University of Leoben

Dissertation

Generation of bulk nanocomposites by severe plastic deformation

Andrea Bachmaier

Leoben, August 2011

This work was financially supported by the Austrian Fonds zur Förderung der wissenschaftlichen Forschung (Project number: S10402-N16).

Copyright © 2011 by Andrea Bachmaier. All rights reserved.

Erich Schmid Institute of Materials Science
Austrian Academy of Sciences
Jahnstrasse 12
A-8700 Leoben

Affidavit

I declare in lieu of oath, that I wrote this thesis and performed the associated research myself, using only literature cited in this volume.

_____

Dipl.Ing. Bachmaier Andrea

Leoben, August 2011

Acknowledgments

I would like to thank my supervisor Reinhard Pippan for assigning this work to me, for his help and guidance, and for giving his expertise to this thesis.

Furthermore, I would like to thank my former as well as my current office colleagues: Peter G., Megan, Martin R., Tristan, Karo and Peter I., for their help and a lot of fun in the office apart from work as well. I would also like to thank my “non-office” colleagues, especially the former and current members of the “SPD” team: Toni, Georg, Doris, “Mr. HPT” Peter, Stephan, Georg H. and Christoph for their generous help performing experiments and discussing results as well as for the discussions “after 4 o'clock”. Furthermore, I would like to thank Christian, Stefan, Thomas, Johannes and Daniel for their great support I received in all matters during my time at this institute.

I would like to express my gratitude to all other employees of the Erich Schmid Institute, in which I was greatly incorporated during this work. I especially wish to thank Edeltraud Haberz and Gabriele Moser for the excellent sample preparations and Franz Hubner and Günther Aschauer for all the work done in the workshop. Furthermore, I would like to thank Viktoria Schrutt and Marianne Fliesser.

I would also like to thank my family and friends for their support and friendship.

I don’t want to achieve immortality through my work,
I want to achieve it through not dying.
(Woody Allen)

Abstract

This work is devoted to the generation of nanocomposites and stable nanocrystallites by severe plastic deformation (SPD) which is quite a new research area in materials science. The main research topics in the last years were the fundamental understanding of the fragmentation process of materials deformed by SPD at very high strains and the limitations of the refinement of single phase materials.

The first chapter of this work is assigned to give a short introduction on the most commonly used SPD methods and in particular to the ones used to perform the experiments during this thesis. Furthermore, a short review about the deformation of single phase materials is given. The main parameters influencing the limitations in the refinement of single phase materials are outlined and a process is proposed which might be the reason for the limit of the refinement.

While a lot of studies have been published about the above mentioned issue in recent years, the structural evolution of multiphase materials during SPD has not been extensively studied and documented. First experiments on metal-metal composites (Cu-Cr, Cu-W) were already performed which result in nanocomposites with a grain size around 10 nm. SPD of the individual materials used in the before mentioned composites leads to a much larger grain size. Therefore, SPD of composites might offer the possibility to obtain materials with a nanocrystalline grain size and offer a possibility to overcome the limitations in the refinement. A short review about all kinds of different composites produced by SPD is also given in the first chapter.

During this thesis, it was possible to develop a new procedure to generate stable nanocrystalline materials by SPD using a similar approach as mentioned above. It is presented in the second chapter of this thesis in more detail. Instead of bulk composite materials, metal powders were consolidated and severely plastically deformed. Due to natural oxide layers on the powder surfaces, nanometer sized oxide dispersions were incorporated in the latter bulk compacts which allows the fabrication of nanocrystalline metal matrix composites. Moreover, not only oxide dispersions were used to stabilize the metallic matrices. By the use of carbon nanoparticles, stable nanocrystalline copper and nickel composites could be obtained as well.

Furthermore, powder mixtures of different combinations of metal powders were severe plastically deformed to form nanocomposites of the individual constituents. Special attention is given to possible dissolution processes and formation of supersaturated solid solutions which were formed during processing although the elements chosen are normally immiscible. After annealing, nanocrystalline nanocomposites with enhanced hardness and thermal stability were obtained.

Kurzfassung

Ziel dieser Arbeit ist es, stabile nanostrukturierte Werkstoffe und Nanoverbundwerkstoffe mit Hilfe der Hochverformung, welche eine relativ neue Methode auf dem Gebiet der Materialwissenschaften ist, herzustellen. Hauptaugenmerk der Forschung in diesem Gebiet lag in den letzten Jahren darin, ein grundlegendes Verständnis für die Kornfeinung, welche in hochverformten Materialien auftritt, zu gewinnen und die Grenzen der Kornfeinung in einphasigen Materialien aufzuzeigen.

Im ersten Kapitel dieser Arbeit wird ein kurzer Einblick in die gängigsten Hochverformungsmethoden gegeben und vor allem jene, welche für Versuche im Rahmen dieser Arbeit verwendet wurden, kurz vorgestellt. Dann wird eine kurze Zusammenfassung über die Hochverformung von einphasigen Materialien gegeben und die wichtigsten Einflussfaktoren auf die dabei auftretende Kornfeinung diskutiert. Weiters wird ein Prozess vorgeschlagen der möglicherweise der Grund für die auftretenden Grenzen in der Kornfeinung in einphasigen Materialien ist.

Während in den letzten Jahren über die Hochverformung von einphasigen Materialien viele Studien publiziert wurden, ist die Mikrostrukturänderung von mehrphasigen Materialien während der Hochverformung noch nicht ausreichend erforscht und dokumentiert. Erste Arbeiten über metallische Verbundwerkstoffe (Cu-Cr, Cu-W) wurden bereits durchgeführt, wobei Nanoverbundwerkstoffe mit einer Korngrösse um 10 nm hergestellt werden konnten. Werden die Materialien, welche in den zuvor genannten Verbundwerstoffen vorkommen, einzeln hochverformt, erhält man eine deutlich größere Korngrösse. Hochverformung von Verbundwerkstoffen stellt somit eine neue Möglichkeit dar, Materialien mit nanokristalliner Korngrösse herzustellen und somit die Grenzen der Kornfeinung weiter nach unten zu schieben. Einen kurzen Rückblick über die bisher mit Hochverformung hergestellten Verbundwerkstoffe findet man im ersten Kapitel dieser Arbeit.

Im Rahmen dieser Arbeit wurde eine neue Methode entwickelt, stabile nanokristalline Materialien herzustellen, indem ein ähnlicher Ansatz wie bei hochverformten Verbundwerstoffen verwendet wurde. Anstelle von massiven Verbundwerkstoffen, werden metallische Pulver konsolidiert und anschliessend hochverformt. Durch die natürliche Oxidschicht auf den Pulverpartikeln können Oxide mit Abmessungen im Nanometerbereich in die später massiven Materialien eingebracht und somit nanokristalline oxid-verstärkte metallische Verbundwerkstoffe hergestellt werden. Aber nicht nur Oxide können verwendet werden um die metallische Matrix zu stabilisieren. Mit Hilfe von Kohlenstoff-Nanopartikeln können nanokristalline, stabile Kupfer und Nickel-Verbundwerkstoffe hergestellt werden.

Weiters wurden Pulvermischungen aus verschiedenen Metallpulvern hochverformt um Nanoverbundwerkstoffe herzustellen. Obwohl die Elemente der gewählten Komponenten der Verbundwerkstoffe normalerweise nicht miteinander mischbar sind, wird die Bildung von übersättigten Mischkristallen beobachtet. Nachfolgende Glühbehandlungen führen zu stabilen, nanokristallinen Verbundwerkstoffen mit verbesserter Härte und hoher thermischer Stabilität.

Motivation and Aim of the Work

Nanocrystalline materials possess unique mechanical, thermophysical, optical and magnetic properties not comparable to their coarse grained counterparts. Therefore, they have been a subject of extensive research in the last decades. Although their improved properties have been known for a long time, application of these nanocrystalline materials is limited due to the challenging task of fabricating bulk nanocrystalline materials which would be necessary for technical applications. With conventional processing routes, just limited dimensions of nanocrystalline materials like thin films or powders are producible. Therefore, one major goal is to develop a method for large-scale processing to obtain massive bulk nanocrystalline materials with dimensions in the millimetre range with 100% density. Severe plastic deformation methods offer a possibility to fabricate such massive bulk nanomaterials.

Severe plastic deformation of single phase materials usually results in ultrafine grained or sometimes even in nanocrystalline materials. The minimum grain size attainable depends on the deformed material itself, and on processing parameters like the deformation temperature, the applied strain and the strain rate. Even if the obtained microstructure is nanocrystalline after deformation, there exists still one major drawback. Unfortunately, the nanocrystalline microstructures of severe plastically deformed materials are often thermally unstable and coarsening of the microstructure can take place even at room temperature. With increasing grain size, the properties of the material are in turn altered.

Aim of this thesis was the generation of stable nanocrystallites in massive bulk form by severe plastic deformation. Hence, a new powder consolidation method by severe plastic deformation was developed to achieve the aforementioned goal and oxide dispersion strengthened metal matrix composites were fabricated. The materials produced exhibited enhanced mechanical properties like high strength and an extraordinary thermal stability.

Another challenge was the fabrication of completely new types of composite materials in bulk form by severe plastic deformation of different metal powder combinations. The composite materials consist of normally immiscible elements and were produced with a novel two step severe plastic deformation process developed during this thesis. These new types of materials might exhibit, apart from improved mechanical properties, extraordinary functional properties. In particular magnetic properties might be extraordinarily enhanced as already shown in mechanically alloyed powders of the same material combinations.

Contents

1. Introduction

1.1. Severe plastic deformation methods

With severe plastic deformation (SPD) methods, submicron- and even nanocrystalline metals and alloys can be easily produced if the fabrication process is compared to other available techniques to manufacture nanocrystalline materials [Zhu04]. The formal definition of SPD is given as follows: *"Any method of metal forming under an extensive hydrostatic pressure that may be used to impose a very high strain on a bulk solid without the introduction of any significant change in the overall dimensions of the sample and having the ability to produce exceptional grain refinement."* [Val06].

A lot of different SPD methods fulfilling these requirements have been developed in the last 20 years which are High-pressure torsion (HPT), Equal Angular Channel Pressing (ECAP), Accumulative Roll Bonding (ARB), repetitive corrugation and straightening or constrained groove pressing to name only a few. The first three mentioned are the most established SPD methods. A schematic sketch of ECAP and ARB process is shown in Fig.1-1. In ECAP, the material is pressed several times through a die which consists of two equal channels. The amount of applied strain per pressing pass depends on the angle Φ between the two channels. During ARB, two sheets are stacked together, rolled to 50% thickness reduction, cut in two pieces, stacked together again and rolled for several cycles repeating the same procedure over and over. A detailed description of these methods can be found in [Bach11].

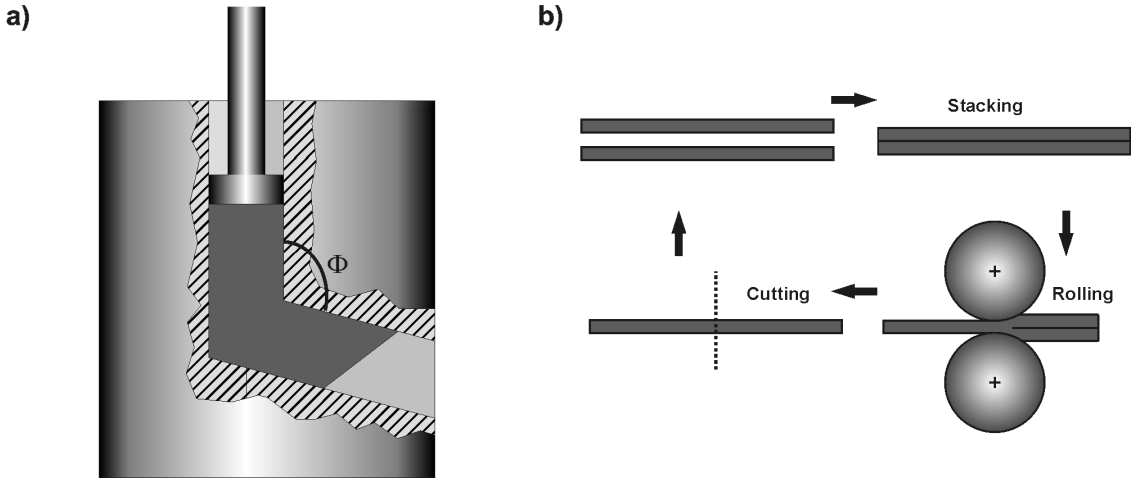

Fig.1-1 Schematic sketch of the a) ECAP and b) the ARB process.

For the experiments conducted within this thesis, predominantly the HPT process was used. The principle of HPT deformation is shown in Fig.1-2. Derived from conventional torsion experiments, a disk shaped specimen is pressed between two anvils by applying a high hydrostatic pressure. While the upper anvil is fixed, the lower one is rotated and the sample is deformed by shear. The equivalent strain ε_v can

be calculated by [Stü03]

$$\varepsilon_v = \frac{2 \cdot \pi \cdot r \cdot n}{t \cdot \sqrt{3}}, \quad (1)$$

where *r* denotes the radius and *t* the thickness of the deformed sample and *n* is the number of applied turns.

Currently, two HPT equipments are installed at the Erich Schmid institute. The first HPT equipment has a maximum load of 400 kN, the maximum load of the second larger equipment is ten times higher (4000 kN). Due to this up scaling in the loading capacity, the possibility to deform large samples with diameters of 30-50 mm and a thickness of about 10 mm, which is currently the largest producible sample size worldwide, is given. Although only smaller samples (diameter of 6-14 mm) can be deformed with the smaller HPT equipment, it offers several unique features. Using an induction coil as heating system and liquid nitrogen for cooling, deformation temperatures between -196°C (liquid nitrogen temperature) and 700°C can be realized. A torque measurement system is also installed which makes it possible to evaluate the flow stress of the material and furthermore to detect possible slippage in-situ during processing. Other processing parameters like the applied strain rate, the applied pressure and the strain path (cyclic or monotonic deformation) can be easily adjusted over a wide range.

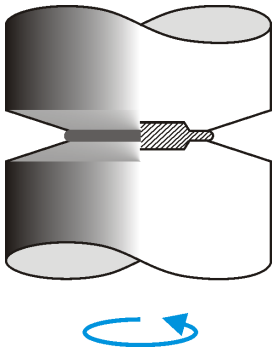

Fig.1-2 Schematic sketch of the principle of HPT deformation.

For a systematic study of the influences of the deformation temperature, alloying and the strain rate on the saturation region during HPT deformation of single phase materials (bulk Al and bulk Al-Mg alloys) in publication A, the small HPT equipment was used due to the aforementioned reasons. The consolidation and deformation of the different metal powders to form metal-matrix composites with oxide or carbon based reinforcements were performed with this equipment as well (publications C and D).

For manufacturing the metal-metal composites, a two step HPT process, only possible due to the availability of both HPT equipments, was developed during this thesis. Consolidation of the different powder mixtures to samples with 30-50 mm diameter was directly conducted in the large HPT equipment and the samples were subsequently deformed. From these large samples, smaller samples (8 mm diameter) were cut and deformed a second time with the smaller HPT equipment. A schematic

sketch of the individual steps of the sample production, which also includes a rotation of the deformation direction, can be seen in Fig.F1 in publication F.

Moreover, conventional cold rolling with a standard rolling mill was performed on previously HPT deformed bulk Ni samples to investigate if a different strain paths result in a different saturation grain size (publication B). The von Mises equivalent strain for rolling deformation, ε_{CR}, was calculated by

$$\varepsilon_{CR} = \frac{2}{\sqrt{3}} \ln\left(\frac{t_o}{t_f}\right), \quad (2)$$

where t_o and t_f denote the thickness of the sample before and after the cold rolling, respectively.

The same rolling mill equipment was used to roll stacks of Al foil with different initial foil thickness to study the role of oxides hindering grain boundary motion and on the developing microstructure. This rolling process resembles the repeated rolling and folding process which is in turn similar to the ARB process [Din05]. Differences are the amount of strain which is applied and that the initial material consists of a multilayer instead of two sheets.

1.2. Deformation of single phase materials

During SPD, the dislocation density is significantly increased and cell blocks with large misorientations as well as dislocation cells are formed in the initial coarse grained material. The size of both cell types is decreased with increasing deformation and transformed to an uniform grain structure at high strains. Depending on the material and the applied strain, ultrafine grained or even nanocrystalline microstructures are obtained [Pip06, Val00, Zeh04]. After applying a certain amount of strain, which is dependant on the deformed material, a limit in the refinement in single phase materials is observed. Not only is the starting point of this saturation region in the grain refinement determined by the material, also the minimum achievable grain size is material specific [Pip06, Pip10].

Although the occurrence of the saturation during SPD is well known, there still exist open-ended questions like what are the reasons which limit the refinement during SPD and how a steady state in the microstructure can be retained although continuously more and more strain is applied. To maintain a steady state, a balance in the dislocation density, grain boundary length and vacancy density must exist. Another question which arises is how it might be possible to overcome the limit in refinement.

One possible answer for the first question is that there might be a change from a distributed shear deformation to a very localized deformation like in grain boundary sliding. During such deformation, the rest of the microstructural elements would remain undeformed. Hafok et al. [Haf07] showed that the microstructure of a Ni sample deformed by HPT is deformed homogeneously in the saturation region and no grain boundary sliding was observed experimentally.

In publication A, enclosed in the appendix, the influence of the deformation temperature, the strain rate and the addition of alloying elements on the saturation microstructure of single phase Al and Al-Mg alloys is investigated in detail.

Three major parameters control the final grain size in the saturation region in single phase materials and the amount of strain which must be applied to reach the saturation region. First of all, there is the

large influence of the deformation temperature: the lower the deformation temperature, the smaller the final grain size and the higher the necessary strain to reach saturation. The influence of the deformation temperature on the size of the structural elements and the measured microhardness after deformation is illustrated in Fig.A4 in publication A. With increasing deformation temperature, the size of the grains increases and the hardness decreases. Furthermore, the onset point of saturation is shifted to higher strains with decreasing deformation temperature (shown in Fig.A1 in publication A). Furthermore, the texture obtained after HPT deformation as well as the morphology of the grains is changed with the deformation temperature.

The second important parameter is the strain rate which only has an influence at certain deformation temperatures. For example, the strain rate influences the final grain size of Al-Mg alloys at deformation temperatures higher than room temperature. In the strain rate sensitive regime, smaller final grain sizes are obtained if a higher strain rate is applied. The strain rate sensitive regime and the final grain size of the Al-Mg alloy with 3 wt% Mg deformed at two different strain rates is shown in Fig.A5 in publication A.

The last parameter influencing the saturation microstructure is the amount of added alloying elements. In Fig.1-3, the final microstructure in the saturation regime of a bulk Al sample and a bulk Al-Mg sample with 1 wt% Mg deformed by HPT is shown. Comparing both microstructures, a significantly smaller grain size is obtained in the Al-Mg alloy. The grain size in the HPT deformed bulk Al samples is ~ 1 µm and the grain size in HPT deformed alloy is ~ 300 nm. Not only deliberate alloying elements, but also impurities influence the saturation region during SPD deformation. Just by the alteration of the carbon content in Ni, which is deformed by HPT at room temperature, final grain sizes of 130nm–380nm in the saturation region can be attained [Rat11].

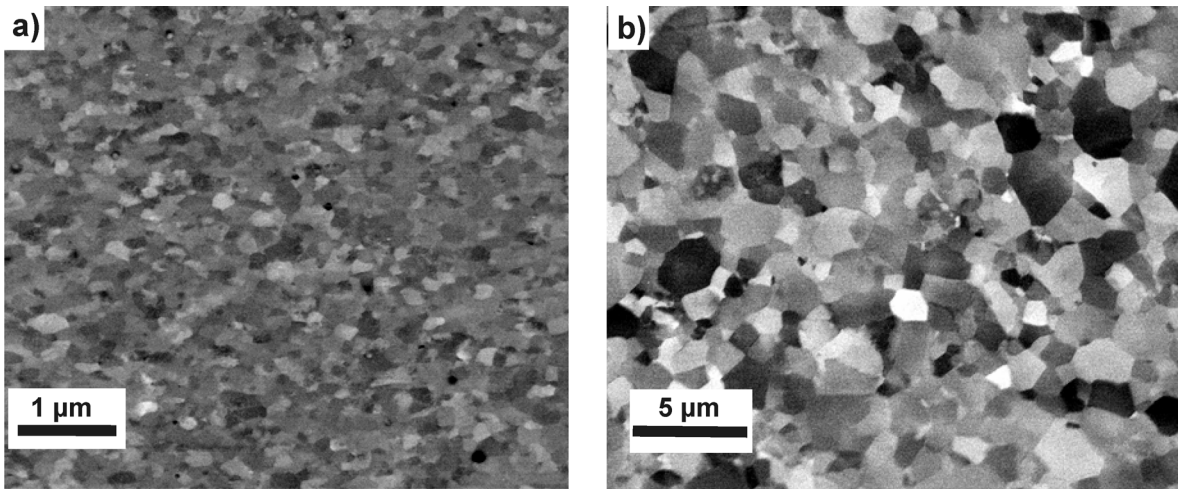

Fig.1-3 Back scattered electron image of the saturation microstructure of a) an Al-Mg sample with 1 wt% Mg addition and b) a bulk Al sample.

Based on the results in publication A, dynamic recrystallization is proposed as structural restoration process at medium SPD temperatures similar to the steady state deformation in hot forming at high homologous deformation temperatures. At low homologous deformation temperatures, a similar

process is suggested. In that case stress induced grain boundary migration is the alternative proposed restoration mechanism.

In summary, grain boundary migration is the main grain size controlling mechanism in the saturation regime during SPD. Therefore, a restriction of boundary migration should result in a smaller saturation grain size which can be achieved by a higher amount of alloying elements or impurities or a reduction of the deformation temperature. Another possibility to stabilize the microstructure during deformation is the introduction of phase boundaries like in composites or introducing stable second phase particles which will be discussed in chapter 1.3 and chapter 3 of this thesis.

In publication B, possible effects of different SPD methods and therefore different strain paths on the final microstructure in the saturation region were evaluated. A different strain path might result in different saturation grain sizes. Therefore, Ni samples were HPT deformed until the saturation region was reached. Afterwards, the previously deformed HPT samples were cold rolled to two different amounts of strains. The grain size could not be significantly refined nor could the hardness be considerably increased after the additional cold rolling as can be seen in Fig.B1 and Fig.B2 in publication B. Only the shape of the grains is somewhat elongated after the additional rolling but the elongation was much less than expected from simple geometrical considerations. Moreover, the thickness reduction of the grains does not correlate with the applied reduction of the rolled sheets. Based on the results obtained it can be concluded that the restoration processes proposed beforehand are the same during HPT deformation and during cold rolling in the saturation regime.

1.3. Deformation of two phase materials

In the following chapter, the fabrication of different composites by SPD methods like metal-metal composites, metal matrix composites and amorphous metal matrix composites with ultrafine grained as well as nanocrystalline microstructures is briefly outlined. More details can be found in [Bac11].

Composites usually have a ceramic, metallic or polymeric matrix and an additional second phase, usually denoted reinforcement phase, is added to improve the properties of the composite material. It is important for the performance of the composite that the matrix has a uniform microstructure, ideally nanocrystalline, and that the reinforcement phase is homogenously distributed through the matrix material. Conventional composite processing routes like powder extrusion or sinter forging are often confronted with problems achieving the aforementioned goals [Vis06].

Depending on the kind of second phase particle and its individual deformation behaviour, the deformation behaviour of composite materials is different compared to single phase materials. On account of this the selection of a suitable SPD process as well as the size and volume fraction of the reinforcement phase is very important [Bac11].

During SPD of metal-metal composites, either nanostructured composite materials are obtained or the formation of supersaturated solid solutions or amorphization occurs. SPD of metal matrix composites results in grain refinement of the matrix material and the reinforcing constituent. Furthermore, a

uniform distribution of the second phase in the matrix is usually achieved. Therefore, the properties of the composites are improved [Bac11].

Metal-Metal composites

Composites consisting of two distinct metals can be easily produced by SPD. In the ideal case, the microstructures of both metal phases are refined during SPD and a composite with a nanocrystalline microstructure can be obtained.

One example is the fabrication of multilayer composites consisting of different metal combinations with the ARB process or with the repeated rolling and folding process. Different metals can be combined to form micrometer or even nanometer sized composites after deformation. Dependent on the number of rolling cycles, the thickness of the individual layers of the composite can be adjusted. Several examples for Al-Ni, Al-Mg, Al-Cu, Cu-Nb, Ti-Al, Cu-Zr composites are given in [Che06, Eiz08, Lee06, Luo04, Luo06, Sha10, and Sun10a]. Due to the different flow properties of the joint metals, a composite microstructure consisting of fragments of the metal with the higher strength embedded in the “softer” metal matrix material is obtained. The produced composites normally exhibit enhanced strength combined with reasonable ductility. Micrometer or nanometer sized composites can also be easily produced by HPT and ECAP which is reported for Cu-Ag and W-Cu composites, for example [Sab05, Tia10].

If a nanocomposite has already been formed but further strain is applied, the nanometer sized phases of the distinct constituents become thinner and thinner during ongoing deformation. If a critical thickness, which is dependent on the individual stability of the different phases and phase mixtures, is reached, unique features can be observed in the composites. One possibility is the formation of supersaturated solid solutions, the other is the occurrence of amorphization reactions. An Enhancement of the solid solubility for many normally immiscible systems like Fe-Cu, Cu-Cr or Cu-Co has been observed [Nis08, Sau05a, Sau05b, Sau08a, and Tep05].

Furthermore, SPD can extend the solubility of Fe in Al [Sen98, Sto03, and Tch04]. Complete or partial amorphization reactions have been observed in Cu-Ag, Cu-Zr, Cu-Ti-Zr, Cu-Ti-Zr-Ni composites after the repeated rolling and folding process [Rös07a, Rös07b, Ohs07, and Sun07]. One advantage is that during subsequent annealing treatments, decomposition of the supersaturated solid solutions is observed in most of the alloy systems and stable nanocomposites with enhanced hardness and high thermal stability are formed. Different explanations for the occurrence of this “bulk” mechanical alloying can be found in literature which are mainly diffusion driven mechanisms, defect-enhanced diffusion mechanisms and a mechanical intermixing mechanism which is driven by the plastic deformation [Raa10]. Amorphization occurs either directly, without prior formation of supersaturated solid solutions, or with a prior non-equilibrium intermixing of different phases and is proposed to occur due to the reduction of the high dislocation density by the amorphization reaction [Raa10].

These “new” alloys, formed from usually immiscible elements, exhibit extraordinary magnetic properties like high magnetoresistance or coercivity. Furthermore, high thermal and electrical conductivity is reported which makes these materials of particular interest [Ma05, DiM07].

Over the course of this thesis, the immiscible Fe-Cu and Ag-Ni systems have been investigated and deformed by a novel two step HPT process. Both systems exhibit a positive heat of mixing [Ma05]. The phase diagrams of the systems can be seen in Fig.1-4.

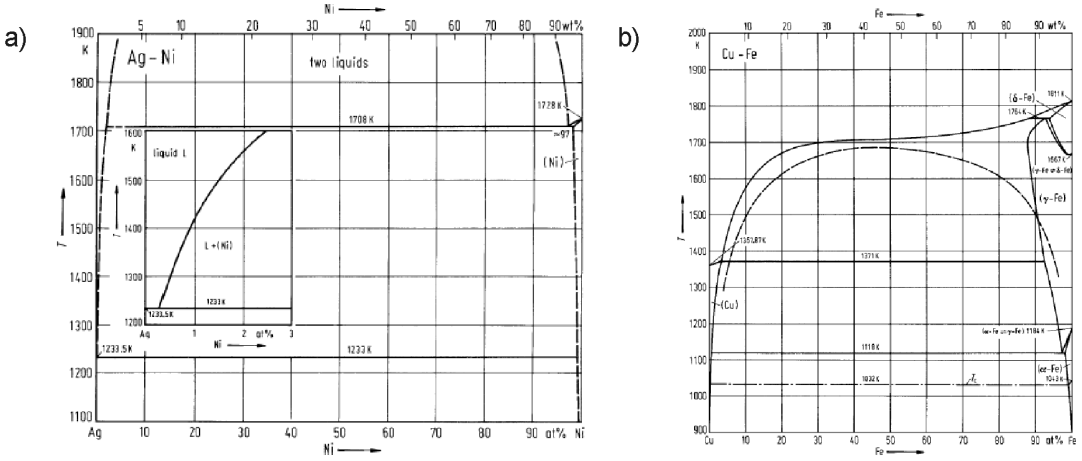

Fig.1-4 Phase diagram of Ag-Ni and Cu-Fe [Pre98].

The Ag-Ni system has a large positive heat of mixing which means that the system is immiscible even in the liquid state up to high temperatures. The Fe-Cu system exhibits a smaller heat of mixing. Therefore, the system is only immiscible in the solid state. Through several different processing routes like rapid quenching or mechanical alloying, the formation of single phase alloys consisting either of amorphous phases or crystalline supersaturated solid solutions or other metastable compounds have been observed before in these alloy systems [Ma05]. Ag-Ni alloys are reported to be diffraction amorphous for compositions with~ 20-70 at% Ag content and Ag face-centred cubic solid solutions are obtained for higher Ag contents as well as Ni face-centred cubic solid solutions for lower Ag contents [Hau75, He01, Ma01, Xu96]. In the Fe-Cu system, face-centred cubic or body-centred cubic single phase or two phase supersaturated solid solutions, depending on the amount of Fe and Cu content, are obtained but usually no amorphization reactions are observed [Eck96, Ish92, Ma93].
Further details, results and discussion about the investigated Fe-Cu and Ag-Ni systems are given in chapter 3.2 and publication E and F.

Metal-Matrix composites

Particle reinforced metal-matrix composites are reported to possess superior mechanical and thermal properties compared to their corresponding matrices because ideally the composite material combines the properties of the matrices with those of the reinforcement. It is a large family of materials which can be differentiated either according to the type of reinforcing phase which is embedded in the metallic matrix material or according to the geometric shape of the reinforcement. Using the first distinctive feature, metal-matrix composites reinforced with ceramic, carbon based and other second phase particles which are processed by the different SPD techniques can be distinguished and will be shortly presented in this chapter. Detailed descriptions can be found in [Bac11].

The properties of metal-matrix composites are mainly controlled by the size of the reinforcing phase in relation to the size of the matrix microstructure as well as by the distribution of the second phase in the metallic matrices. Diminished ductility and toughness are reported in conventionally processed metal-matrix composites [Vis06].

The majority of metal matrix composites deformed by SPD are those reinforced with ceramic particles which can be further divided corresponding to the type of ceramic used (mainly Al_2O_3, SiO_2, SiC particles). Furthermore, some work has been conducted on metal-matrix composites reinforced with miscellaneous metallic particles. In the case of coarse grained composite starting materials, SPD results in grain refinement of the matrix material independent of the used SPD technique. The major difference between the various SPD techniques is the amount of strain which can be applied. The distribution of the second phase particles in the matrix of the composite generally becomes more uniform, the higher the amount of applied strain [Bac11].

During ECAP processing, the application of high strains is often inhibited due to crack formation in the samples. Although the use of back pressure reduces the crack formation probability, particle free zones as well as particle clusters often remained after ECAP deformation. Furthermore, the particle size of the second phase is often unchanged after ECAP processing and remains micrometer sized [Mun05, Mun06, Val98]. ARB processed composites experience with the same drawbacks. The matrix grain size is refined during processing, whereas the size of the particles remains unchanged due to their undeformability [Jam10]. HPT processed composites, however, exhibit better homogeneity of the second phase particles after processing due to the larger applied strains and the size of the particles is more effectively reduced. In most cases, nanocrystalline composites reinforced with homogeneous nanometer sized particles and therefore exhibiting excellent thermal stability, high strength and high ductility are fabricated by HPT [Isl01].

As mentioned before, the size as well as the distribution of the second phase particles has a huge influence on the properties of the composite. To obtain a high thermal stability, for example, a homogeneous dispersion of fine and stable second phase particles is necessary. The same holds if mechanical properties are regarded [Bac11].

Another SPD composite production alternative is the use of powder mixtures of the different composites' constituents and subsequent consolidation and deformation by SPD. To improve the distribution of the second phase particles and to refine the grain size before deformation, prior ball milling treatments of the powder mixtures are often performed. The SPD deformation usually leads to bulk dense samples with a matrix grain size in the nanometer range [Ale98a, Ale98b, and Sor08].

Another option is the use of pure metallic powders. During SPD deformation natural oxides from the powder surfaces are introduced in the latter bulk compacts leading to oxide dispersion strengthened composites with a nanocrystalline matrix grain size. A schematic sketch of the process is shown in Fig.1-5. During the deformation, the powder particles are deformed and elongated. Due to the deformation, the oxide layer fracture into small oxide particles which are subsequently incorporated in the metallic matrix. In this thesis, aluminium and nickel based metal-matrix composites reinforced with oxide particles are produced by this technique. Further details can be found in the chapters 3.1.1 and publication B-D.

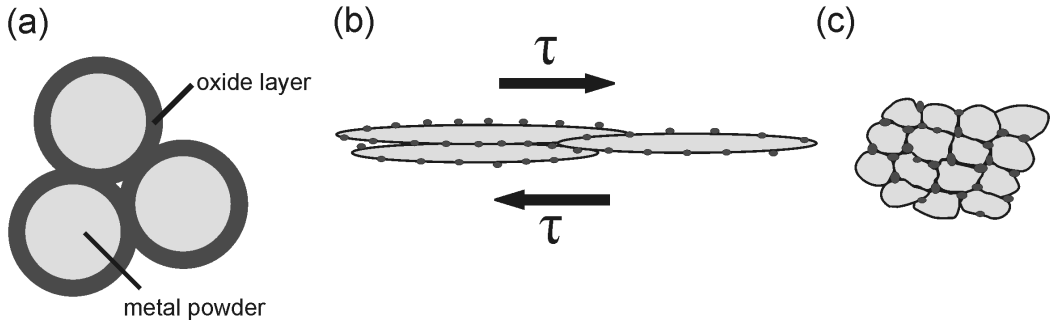

Fig.1-5 Schematic sketch of the HPT metal powder consolidation and deformation process illustrating the change from the coarse powder to the consolidated elongated grains and the resulting final stabilized ultrafine grained or nanocrystalline material. Figure taken and adapted from publication C.

Metal matrix composites with novel second phase materials can also be easily produced by the SPD powder consolidation and deformation techniques. Nanocrystalline carbon based particles (carbon nanotubes, fullerene or carbon black particles) mixed with metallic powders are such an option. Such composite types have been produced by HPT as well as with ECAP. Composites processed by other non SPD techniques have to deal with problems like cluster formation of the carbon particles during processing or carbide formation because subsequent sintering steps are required to achieve dense samples [Oga07, Xu99, and Zho03].

In the majority of reports, nanocrystalline bulk composites with homogeneously dispersed carbon based particles have been obtained and an enhancement of thermal stability and strength accompanied with a deterioration of ductility was observed. Mainly Cu and Al powders were used as matrix materials which were mixed with the corresponding carbon reinforcement material and were subsequently consolidated and deformed [Gou09, Li09a, Li09b, Tok08a, Tok08b, and Sar07]. Initial ball milling of the powder mixtures was often conducted to increase the homogeneity of the composite [Li09a, Li09b]. The damage of the carbon nanotubes after SPD was reported in [Tok08a], while in other studies no destruction of the carbon based particles was observed [Li09a, Li09b].

Within the framework of this thesis, Ni and Cu based metal matrix composites reinforced with fullerenes were examined. The composites were produced by HPT deformation starting with micrometer sized powders without ball milling before compaction. The influence of the fullerenes on microstructure and mechanical properties has been investigated. By means of high-resolution transmission electron microscopy the possible destruction of the fullerenes has been examined and results are reported in chapter 3.1.2.

Amorphous metal matrix composites and miscellaneous

A new approach in this research field is the production of amorphous metal matrix composites with different types of reinforcement like ceramics, refractory metal phases or carbon fibres [Bac11]. Using SPD methods, a wider range of options is available for the choice of reinforcement and range of composition compared to standard production methods as shown in first studies in [Bot04, Mat07, Sun10b and Yav02].

Another possibility is the combination of a metallic glass matrix with a polymer as a second phase or the combination of a metallic matrix material with a polymer [Kün07, Sau08].

2. Improvements in processing by HPT

In several studies it is shown that different composites or nanocomposites can be processed by the use of different SPD methods. The best results are obtained with the HPT process which is related to the high amount of strain which can be applied with this process due to the high pressure.

Shear deformation is the deformation mechanism in HPT and ECAP. If a composite material is deformed by HPT in the ideal case, the individual components of the composite are continuously sheared and their thickness decreases with increasing applied strain (Fig.2-1a). The final size d_1 of the individual composite components can be calculated, if a large amount of γ is applied, by

$$d_1 = d_0 / \gamma \,, \tag{3}$$

where d_o denotes the initial component size and γ is the shear strain.

For example, the microstructure of a $Fe_{85}Cu_{15}$ composite material deformed by HPT for 10 rotations can be seen in Fig.2-1b. Inside the individual components of the composite an ultrafine grained microstructure develops but the size of the Fe and Cu components is in the micrometer range. On that account very high amounts of strain are necessary to reach a nanostructure in the composite using monotonic shear deformation.

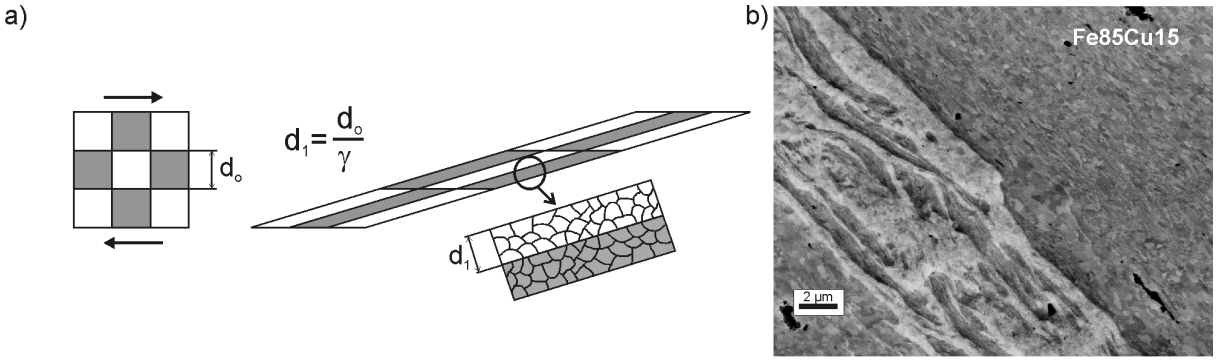

Fig.2-1a) Schematic sketch of the deformation behaviour of the individual composite components during monotonic shear deformation. b) Scanning electron image of the microstructure of a $Fe_{85}Cu_{15}$ composite material deformed by HPT for 10 revolutions recorded with back scattered electrons detector at a radius of 10 mm in tangential direction.

Applying such high amounts is in principle possible by the HPT process, but it requires a large amount of time and energy. Therefore, a novel two step process was developed during this study.

From the deformed samples, new samples are cut and deformed. Furthermore, the shear direction is rotated by 90° for the second step of the HPT deformation. After both steps, the thickness of the individual components of the composite can be reduced by

$$d_2 = d_0 / \gamma_1 \gamma_2 \,, \tag{4}$$

where d_2 is the thickness of the individual composite components after both deformation steps and γ_1 and γ_2 are the applied shear strains in HPT step 1 and 2, respectively. The effectiveness of the process is shown in Fig.2-2. It shows the microstructure of the $Fe_{85}Cu_{15}$ composite sample after both deformation steps. Compared to Fig.2-1b, the grain size of the composite material is significantly reduced and a final nanocrystalline structure is reached. Further details of the process can be found in publication F.

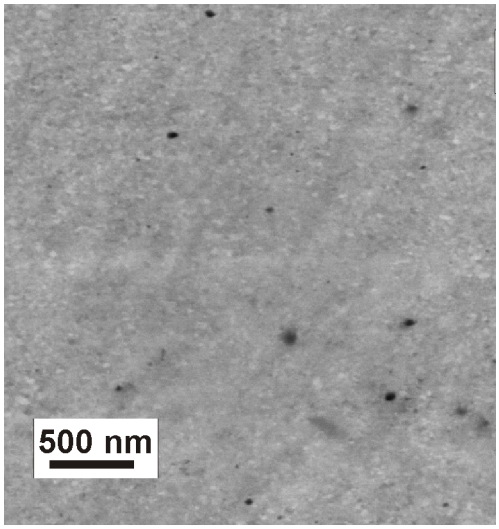

Fig.2-2 Scanning electron image of the $Fe_{85}Cu_{15}$ composite sample recorded with back scattered electrons at a radius of 3 mm in tangential direction after both HPT deformation steps.

The advantages of the newly developed process are not only the quick way to produce nanocomposites. There is also an uncomplicated choice of combinable materials and the composition of the composite can be easily controlled. Micrometer sized powders used in these processes are easier to handle and to produce. Furthermore, the high quality final product is already in bulk form and there might be also potential to scale up the process in future.

The same advantages are valid for the second composite production process which is HPT consolidation and deformation of metallic powders. This process uses the natural oxide layer on the powder particles to fabricate oxide dispersion strengthened composites. Not just oxides can be incorporated in the latter bulk compacts. By the use of coating processes or initial carburization of the metallic powders, completely new types of metal matrix composites of type MC_x or MX_x (C denotes carbon and X stands for the second arbitrary component) can be produced.

3. Results and Discussion

In this chapter, the results of the thesis are summarized. This part outlines the major findings of the present thesis which have already been published (Publications A-F). Furthermore, unpublished results of experiments conducted during the thesis are also presented.

3.1. Metal matrix composites

3.1.1. Nickel and aluminium based composites

With the novel powder processing route introduced in chapter 1, bulk nanocrystalline Al- and Ni-matrix composites with nanometer sized oxide dispersions are obtained. The second phase particles are easily introduced in the material during HPT consolidation and deformation, finally they are homogeneously distributed through the matrix material. The matrix is strengthened by the nanostructured oxides which results in high hardness and exceptional grain size stability upon annealing. Further details and results can be found in publication B-D.

For the production of the Al based composites, different SPD methods (cold rolling of multilayers of Al foils with different initial thickness and HPT consolidation and deformation of Al powders with different initial particle size) were used. Regardless of the applied SPD method and independent of the initial starting material, a reduction in size of the grains by a factor over ten can be achieved due to the pinning effect of the particles hindering grain boundary migration during deformation. More details can be found in publication D.

The processed Al composites might be material candidates for different structural applications, for example in the automotive and sports goods industries due to their superior mechanical properties like increased yield strength and ultimate tensile strength (Fig.3-1).

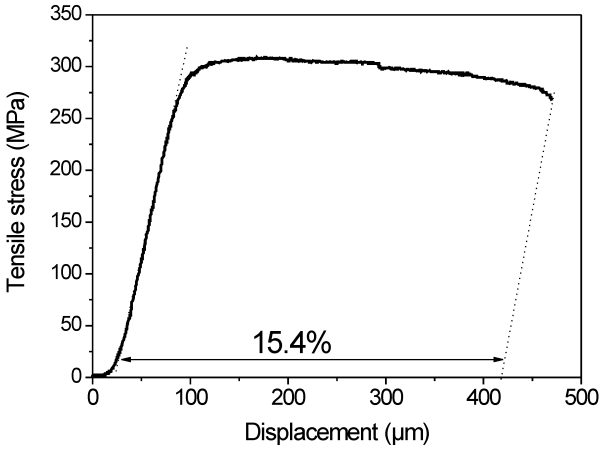

Fig.3-1 Tensile stress – displacement curve of an Al based composites sample with an ultimate tensile strength of ~300 MPa and a total elongation to fracture of 15.4%.

Even the ductility of the Al based composites is reasonable. Low ductility and a brittle fracture behavior might prevent use of the Ni based composites for structural applications. This material group might be a potential candidate for functional applications with the focus on soft magnetic properties. SPD can be used to synthesize nanocrystalline massive Ni samples with a grain size of about 20 nm in one single step which could perfectly fill the gap between amorphous metals and conventional polycrystalline metals.

3.1.2. Nickel-fullerene and copper-fullerene composites

With the powder processing route, Ni-fullerene and Cu-fullerene composites are also produced. The materials used were Cu powders (99.9% purity, -170+400 mesh) and Ni powders (99.8% purity, -150+200 mesh) mixed with different amounts of fullerenes in powder form (C_{60}, 99.5 % purity). The Ni powders were mixed with 1 wt% C_{60} and the Cu powders with 1, 2.5 and 10 wt% C_{60}, respectively. Afterwards, the powder mixtures were directly HPT consolidated and deformed at room temperature with a pressure of 4 GPa for 25 to 50 rotations to final samples of 8 mm diameter and a thickness of ~0.5 mm.

In Fig.3-2, the saturation microhardness of the Ni and Cu based composite samples as a function of the C_{60} content as well as of pure HPT consolidated Cu and Ni powder samples for comparison is plotted. An increase in hardness from about 5 GPa for the Ni powder sample without C_{60} to 5.6 GPa with 1 wt% C_{60} is observed. It should be noted that HPT deformation of bulk Ni results in a saturation hardness of ~2.8 GPa [Bac09]. In case of the Cu composite samples, an increase in hardness with increasing amount of C_{60} is visible. The pure HPT deformed Cu sample exhibits a hardness of 2.1 GPa, the addition of 10 wt% C_{60} results in hardness of 3.1 GPa.

Comparing back scattered electron images of the microstructure of the different composite samples with and without C_{60}, smaller Cu and Ni grain sizes are obtained due to the addition of C_{60} in the composites. In both cases, nanocrystalline microstructures are obtained.

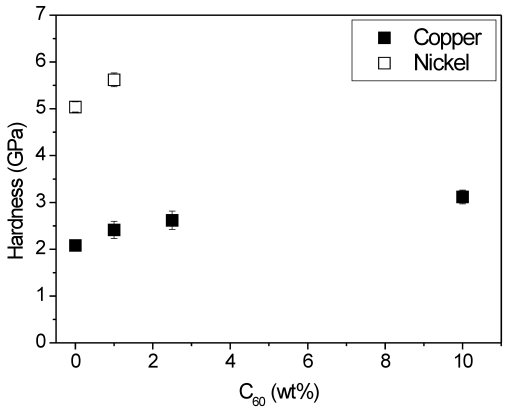

Fig.3-2 Microhardness as a function of the C_{60} content in weight percent (wt%) for the Ni and Cu based composite samples and for pure Cu and Ni HPT consolidated and deformed powder samples, respectively.

Transmission electron microscopy was used to study the microstructure of the Cu composites in more detail. In Fig.3-3, a bright field transmission electron micrograph image of the Cu composite sample with 2.5 wt% C_{60} is shown. The image reveals a nanocrystalline structure with most of the grains below 50 nm. A similar microstructure is obtained in the Cu composite sample with 1 wt% C_{60} and 10 wt% C_{60}.

During the fabrication of metal matrix composites reinforced with carbon nanotubes by SPD processes, the destruction of the carbon nanotubes was reported in [Jen11, Tok08a]. In Al-fullerene composites, no damage of the fullerenes was observed with Raman spectroscopy measurements [Tok08b]. To examine if the fullerenes in the Cu composite samples withstand SPD without destruction, the morphology of C_{60} in the Cu composite sample with 10 wt% C_{60} after HPT was studied by high resolution transmission electron microscopy and electron energy loss spectroscopy.

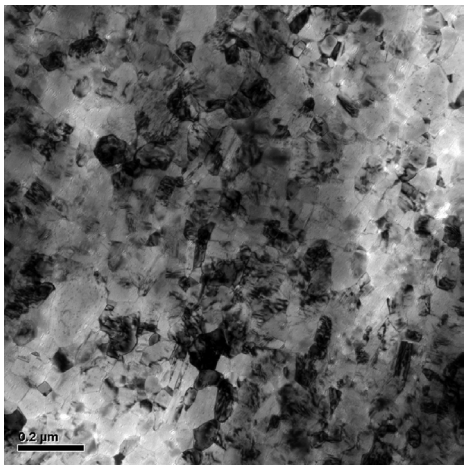

Fig.3-3 Bright field transmission electron micrograph image of the Cu composite sample with 2.5 wt% C_{60}.

In Fig.3-4, the high angle angular dark field electron microscope image of the Cu composite sample with 10 wt% C_{60} can be seen. Apart from nanocrystalline Cu grains, large black areas can be seen. We assume that these black areas are C_{60} agglomerates which are formed in the specific composite due to the large fraction of C_{60}. In the Cu and Ni composite samples with lower amounts of C_{60}, homogeneous nanostructures without such agglomerates are observed which excludes the possibility of using electron energy loss spectroscopy to identify the morphology of C_{60} and to answer whether the C_{60} particles are destroyed during SPD. The electron energy loss spectrum recorded at one of the dark spots indicated by “EELS” in Fig.3-4a, can be seen in Fig.3-4b. The spectrum of the dark regions is similar to the electron energy loss spectrum recorded of amorphous carbon. Therefore, it gives evidence that the C_{60} particles are destroyed by SPD. Nevertheless, more investigations definitely must be performed to answer this question.

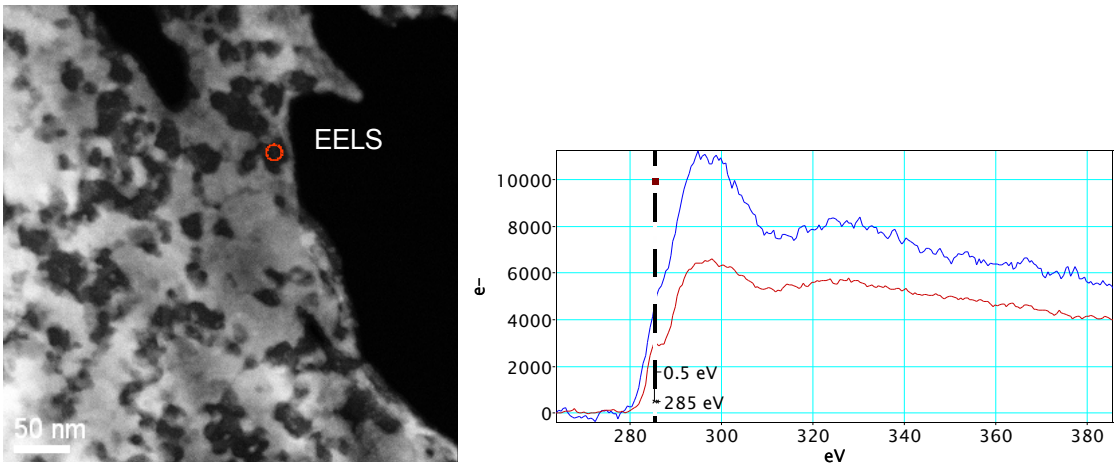

Fig.3-4 a) High angle angular dark field scanning transmission electron microscope image of the Cu composite sample with 10 wt% C_{60} and b) electron energy loss spectrum of the dark regions of the Cu composite sample with 10 wt% C_{60} (blue curve) and electron energy loss spectrum of amorphous carbon (red curve).

3.2. Metal-Metal composites

3.2.1. Iron-copper composites

By mixing Fe and Cu powders and subsequent HPT consolidation and deformation using the novel two step process introduced in chapter 2, fully dense bulk Fe-Cu nanocomposites are processed. Supersaturated single phase solid solutions of Cu in Fe and Fe in Cu are obtained for high Cu or Fe contents. For intermediate Cu or Fe contents, two phase supersaturated solid solutions are obtained. Decomposition of the alloys occurs during annealing which results in the formation of nanostructured Fe-Cu composites. The formed nanocomposites exhibit high hardness as well as stable nanostructures up to high annealing temperatures. Further details can be found in publication F.

The novel two step process allows synthesizing a new type of material which possesses unique properties, in particular magnetic properties. Mechanically alloyed nanocrystalline Fe-Cu powders show large magnetostrictive effects and face centred cubic Fe-Cu supersaturated solid solutions are ferromagnetic for low Fe contents [Gor06]. The advantages of the SPD process compared to mechanical alloying are the macroscopic dimensions of the material which can easily be obtained as well as the low influence of impurities. Whether SPD materials exhibit the same magnetic properties as mechanically alloyed powders must be still investigated.

3.2.2. Nickel-silver composites

Ag powder (99.99% purity, -300 mesh) and Ni powder (99.8% purity, 150+200 mesh) were mixed in two different ratios to obtain powder mixtures with a fraction of 10 and 30wt% Ag. Subsequent

consolidation and deformation were performed with the two-step HPT process described in detail in chapter 2 and publication E and F. In Table 3-1, further details o the deformation parameters are listed.

	1. Deformation Step			2. Deformation Step		
	# rotations	thickness (mm)	Ø (mm)	# rotations	thickness (mm)	Ø (mm)
$Ag_{10}Ni_{90}$	10	9,4	50	50	0,5	8
$Ag_{30}Ni_{70}$	10	9,5	50	100	0,6	8

Table 3-1 Deformation parameters of the first and second deformation step for all deformed AgNi samples.

As described in chapter 1, the formation of single phase alloys consisting either of amorphous phases or crystalline supersaturated solid solutions in these alloy systems has been observed before.
In Fig. 3-5, the microstructures of the $Ag_{10}Ni_{90}$ sample and the $Ag_{30}Ni_{70}$ sample after the first processing step recorded at a radius of 10 mm in the tangential direction are shown. Due to the higher scattering factor of the Ag phase, Ag-rich phases appear brighter in the images recorded with the back scattered electron detector. Both samples show a microstructure consisting of two distinct phases, where the Ag and Ni phases can be easily distinguished. Bands of Ag-rich regions are embedded in the Ni phase. The grain size of the Ni phase is around 300 nm and the grain size of the Ag phase seems to be somewhat smaller. The widths of the Ag bands as well as the distance between the Ag bands differ significantly.

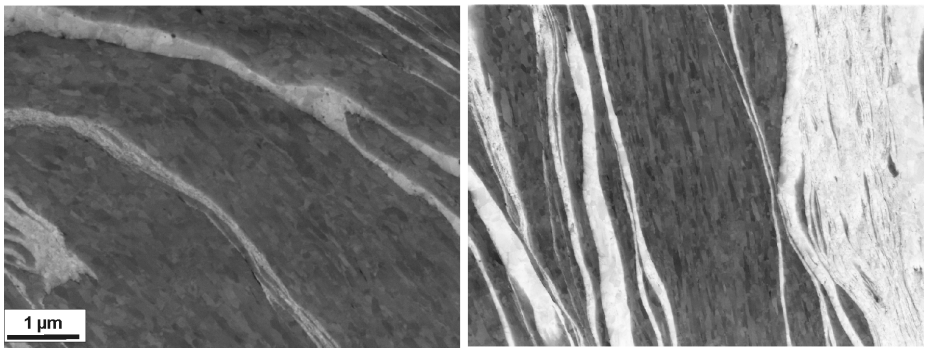

Fig.3-5 Back scattered electron image of the $Ag_{10}Ni_{90}$ sample after the first processing step on the left side and of the $Ag_{30}Ni_{70}$ sample on the right side recorded at a radius of ~10 mm ($\gamma_1 \sim 70$). The magnification is the same in both images.

In Fig.3-6, the microstructure of the samples after the second processing step in the center of the sample (~ radius 0 mm) and at the outer edge of the sample (~ radius 3 mm) is shown. At a radius of about 0 mm which corresponds to a low degree of deformation a two phase composite structure can still be seen in both samples (Fig.3-6a and c). Nevertheless, the grain size as well as the width of the Ag bands and the distance between the Ag bands is significantly reduced and nanometer sized in both composites. In the $Ag_{10}Ni_{90}$ sample, some larger Ni grains can be seen as well. At a radius of 3 mm

which corresponds to a high degree of deformation (γ_2~1880 and 3140, respectively) a homogeneous microstructure is obtained in both samples (Fig.3-6b and d). The grain size in both composites is below 50 nm. From the back scattered electron images no distinction between Ag and Ni phase can be made due to the small grain size and lack of contrast.

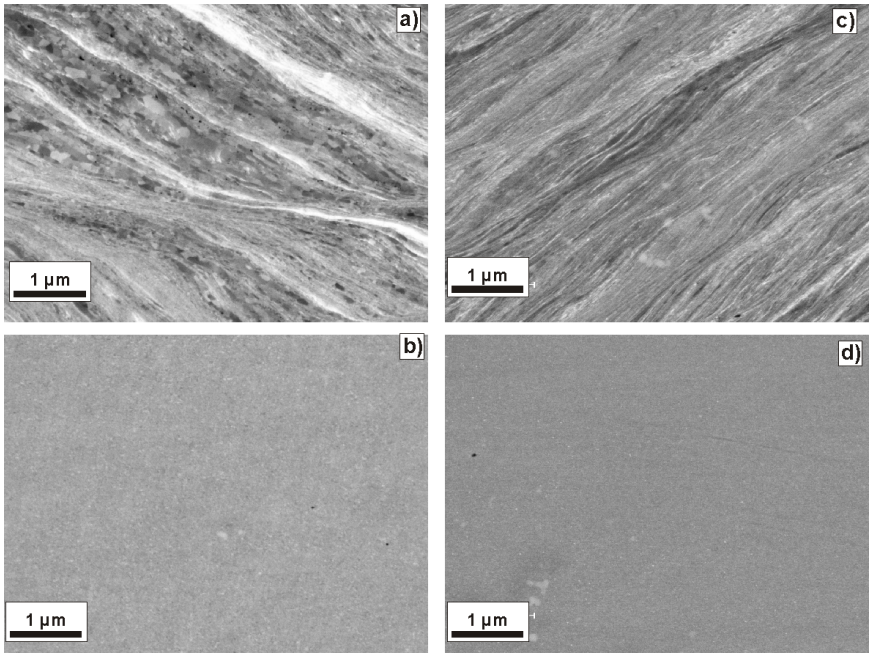

Fig.3-6 Back scattered electron images of the $Ag_{10}Ni_{90}$ sample recorded a) at the center of the disk and b) at the outer edge of the disk, and back scattered electron images of the $Ag_{30}Ni_{70}$ sample recorded c) at the center of the disk and d) at the outer edge of the disk.

In Fig.3-7, the microhardness of the $Ag_{10}Ni_{90}$ sample (red symbols) and $Ag_{30}Ni_{70}$ sample (black symbols) after the first and second processing step are shown, respectively. After the first processing step, a constant microhardness across the radii of the disks of approximately 250 HV is measured in both samples independent on their composition. After the second processing step, the hardness of the $Ag_{30}Ni_{70}$ sample increases from about 450 HV in the center of the sample to about 600 HV at the outer edge of the sample. The $Ag_{10}Ni_{90}$ sample has approximately the same hardness in the center of the sample but a higher hardness (~700 HV) is reached at the outer edge of the disk. The continuous increase in hardness with increasing radii can be explained by the different microstructures along the radius of the samples in both composites.

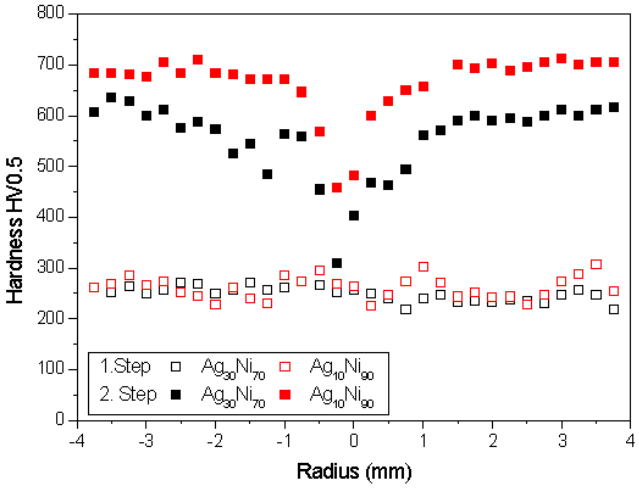

Fig.3-7 Microhardness of the $Ag_{10}Ni_{90}$ sample and $Ag_{30}Ni_{70}$ sample after the first and after the second processing step.

X-ray diffraction experiments were performed to evaluate the occurring phases after the first and second processing step. To monitor the different phases which occur during SPD more precisely, X-ray patterns were recorded every 0.5 mm starting from the center of the disk to the outer edge of the sample after the second deformation step. In Fig.3-8, the X-ray diffraction patterns of the $Ag_{30}Ni_{70}$ sample after the first and second processing step are shown. After the first processing step, peaks of the Ag phase as well as of the Ni phase are visible in the X-ray diffraction pattern. This result fits well with the images of the microstructure of the sample, where a two phase structure is clearly visible after the first processing step as well. In the second part of the figure, the diffraction patterns recorded every 0.5 mm starting from a low degree of deformation to a high degree of deformation after the second processing step are shown. At low deformation degrees, both sets of diffraction peaks are visible. With increasing amount of deformation, the intensity of the Ag peaks decreases until in the pattern recoded at the higher amounts of deformation, only face-centred cubic Ni peaks are visible. Based on the X-ray diffraction results it might be assumed that at the highest degree of deformation, Ni supersaturated solid solutions are formed. Although amorphization reactions were observed in this alloy systems processed by other methods, it could not be obtained by SPD, at least with this composition.

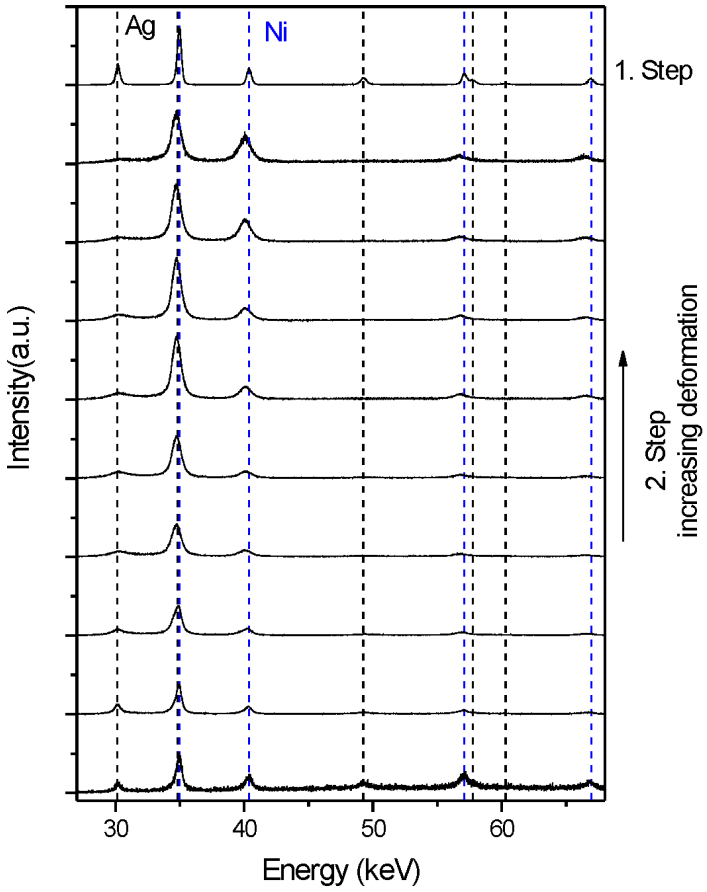

Fig.3-8 X-ray diffraction patterns of the $Ag_{30}Ni_{70}$ sample after the first and after the second processing step. After the second deformation step, X-ray diffraction patterns are recorded every 0.5 mm starting at the center of the disk to the outer edge of the sample.

Nanocrystalline Ag-Ni composite samples were produced by the two-step HPT process. It was shown that with increasing amounts of strain and with the use of the newly developed process, the formation of supersaturated solid solutions was feasible. At low degrees of deformation, two phase Ag-Ni composite samples were produced. At the highest degrees of deformation, nanostructured supersaturated solid solutions were achieved. Therefore, mechanical intermixing of Ag and Ni is possible due to SPD but no amorphization reactions were observed.

4. Summary

Very strong deformation of single phase bulk metallic materials always results in ultrafine or nanocrystalline microstructures. Nevertheless, at a certain applied strain, no further refinement of the microstructure can be observed even if continuously more and more strain is applied.

In this thesis, pure bulk Al and single phase Al-Mg alloys were investigated to determine the most important parameters which influence the minimum obtainable grain size during SPD. The results show that grain boundary migration is the main mechanism controlling the grain size during SPD and that restriction of boundary migration results in a finer saturation grain size. Grain boundary migration during SPD can be reduced by a lower deformation temperature, alloying or by the introduction of phase boundaries, as in composites. Furthermore, stable nano-particles are also efficient to generate very fine and thermally stable microstructures.

To generate these desirable microstructures, a SPD consolidation and deformation technique was applied to produce metal-metal composites as well as metal matrix composites with different reinforcement phases from initially micrometer sized metal powder mixtures. Pure powders or powder mixtures were consolidated and subsequently deformed by HPT, which was the predominantly used SPD method in this thesis.

With this HPT powder consolidation technique, Al and Ni based composites with oxides as reinforcing phases were produced. Furthermore, Cu and Ni based composites reinforced with fullerenes were fabricated. Compared to their SPD deformed pure bulk metallic counterparts, significantly finer microstructures could be reached. In fact, nanocrystalline matrix microstructures were obtained in all deformed composites. The composites also showed enhanced mechanical properties considering hardness and yield strength. Unfortunately, only the Al based composites displayed reasonable ductility during tensile testing. Furthermore, it was clearly shown that all SPD produced composites exhibit remarkable thermal stability upon annealing.

The HPT consolidation and deformation technique offers a way to generate new types of materials by bulk mechanical alloying. Metal powder mixtures of normally immiscible elements from Ag-Ni and Fe-Cu systems were HPT consolidated and deformed. By the use of a novel two step HPT process, a way to improve the efficiency of the HPT process was found. It was shown that supersaturated solid solutions with nanocrystalline microstructures were formed in both systems. Upon annealing, decomposition and the formation of nanocomposites were observed. These nanocomposites exhibit high hardness and remarkable thermal stability.

The results show that SPD powder consolidation is a fast and simple method for the production of different kinds of nanocomposites in bulk form. The simplicity of the process, the possibility of using arbitrary material combinations and the potential to scale up makes it an attractive candidate for industrial production. For a wide range of technical applications, the material dimensions of the SPD produced composites are still too small. Nevertheless, SPD can be used to obtain bulk magnetic nanocrystalline materials because in the majority of cases only small material dimensions are necessary in this application area.

4. Summary

Up to now only the mechanical properties of the produced nanocrystalline composite materials have been investigated. Further investigations must be conducted to evaluate the magnetic properties of the obtained materials.

Bibliography

[Ale98a] I.V. Alexandrov et al., Nanostruct. Mater. 10(1), 1998, 45-54

[Ale98b] I.V. Alexandrov et al., Metall. Mater. Trans. A 29(9), 2253-2260

[Bac09] A. Bachmaier et al., Scr. Mater. 61, 2009, 1016-1019

[Bac11] A. Bachmaier et al., Int. Mater. Rev., submitted

[Bot04] W.J. Botta Filho et al., Mat.Sci. Eng. A 375-377, 2010, 149-152

[Che06] M.C. Chen et al., J. Alloys Compd. 416(1-2), 2006, 169-172

[Din05] G.P. Dinda et al., Scr. Mater. 52(7), 2005, 577-582

[DiM07] R. Di Maggio et al., J. Mater. Sci .42, 2007, 9284

[Eck96] J. Eckert et al., Metall. Mater. Trans. A 27(10), 1996, 2934-2946

[Eiz08] M. Eizadjou, Comp. Sci. Technol. 68(9), 2008, 2003-2009

[Gou09] S. Goussous et al., Comp. Sci. Technol. 69(11-12), 2009, 1997-2001

[Gor06] P. Gorria et al., J. Magn. Magn. Mater. 300, 2006, 229-233

[Haf07] M. Hafok et al., Scr. Mater. 56(9), 2007, 757-760

[Hau75] J.J. Hauser, Phys. Rev. B12, 1975, 5160

[He01] J.H. He et al., Phys. Rev. Lett. 86, 2001, 2826

[Ish92] K.N. Ishihara et al., Zeitschrift für Metallkunde 83(2), 1992, 132-135

[Isl01] R.K. Islamgaliev et al., Mat. Sci. Eng. A 319-321, 2001, 872-876

[Jam11] R. Jamaati et al., Materials & Design 31(10), 2010, 4816-4822

[Kün07] A.A. Kündig et al., Scr. Mater. 56(4), 2007, 289-292

[Pre98] B. Predel: Phase Equilibria, Crystallographic and Thermodynamic Data of Binary Alloys, Group IV, Volume 5, Springer-Verlag Berlin Heidelberg New York

[Lee06] J.-M. Lee et al., Mater. Lett. 60(27), 2006, 3255-3259

[Li09a] H. Li et al., Appl. Phys. Lett. 95(7), 2009

[Li09b] H. Li et al., Mat. Sci. Eng. A 523(1-2), 2009, 60-64

[Luo04] J.-G. Luo et al., Mat. Sci. Eng. A 379(1-2), 2004, 164-172

[Luo06] J.-G. Luo et al., Mat. Sci. Eng. A 433(1-2), 2006, 334-342

[Ma93] E. Ma et al., J. App. Phys. 74(2), 1993, 955-962

[Ma01] E.Ma et al., Phys. Rev. B64, 2001

[Ma05] E. Ma, Prog. Mater. Sci. 50(4), 2005, 413-509

[Mat07] S.N. Mathaudu et al., J. Non-Cryst. Solids 353(2), 2007, 185-193

[Mun05] M.A. Munoz-Morris et al., Mat. Sci. Eng. A 396(1-2), 2005, 3-10

[Mun06] M.A. Munoz-Morris et al., Mat. Sci. Eng. A 425(1-2), 2006, 131-137

[Nis08] S. Nishimura et al., Mater. Trans. 49(1) 2008, 102-106

[Oga07] T. Ogasawara et al., Mater. Lett. 61(29), 2007, 5095-5097

[Ohs07] S. Ohsaki et al., Acta Mater. 55(8), 2007, 2885-2895

[Pip06] R. Pippan et al., Adv. Eng. Mater. 8(11), 2006, 1046-1055

[Pip10] R. Pippan et al., Annu. Rev. Mater. Res. 40, 2010, 319-343

[Raa10] D. Raabe et al., MRS Bull. 35, 2010, 982-991

[Rat11] G.B. Rathmayr et al., Acta Mater., submitted

[Rös07a] H. Rösner et al., J. Mater. Sci. 42(5), 2007, 1772-1781

[Rös07b] H. Rösner et al., J. Non-Cryst. Solids 353(32-40), 2007, 3777-3781

[Sab05] I. Sabirov et al., Scr. Mater. 52(12), 2005, 1293-1298

[Sau05a] X. Sauvage et al., Acta Mater. 53(7), 2005, 2127-2135

[Sau05b] X. Sauvage et al., Mat. Sci. Eng. A 410-411, 2005, 345-347

[Sau08a] X. Sauvage et al., Scri. Mater. 58(12, 2008, 1125-1228

[Sau08b] X. Sauvage et al., Mater. Sci. Forum 584-586, 2008, 306-309

[Sar07] M. Saravanan et al., Comp. Sci. Technol. 67(6), 2007, 1275-1279

[Sch11] S. Scheriau et al., Mat. Sci. Eng. A 528(6), 2011, 2776-2786

[Sen98] O.N. Senkov et al., Nanostruct. Mater. 10(5), 691-698

[Sha10] H.S. Shahabi, Mat. Sci, Eng. A 527(21-22), 2010, 5790-5795

[Sor08] J. Sort et al., Adv. Funct. Mater. 18(20), 2008, 3293-3298

[Sto03] V.V. Stolyarov et al., Mat. Sci. Eng. A 357(1-2), 2003, 159-167

[Stü03] H.P. Stüwe, Adv. Eng. Mater. 5(5), 2003, 291-295

[Sue08] K. Suehiro et al., J. Mater. Sci.c43(23-24), 2008, 7349-7353

[Sun07] Y.F. Sun et al.,Mater. Trans. 48(7), 2007, 1605-1609

[Sun10a] Y.F. Sun et al., J. Alloys Compd. 504(S1), 2010, S443-S447

[Sun10b] Y.F. Sun et al., J. Alloys Compd. 492(1-2), 2010, 149-152

[Tch04] V.V. Tcherdyntsev et al., Mat. Sci. Eng. A375-377, 2004, 888-893

[Tep95] V.A. Teplov et al., Nanostruct. Mater. 6(1-4), 1995, 437-440

[Tia10] Y.Z. Tian et al., Scr. Mater. 63(1), 2010, 65-68

[Tok08a] T. Tokunaga et al., Mat. Sci. Eng. A 490(1-2), 2008, 300-304

[Tok08b] T. Tokunaga et al., Scr. Mater. 58(9), 2008, 735-738

[Val98] R.Z. Valiev et al., Scr. Mater. 40(1), 1998, 117-122

[Val00] R.Z. Valiev et al., Prog. Mater. Sci. 45, 2000, 103-189

[Val06] R.Z. Valiev et al., JOM 58(4), 2006, 34

[Vis06] V. Viswanathan et al., Mat. Sci. Eng. R 54(5-6), 2006, 121-285

[Yav02] A.R. Yavari et al., Scr. Mater. 46(10), 2002, 711-716

[Xu96] J. Xu et al., J. Appl. Phys. 79, 1996, 3935

[Xu99] C.L. Xu et al., Carbon 37(5), 1999, 855-858

[Zeh04] M.J. Zehetbauer and R. Z. Valiev: Nanomaterials by severe plastic deformation, Wiley-VCH, Weinheim, Germany, 2004

[Zho03] R. Zhong, Carbon 41(4), 2003, 848-851

[Zhu04] Y. Zhu et al., Scr. Mater. 51 (8), 2004, 825

List of appended publications & proceedings

[A] A. Bachmaier, M. Hafok, R. Pippan, Rate independent and rate dependent structural evolution during severe plastic deformation, Materials Transactions, 51(1) 8-13.

[B] A. Bachmaier, M. Hafok, R. Schuster, R. Pippan, Limitations in the refinement by severe plastic deformation: the effect of processing, Reviews on Advanced Material Science, 25 (2010) 16-22

[C] A. Bachmaier, A. Hohenwarter, R. Pippan, New procedure to generate stable nanocrystallites by severe plastic deformation, Scripta Materialia, 61 (2009) 1016-1019

[D] A. Bachmaier, R. Pippan, Effect of oxide particles on the stabilization and final microstructure in aluminium, Materials Science and Engineering A, 528 (2011), 7589-7595

[E] A. Bachmaier, R. Pippan, Microstructure and properties of a Fe-Cu composite processed by High-Pressure Torsion powder consolidation, Materials Science Forum, 667-669 (2011) 229-234

[F] A. Bachmaier, R. Pippan, The formation of supersaturated solid solutions in Fe-Cu alloys deformed by High-pressure torsion, submitted

Remarks

In the appended papers, I, Andrea Bachmaier performed all experiments, data analyses and was the primary author with the following exceptions:

- Georg Hübler helped in sample preparation and experimental work for Publication D, E and Publication F, respectively.
- Martin Hafok performed part of the experiments and data analysis of results of Publication A and B.
- Michael Kerber and Erhard Schafler conducted X-ray diffraction experiments for publication F.
- Roman Schuster and Erhard Schafler performed X-ray diffraction experiments for publication B.
- Daria Setman conducted Differential Scanning Calorimetry experiments for publication F.
- Georg B. Rathmayr conducted sample preparation with the Focused Ion Beam workstation for publication D.
- Josef Keckes performed X-ray diffraction experiments on Ag-Ni samples.
- Zaholi Zhang carried out transmission electron microscopy on Cu and Ni samples.
- Reinhard Pippan, my supervisor, contributed to all publications with principal ideas from design of experiments to final analysis and interpretation of results.

In order to stay with the published versions, no modifications according to British English and American English have been made.

Publication A: Rate independent and rate dependent structural evolution during severe plastic deformation

Rate independent and rate dependent structural evolution during severe plastic deformation

Andrea Bachmaier[a], Martin Hafok[b] and Reinhard Pippan[a]

[a] Erich Schmid Institute of Materials Science of the Austrian Academy of Sciences, Jahnstrasse 12, A-8700 Leoben, Austria

[b] Present address: Boehler Edelstahl GmbH&Co KG, 8605 Kapfenberg, Austria

Abstract

High pressure torsion (HPT) deformation enables the grain refinement of bulk materials until a saturation region is reached where no further microstructural refinement can be observed. The influence of deformation temperature, alloying and strain rate on the saturation region was examined by using pure aluminium, an Al-1 mass% Mg alloy and an Al-3 mass% Mg alloy. The deformation temperature was varied between -196°C and 450°C. Both, temperature and alloying exhibit a pronounced influence on the saturation microstructure. The measurements reveal either a rate independent behavior of the structural evolution at low temperatures and a rate dependent behavior of the structural evolution at high temperatures. Two different processes are proposed to be the reason for the saturation at low and high homologous temperatures.

Keywords

aluminium alloy, high pressure torsion, saturation, grain boundary migration, strain rate

Introduction

Severe plastic deformation (SPD) is well known to allow the grain refinement of bulk materials. An ultra fine grained or even nanocrystalline microstructure is formed by SPD with a high fraction of high-angle boundaries [A1-4]. At strains larger than a critical value, no further microstructural refinement can be observed and a saturation region is reached which also manifests in a stagnation in hardening of the material. This general behaviour is independent of the material and the processing parameters in single phase materials. Only the minimum size of the crystallites in the saturation and the necessary strain to reach the saturation are influenced by the material. The initial process of fragmentation as well as the most important parameters influencing the grain refinement are well documented in literature [A5-10]. The grain refinement process is especially influenced by the temperature, alloying, the strain rate and the deformation path [A11]. Although these major parameters controlling the grain refinement are well known, there still exists no clear explanation for the question how an increasing strain can lead to a steady state in the microstructure and the hardening of a material. To maintain a saturation microstructure, a balance in the structural restoration process must be kept: the same number of dislocations have to be eliminated as produced by the applied strain. In addition, the annihilation and generation of boundaries have to be also in balance. The generation of new boundaries can be caused by a simple increase of boundary length due to an elongation of the grains and by the formation of new boundaries from dense dislocation walls. The reduction in boundary length requires a movement of boundaries.
At very large strains, when the saturation in strength and microstructural refinement is observed, it is evident that the generation and restore mechanisms are in equilibrium. However, the details of the phenomena are not well understood. Temperature and alloying should affect the processes significantly. Therefore both parameters are varied in a wide range in an Al alloy.
In this study, we used aluminium, an Al-1wt%Mg alloy and an Al-3wt%Mg alloy in order to investigate the influences of deformation temperature, alloying and strain rate on the saturation region during HPT deformation. The low melting temperature of the Al alloy allows the deformation at homologous temperatures ranging from 0.1-0.8 Tm (Tm being the melting temperature).

Experimental

Samples for HPT deformation were cut out of an aluminium (99.99% purity), an Al-1wt%Mg and an Al-3wt%Mg alloy plate. A detailed description of the HPT equipment used for processing the materials present in this paper is given in [A6]. The disk-shaped specimens with a diameter of 14 mm and a height of approximately 0.8 mm are pressed between two anvils, which can be heated or cooled to allow SPD at temperatures between -196°C and 500°C. Furthermore, the rotation speed of the anvils can be varied over a wide range. The direct measurement of the torque applied to the sample is also possible, which can be used to estimate the change in the flow stress of the material in-situ during deformation.

The shear strain can be calculated according to

$$\gamma = \frac{2\pi n}{t} r$$

whereby r, n, t are the distance from the center of the sample, the number of revolutions and the thickness of the sample, respectively. As the strain is dependent on the radius, all strains and strain rates were calculated for a radius of 6 mm. The thickness t is calculated according to $t=(t_i+t_a)/2$ whereby t_i and t_a are the thickness of the sample before and after the deformation, respectively.

The HPT deformation was performed in three different ways: First of all the deformation was performed at constant, but different temperatures ranging from -196°C to 450°C with the rotation speed kept constant. In addition to the constant temperature experiments, cooling experiments were performed. The samples were heated up and kept at a constant temperature of 450°C for about 5 minutes. Afterwards, the deformation with constant, but different rotation speeds was started until a constant torque was measured. Subsequently, the heating device was turned off and the sample cooled down during continued deformation. During the cooling of the sample the change in torque was measured. Additionally, similar experiments during heating from cryogenic temperatures were performed. In the third set of experiments, the samples were heated to constant, but different temperatures between -196°C and 450°C. Afterwards the HPT deformation was started with a high rotation speed (0.48 rpm) until a constant torque was measured. During the ongoing deformation, the rotation speed was immediately decreased to the lowest possible rotation speed (0.016 rpm) and the change of the torque was measured.

Microstructures were characterized in a scanning electron microscope (SEM) type LEO 1525 using back scattered electrons (BSE) and the microtexture was investigated by electron back scatter diffraction (EBSD) using the EBSD system attached to the SEM. The micrographs were taken at radii of approximately 6 mm on the shear plane of the sample (see Fig.A3). Grain size determination was performed on BSE micrographs. Vickers microhardness measurements were performed with a BUEHLER Mircomet 5100 using a load of 500 g.

Results

3.1. Influence of deformation temperature

The influence of the deformation temperature on the saturation region was examined in HPT deformation experiments at different but constant temperatures.

The torque applied during the HPT deformation of the Al-3wt%Mg alloy versus the applied strain is shown in Fig.A1(a). The strain is calculated for a radius of 6 mm. The HPT deformation was conducted with a constant rotation speed (0.48 rpm). The alloy was deformed at -196°C, room temperature, 150°C, 250°C, 350°C and 450°C until a constant torque was measured indicating that the saturation region was reached. Because the measured torque can be influenced by several experimental parameters, the same experimental conditions were used for these experiments to make a comparison of the measured torque feasible.

All recorded torque curves show a similar behavior: at low strains the torque increases until at a certain shear strain a saturation torque is reached. It can be clearly seen that the deformation temperature affects the saturation torque and the onset strain of saturation of the Al-3wt%Mg alloy. Increasing the deformation temperature lowers the saturation torque and the saturation shear strain. Fig.A1(b) compares the applied torque during HPT deformation of the Al-1wt%Mg alloy and the Al-3wt%Mg alloy at room temperature. The effect of alloying can be clearly seen: Deformed at room temperature, the Al-1wt%Mg alloy exhibits a significantly lower saturation torque than the Al-3wt%Mg alloy.

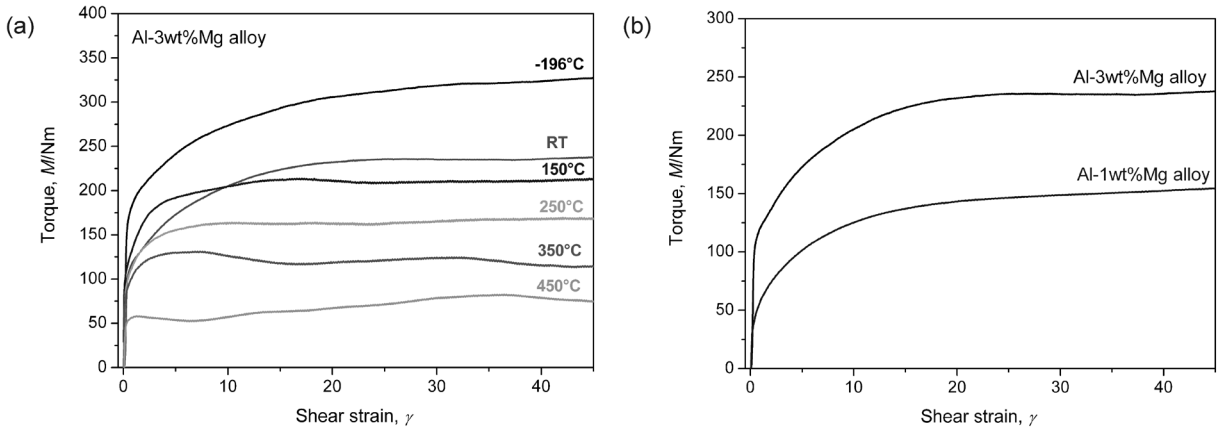

Fig. A1 (a) In-situ torque measured during the deformation of the Al-3wt%Mg alloy vs. the shear strain at a strain rate of 0.4 s^{-1} (0.48 rpm). The deformation temperature was varied between -196°C and 450°C. (b) Comparison between the in-situ torques measured during the deformation of the Al-1wt%Mg and Al-3wt%Mg alloy at room temperature. The strain rate during deformation was 0.4 s^{-1} (0.48 rpm).

Fig.A2 shows the development of the saturation microstructure of the Al-3wt%Mg alloy samples. BSE micrographs of the Al-3wt%Mg alloy deformed at -196°C, 200°C, 300°C and 450°C at a strain rate of 0.2 s^{-1} (rotation speed: 0.25 rpm) were recorded. For all samples, the applied strain and the deformation conditions were chosen for the microstructure to be in the saturation regime. It is evident that the steady-state size of the structural elements increases with increasing temperature. The first micrograph show a sample which was deformed at -196°C. It shows elongated grains, which are aligned in tangential direction. This direction coincides with the shear direction during the HPT deformation. The average size of the structural elements is approximately 120 nm in the tangential direction and about 70 nm in the direction of the torsion axis. With rising temperature the size of the structural element increases and a change in the microstructure occurs. The grains become more equiaxed and the alignment in the tangential direction loses its significance. At 450°C, a more or less equiaxed microstructure can be observed and a further increase in the size of the structural element with increasing temperature is measured. Furthermore, the grain boundaries become more defined at higher temperatures. The transition between these two kinds of morphologies occurs in a temperature range between 300°C and 350°C.

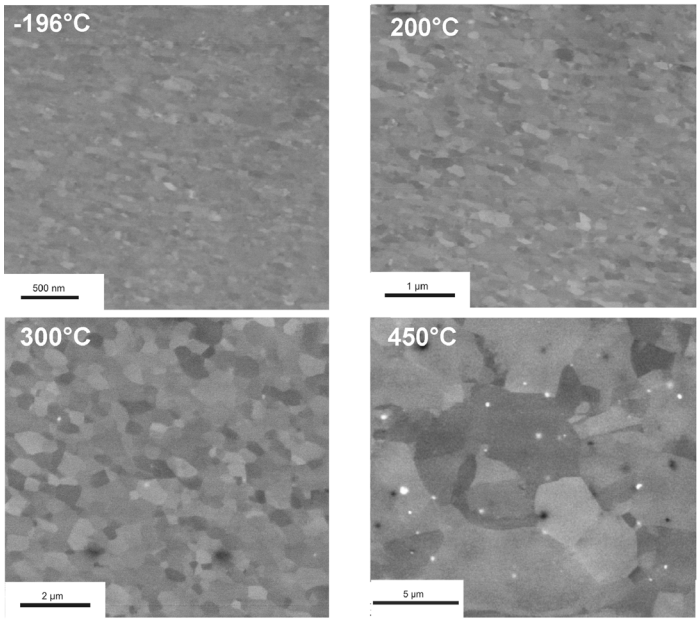

Fig.A2 Microstructure on the shear plane of the Al-3wt%Mg alloy samples deformed at -196°C, 200°C, 300°C and 450°C at a strain rate of 0.2 s^{-1} (0.25 rpm).

Fig.A3 shows the development of the microtexture of the Al-3wt%Mg alloy samples deformed at 200°C, 300°C and 450°C at the same strain rate as used before. Considerable differences in the obtained microtexture can be observed. The pole figure of the sample deformed at 200°C shows a shear texture which is typical for HPT, but also comparable to face-centered cubic (fcc) materials that underwent cold deformation13. The microtexture becomes considerably pronounced at 300°C and a certain alignment of the crystal system with respect to the deformation state is apparent. The torsion axis lays parallel to the (111) glide plane and the [011] glide direction is aligned in the shear direction. On the contrary, the pole figure of the sample deformed at 450°C shows a different microtexture where the glide plane changes from the (111) to the (112) plane.

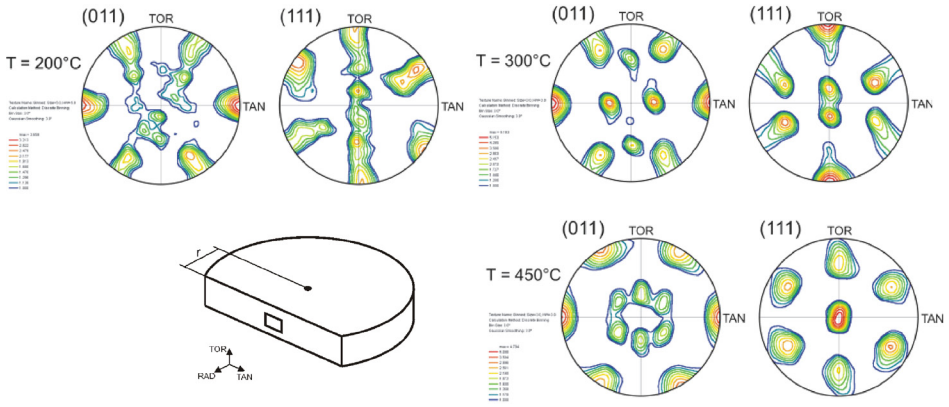

Fig.A3 Microtexture recorded in the center of the cut plane at a radius of 6 mm of the Al-3wt%Mg alloy samples deformed at 200°C, 300°C and 450°C at a strain rate of 0.2 s^{-1} (0.25 rpm). The direction of observations is also shown as an inset. The axes are denoted as TOR, RAD and TAN for the torsion, radial and tangential direction.

Fig.A4 summarizes the development of the size of the structural elements and the measured microhardness as function of the deformation temperature for both aluminium alloys. The microhardness of the Al-3wt%Mg alloy samples decreases with increasing deformation temperature. The sample deformed at -196°C exhibits the highest hardness values of 1.75 GPa, whereas the lowest hardness values of 0.67 GPa were measured for the sample deformed at 450°C. At room temperature the microhardness of the Al-3wt%Mg alloy is about 1.48 GPa. Compared to the Al-3wt%Mg alloy sample, the Al-1wt%Mg alloy sample deformed at room temperature shows a lower microhardness (1.13 GPa). The microhardness values are in good accordance with the determined size of the structural elements: With decreasing deformation temperature the size of the structural elements is reduced whereas the determined size of the structural elements of the Al-1wt% Mg sample deformed at room temperature is clearly larger than those of the Al-3wt% Mg alloy sample.

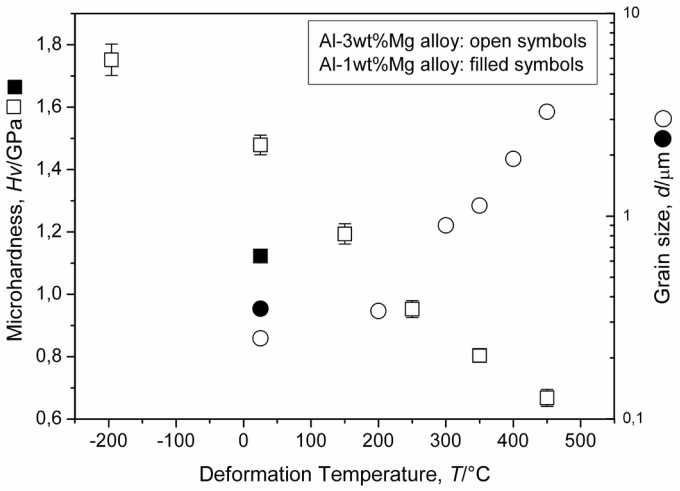

Fig.A4 Microhardness Hv and size of structural elements after HPT deformation of the Al-3wt%Mg alloy at different temperatures and of the Al-1wt%Mg alloy at room temperature determined from BSE micrographs.

3.2. Influence of strain rate

To investigate the influence of the strain rate on the saturation region during HPT deformation, experiments with different rotational speeds (0.05 rpm – 0.50 rpm) were performed as well.

During cooling and heating experiments, the influence of the strain rate in a temperature range from -196°C to 450°C for the Al-3wt%Mg alloy and for comparison, of pure aluminium was examined. In Fig.A5(a) the results of the torque measurements are shown. With increasing temperature the measured torque and therefore, the flow stress of both materials decreases. Comparing the alloy and the pure aluminium, the measured torque for pure aluminium is lower. At room temperature, the aluminium alloy shows only a low strain rate sensitivity. Between room temperature and 450°C, the Al alloy exhibits a certain strain rate sensitivity. Fig.A5(b) shows the microstructure of Al-3wt%Mg alloy samples deformed at 200°C at two different rotation speeds (0.05 rpm and 0.50 rpm). It can be clearly seen that an increase in strain rate leads to a smaller size of the structural elements in the saturation

region. Nevertheless the effect of the strain rate on the saturation size of the structural elements is less pronounced than the effect of the deformation temperature.

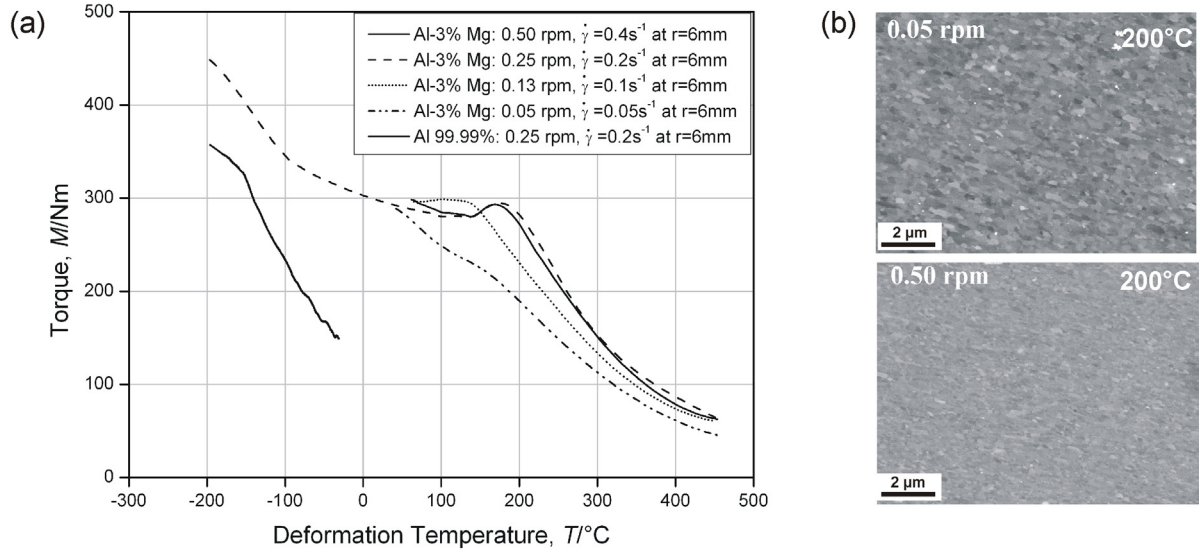

Fig.A5 (a) In-situ torque measured during cooling and heating experiments at different rotation speeds ranging from 0.05 rpm to 0.50 rpm (strain rate of 0.05 s^{-1} to 0.4 s^{-1}). (b) BSE micrographs showing the microstructure of the Al-3wt%Mg alloy deformed at 200°C at two different rotation speeds.

Furthermore the aluminium alloys were HPT deformed at different deformation temperatures, but now the rotation speed was directly changed during the deformation. In the beginning, the samples were deformed with the highest possible rotation speed until saturation in the measured torque curve was observed. Afterwards, the rotation speed was abruptly changed from 0.48 rpm to 0.016 rpm and changes in the measured torque curves were directly recorded. Fig.A6(a) shows the results of these measurements. The fluctuation of the torque is due to the inaccuracy of the alignment of the HPT tool. For the samples deformed at room temperature and -196°C no change in the measured torques were recorded at the moment of reducing the strain rate. The drop in the torque of the sample deformed at -196°C results from a short unscheduled stop of the rotation at the time of the strain rate shifting. Moreover, the strain rate sensitivity at higher temperatures could be further confirmed in this experiment. Changing the strain rate during the deformation at 150°C and 250°C leads to a significant decline in the measured torques. The torque increases somewhat until a constant torque is measured again after a short time. The same behaviour can be observed during the deformation at 350°C and 450°C, although the drop in the measured torques is less pronounced at higher temperatures. Similar shapes of the flow curves by the time of strain rate changes in the steady state flow regime are found in conventional hot working as well. We assume a similar process in the case of HPT deformation at elevated temperatures, although the accurate processes are not completely clear and require further research. Fig.A6(b) compares the relative steady state torques differences (ΔM) as function of the different deformation temperatures for both strain rates. ΔM is calculated according to ΔM = (M2-M1)/(M1) whereby M1 and M2 are the measured steady state torques at the high and low rotation speeds,

respectively. Comparing ΔM, a decrease of the strain rate has hardly an influence on the steady state torque at room temperature and lower temperatures, but the influence of the strain rate increases significantly at higher deformation temperatures.

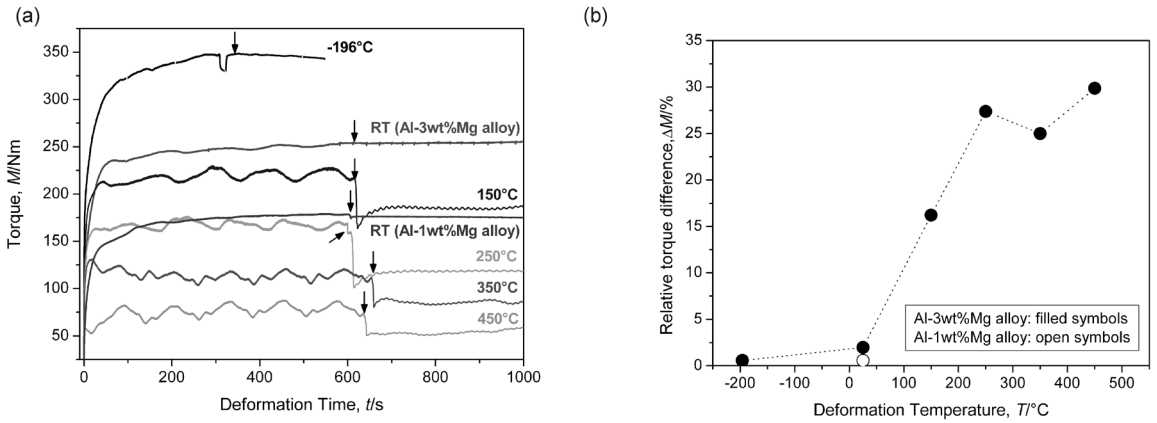

Fig.A6 (a) In-situ torque curves measured during the deformation of the Al-3wt%Mg alloy at different temperatures. The in situ-torque curve of the Al-1wt%Mg alloy which experiences the same strain rate variation is also shown. The times of rotation speed shifting are indicated by an arrow. (b) Relative torque difference ΔM= (M2-M1)/ (M1) for the two different strain rates as function of the deformation temperature of the Al-1wt%Mg alloy and the Al-3wt%Mg alloy. M1 and M2 are the measured torques for the high (0.48 rpm) and low rotation speed (0.016 rpm), respectively.

Discussion

In general, all investigated deformation conditions yield to a saturation of both, the structural element size and the flow stress, at large applied strains. The deformation temperature is one major parameter affecting the final size of the structural elements in the saturation. With decreasing deformation temperature, the size of the structural elements continuously decreases. Moreover, the deformation temperature influences the amount of strain which must be applied to reach the saturation regime and the saturation torque itself. Both parameters distinctly decrease with increasing deformation temperature. Similar behavior is also found in conventional hot working [A14-16]. The second important parameter affecting the size of the structural elements in the saturation and the saturation torque is alloying. It causes significant reduction of the saturation size of the structural elements and therefore leads to an increase in the saturation torque.

Another parameter which has an effect on the saturation torque is the strain rate. Nevertheless, the experiments have shown that the saturation torque is influenced by the strain rate only in a certain temperature region. In deformation experiments at and below room temperature nearly no strain rate sensitivity is observed. In contrast to the low strain rate sensitivity at low temperatures, an enhanced strain rate sensitivity is observed at deformation temperatures ranging from room temperature to approximately 450°C. In the whole strain rate sensitive regime, the strain rate has also an effect on the size of the structural elements whereby an increase of the strain rate results in a smaller size of the structural elements.

Furthermore, the microstructural investigations indicated a definite change in the morphology of the saturation microstructure depending on the deformation temperature. The microstructure consists of elongated grains aligned in the shear direction however with certain inclination at low deformation temperatures. This shape of the grains is maintained up to a deformation temperature of approximately 300°C. At higher deformation temperatures, a completely different morphology of the microstructure develops. The shape of the grains is now equiaxed and no explicit alignment in any direction can be observed. Increasing deformation temperature not only alters the microstructural features, it also changes the microtexture in the saturation region. At low deformation temperatures, the typical shear texture after HPT deformation is received. This texture is similar to those obtained for fcc materials after cold deformation [A13]. At higher deformation temperatures, the texture becomes more pronounced whereby the torsion axis is parallel to the glide plane (111) and the shear direction lays in the direction of the glide direction [110]. If the deformation temperature is further increased, the glide plane changes from (111) to the (112) plane, but the glide direction remains unchanged. To maintain a steady state during continuous HPT deformation a mechanism for the elimination of dislocations must exist because new dislocations are constantly produced as long as an external strain is applied. In hot working, a steady state can be reached by dynamic recrystallization which is a diffusion-controlled process enhanced by temperature [A8,A16-18].

Based on the in situ measurements of the torque curves, the microstructural and the microtextural investigations, we assume that two different processes active at low and high temperatures enable the steady state during HPT deformation.

At high temperatures we assume that a certain type of dynamic recrystallization [A19,A20] is responsible for the occurrence of the observed steady state at large strains. In general, boundaries are mobile and annihilate each other which finally lead to an equiaxed microstructure with mainly high-angle boundaries. Although the exact processes governing the movement of the boundaries are not clear in the case of HPT deformation, the driving force for the boundary migration seems be the reduction of the density of dislocations and the rate determining step the mobility of the boundaries. Because dynamic recrystallization is a diffusion-controlled process, it is enhanced by deformation at high homologous temperatures and influenced by the strain rate as well. The temperature dependence of the size of the structural elements in the saturation, the strain rate sensitivity and influence of the deformation temperature on the onset of the steady state during HPT deformation at high homologous temperatures would encourage this assumption. The morphology of the grains and the microtextural change in the saturation region at high deformation temperatures corroborates this further.

At low temperatures, we assume a process similar to dynamic recrystallization to maintain the steady state. In ultrafine grained and nanocrystalline metals, stress-induced grain boundary migration is proposed as an alternative plasticity mechanism at ambient and low temperatures [A21-23]. Although there exists a certain temperature dependence, the influence of the deformation temperature is not as high as in the high temperature regime. Furthermore there exists hardly any strain rate sensitivity. The driving force for the boundary migration in this case does not seem to be the reduction of dislocation density, but rather stress induced by means of the external applied strain and strain induced through

the stress field of the dislocations. Due to the reduced thermal mobility, the formation of an equiaxed microstructure is not possible.

Conclusion

In the present paper, the influence of the deformation temperature and the strain rate on the saturation region during severe plastic deformation were examined by deforming aluminium alloys at homologous temperatures ranging from 0.1-0.8 Tm.
The results are summarized as followed:

- HPT deformation of aluminium alloys leads to a steady state for all investigated deformation conditions.
- Deformation temperature and alloying are the two major parameters influencing the minimum size of the structural elements in the saturation and the onset of the steady state.
- The measurements reveal either a rate independent or a rate dependent behavior of the structural evolution depending on the temperature during deformation.
- A process similar to dynamic recrystallization is proposed to be the reason for the steady state at high homologous deformation temperatures. At low homologous deformation temperatures a typical severe plastic deformation behavior is observed, where the maintenance of the steady state is facilitated by stress and strain induced boundary migration.

Acknowledgment

The financial support by the Austrian Fonds zur Förderung der wissenschaftlichen Forschung (Project number: S10402-N16) is gratefully acknowledged.

References for Publication A

[A1] M.J. Zehetbauer and R.Z. Valiev: Nanomaterials by Severe Plastic Deformation, (Wiley-VCH, Weinheim, Germany, 2004).

[A2] R.Z. Valiev, R.K. Islamgaliev, I.V. Alexandrov: Prog. Mater. Sci. 45 (2000) 103-189.

[A3] T.C. Lowe and R.Z. Valiev, JOM 56(10) (2004) 64-68.

[A4] Y.T. Zhu and T.G. Langdon: JOM 56(10) (2004) 58-63.

[A5] T. Hebesberger, H.P. Stüwe, A. Vorhauer, F. Wetscher, R. Pippan: Acta Mater. 53 (2005) 393-402.

[A6] A. Vorhauer, S.Kleber, R.Pippan: Mater. Sci. Eng. 281 (2005) 410-411.

[A7] A. Vorhauer, W. Knabl, R. Pippan: Mater. Sci. Forum 426-432 (2003) 2747.

[A8] N. Hansen: Metall. Mater. Trans. 32A (2001) 2917.

[A9] N. Hansen, D. Kuhlmannnn-Wilsdorf: Mater. Sci. Eng. 81 (1986) 141.

[A10] E. Schafler, R. Pippan: Mater. Sci. Eng. A387-389 (2004) 799.

[A11] R. Pippan, F. Wetscher, M. Hafok, A. Vorhauer, I. Sabirov: Adv Eng Mater 8 (2006), 1046.

[A12] H. Matsunaga and Z. Horita: Mater. Trans. 50(7) (2009), 1633-1637.

[A13] G. R. Canova, U. F. Kocks, J. J. Jones: Acta Metall. 32 (1984), 211.

[A14] H.P. Stüwe: Proc. Conf. Deformation Under Hot Working Conditions, (The Iron and Steel Institute, London, 1968) 2-6.

[A15] Y. Zhang, X. Zeng, C. Lu, W. Ding: Mat. Sci. Eng. A 428 (2006) 91-97.

[A16] F.J. Humphreys and M. Hatherly: Recrystallization and Related Annealing Phenomena, (Elsevier, United Kingdom, 2004).

[A17] R. Sandstorm and R. Lagneborg: Acta Metall. 23 (1975) 387.

[A18] W. Roberts and B. Ahlborn: Acta Metall. 26 (1978) 801.

[A19] M. E. Kassner and S. Barrabas: Mat. Sci. Eng. A 410-411 (2005) 152-155.

[A20] S. Gourdet and F. Montheillet: Mat. Sci. Eng. A 283 (2000) 274-288.

[A21] M. Legros, D.S. Gianola, K.J. Hemker: Acta Mater. 56 (2008), 3380-3393.

[A22] F. Mompiou, D. Caillard, M. Legros: Acta Mater. 57 (2009) 2198-2209.

[A23] D. Caillard, F. Mompiou, M. Legros: Acta Mater. 57 (2009) 2390-2402.

Publication B: Limitations in the refinement by severe plastic deformation: the effect of processing

Limitations in the refinement by severe plastic deformation: the effect of processing

A. Bachmaier[1], M. Hafok[1], R. Schuster[2] and R. Pippan[1,3]

[1] Erich Schmid Institute of Materials Science of the Austrian Academy of Sciences, Jahnstraße 12, A-8700 Leoben, Austria

[2]Institute of Materials Physics, University of Vienna, A-1090 Wien, Austria

[3] CD Laboratory of Local Analysis of Deformation and Fracture, Jahnstraße 12, A-8700 Leoben, Austria

Abstract

High Pressure Torsion (HPT) is a simple and effective severe plastic deformation method to produce ultrafine grained or even nanocrystalline microstructures. However, at a certain applied strain no further refinement of the microstructure occurs. HPT deformation of bulk Ni at room temperature leads to a typical saturation microstructure with a mean grain size of approximately 200 nm. In the present work, it will be shown that additional heavy cold rolling of a saturation microstructure does not help to overcome this limit. Furthermore, a strategy to bypass this limitation in the grain refinement using HPT deformation is presented. The main key lies in the reduction of grain boundary migration during the deformation. Thus bulk nanocrystalline Ni samples with an average grain size below 30 nm can be produced.

Introduction

Severe plastic deformation is a well known procedure for producing significant grain refinement in bulk materials. High pressure torsion (HPT) is one of these severe plastic deformation techniques which allows the application of a large amount of strain in a simple way.

In literature, a lot of reports concerning the HPT deformation of bulk Ni and the structural evolution during the deformation can be found [B1-4]. If a high enough amount of strain is applied, a saturation in the refinement process occurs and a microstructure with a mean grain size of approximately 200 nm can be obtained by HPT deformation of Ni at room temperature. Once this so-called saturation region is reached, it is impossible to further decrease the grain size by processing the samples to higher strains if the HPT deformation is conducted at room temperature [B3,B5,B6]. Nevertheless, the deformation temperature as well as the purity of the processed material influence the size of the grains in the saturation region [B4].

If HPT is applied to Ni single crystals, a similar saturation microstructure is reached [B7,B8]. The limitation in the refinement becomes even more clearly visible if HPT deformation is applied to Ni which has an initial nanocrystalline structure with a mean grain size of approximately 20 nm [B9]. The HPT deformation induces grain growth and the nanocrystalline structure is transformed into an ultrafine grained structure with a final grain size of approximately 200 nm.

Independent of the initial state of the material before the HPT deformation, always the same saturation grain size is reached in the aforementioned examples. It apparently seems to be impossible to overcome the limit in the structural refinement during HPT deformation of pure bulk Ni.

Nevertheless, Ni with an average grain size less than 10 nm has been produced by a repeated rolling and folding process [B10,B11]. Although the applied amount of strain is similar during HPT, the minimum grain size in Ni obtained by the repeated rolling and folding process is more than one order of magnitude finer than that in HPT processed Ni.

The present work is devoted to the question if a different strain path like in the repeated rolling and folding process leads to a different saturation grain size. Moreover a way to further reduce the minimum grain size achievable by HPT deformation is presented.

Experimental

A detailed description of the HPT equipment used for processing the materials present in this paper is given in [B12]. The shear strain γ_{HPT} during HPT deformation can be calculated according to

$$\gamma_{HPT} = \frac{2\pi n}{t} r \qquad (1)$$

whereby r, n, t are the distance from the center of the sample, the number of rotations and the thickness of the sample, respectively. The von Mises equivalent shear strain εv_{HPT} is then given by [B13]

$$\varepsilon_{VHPT} = \frac{\gamma_{HPT}}{\sqrt{3}} \quad (2)$$

Disk shaped Ni (99.5 %) samples with a diameter of 30 mm and a height of 10 mm were HPT deformed at room temperature for 10 rotations. This corresponds to a εv_{HPT} of 32 at a radius of 14 mm. The pressure during the deformation was 2.8 GPa and the rotation speed was kept constant at 0.2 rpm. The thus processed material is denoted as initial HPT state. A part of these HPT deformed bulk Ni samples was further treated by the following methods.

State 1 was obtained by cold rolling of the HPT deformed bulk Ni sample in a single standard cold rolling mill with 83% thickness reduction after the HPT deformation. State 2 was achieved by the same cold rolling process of the HPT deformed bulk Ni sample with 96% thickness reduction. To evaluate the additional amount of strain, the von Mises equivalent strain for rolling deformation, ε_{CR}, was calculated by

$$\varepsilon_{CR} = \frac{2}{\sqrt{3}} \ln\left(\frac{t_o}{t_f}\right) \quad (3)$$

whereby t_o and t_f are the thickness of the sample before and after the cold rolling, respectively. The calculation of the additional amount of equivalent strain for rolling deformation gives a ε_{CR} of 2.1 and 3.7 for State 1 and 2, respectively. The total strain ε for State 1 and 2 is calculated by the addition of εv_{HPT} and ε_{CR}. State 1 was deformed to a ε of 34.1 and State 2 to a ε of 35.7 if the von Mises equivalent shear strain εv_{HPT} of the initial HPT deformed sample is calculated at a radius of 14 mm. If one considers a volume element at a radius of 7 mm εv_{HPT} is 16 and the total strain ε is 18.7 and 19.7 for State 1 and 2, respectively.

Furthermore, Nickel powder (99.9%, 3-7 microns from Alfa Aesar®) which was additionally annealed before the compaction was processed by HPT. The precompacted samples with a diameter of 14 mm and a thickness t of 0.8 mm were deformed by HPT at room temperature. The pressure during deformation was 5 GPa and the rotation speed was kept constant at 0.2 rpm.

Microstructures were characterized in a scanning electron microscope (SEM) type LEO 1525 using back scattered electrons and in a transmission electron microscope (TEM) type Philips CM12. The microtexture was investigated by electron back scatter diffraction (EBSD) using the EBSD system attached to the SEM. The direction of observation is given in Fig.B1a. All microstructural investigations in the cold rolled sheets were carried out on the normal direction (ND)- rolling direction (RD) planes. Vickers microhardness measurements were performed on a BUEHLER Mircomet 5100 using a load of 1000 g.

The HPT Ni powder consolidated samples have been subjected to multi reflection X-ray line profile analysis using synchrotron radiation available at the Synchrotron ELETTRA, Trieste, Italy. From the crystallite size distribution, which can be described by a log-normal function, the area weighted mean crystallite size $\langle x \rangle_{area}$ was obtained [B14].

Results and discussion

In the case of HPT deformation of pure Ni, a saturation in the refinement is observed between an equivalent shear strain εv_{HPT}=8 and 16 [B5]. The deformation condition and the applied strain were chosen for the microstructure to be in the saturation region for all samples. The Ni discs were deformed by HPT at room temperature to a corresponding equivalent shear strain εv_{HPT} of 32 at a radius of 14 mm. The resulting saturation microstructure after the HPT deformation in tangential direction at a radius of 14 mm is shown in Fig.B1b. The micrograph shows a typical saturation microstructure. In tangential and axial direction, the grains have an equiaxed shape within the saturation region. In radial direction, an elongation of the grains with a preferred direction of the grains somewhat inclined in the shear direction can be observed [B5]. Grain sizes were measured by linear intersection method in horizontal and vertical direction. The mean grain size using this approach in horizontal and vertical direction is 225 nm and 227 nm, respectively. It is important to notice that the grain size cannot be decreased further by applying higher strains once the saturation region is reached.

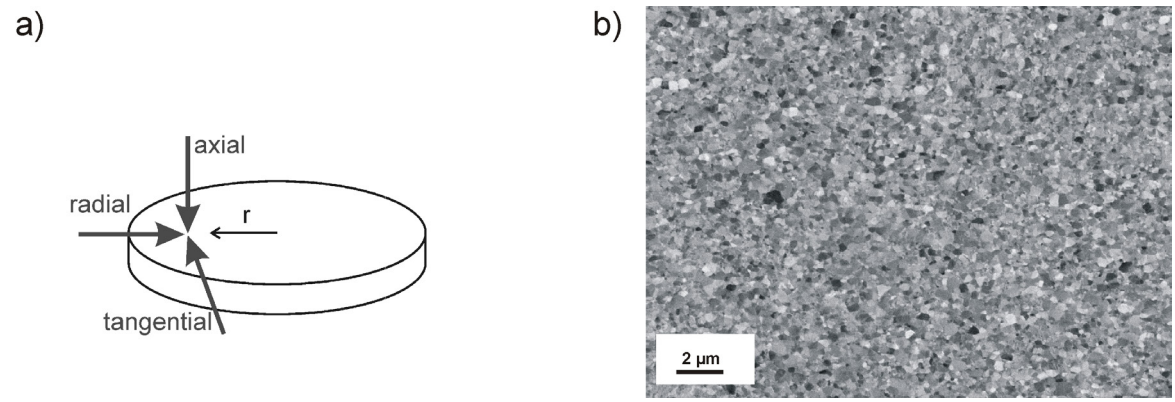

Fig.B1a) Definition of the direction of observation. b) The microstructure of the bulk Ni sample HPT deformed at room temperature to an equivalent shear strain εv_{HPT} of 32 observed in tangential direction.

To examine if the application of a different strain path can lead to a finer saturation grain size, the initial HPT deformed Ni samples were cold rolled to two different additive shear strains. Fig.B2a shows the microstructure of the sample which was additionally cold rolled to an equivalent shear strain ε_{CR} of 2.1 (State 1), resulting in a total equivalent shear strain ε of 34.1. Compared to the initial microstructure shown in Fig.B1b, the grains become aligned in the rolling direction and an elongation of the grains in the rolling direction is also clearly visible. Therefore, the thickness of the elongated grains becomes somewhat smaller compared to the initial state after HPT deformation due to the deformation. Nevertheless, the elongation is much less than expected from a simple elongation due to the rolling. The mean grain size measured by lineal intersection method is 205 nm in normal direction and 406 nm in rolling direction. Fig.B2b shows the microstructure of the cold rolled sample which experienced an additional equivalent shear strain ε_{CR} of 3.7 (State 2). Although the amount of the

additional applied equivalent shear strain ε_{CR} in State 2 is nearly two times more than in State 1, no significant difference in the microstructure between the two states is visible and the observed thickness reduction does not correlate with the applied reduction of the rolled sheets. It rather seems that after a certain amount of cold rolling the grain size reaches a saturation again and no further refinement of the microstructure takes place.

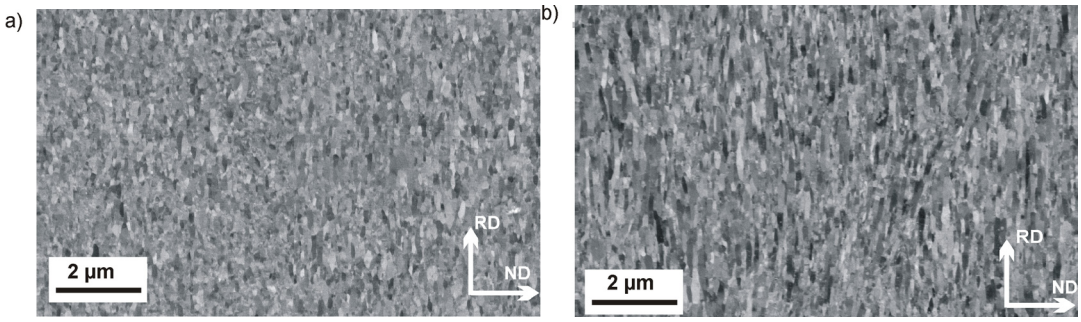

Fig.B2a) The microstructures of the bulk Ni sample which were additionally cold rolled after HPT deformation with 83% reduction and b) with 96% reduction. The rolling direction (RD) and normal direction (ND) during the cold rolling is depicted in the lower right corner.

Fig.B3a shows the inverse pole figure map of HPT deformed Ni at an equivalent shear strain εv_{HPT} of 32 which was obtained in radial direction. Each color corresponds according to the standard triangle to a specific crystallographic orientation. The pole figure in the [111] direction of the sample shows a torsion shear texture which is typical for HPT deformation [B8].
The inverse pole figure of the Ni sample which was additionally cold rolled with 83 % thickness reduction after the HPT deformation and the corresponding pole figure in the [111] direction are shown in Fig.B3b. Considerable differences between the texture of the HPT deformed Ni sample and the sample which was additionally cold rolled can be observed. After cold rolling, the texture is similar to one typically obtained by cold rolling of pure Ni [B15, B16].

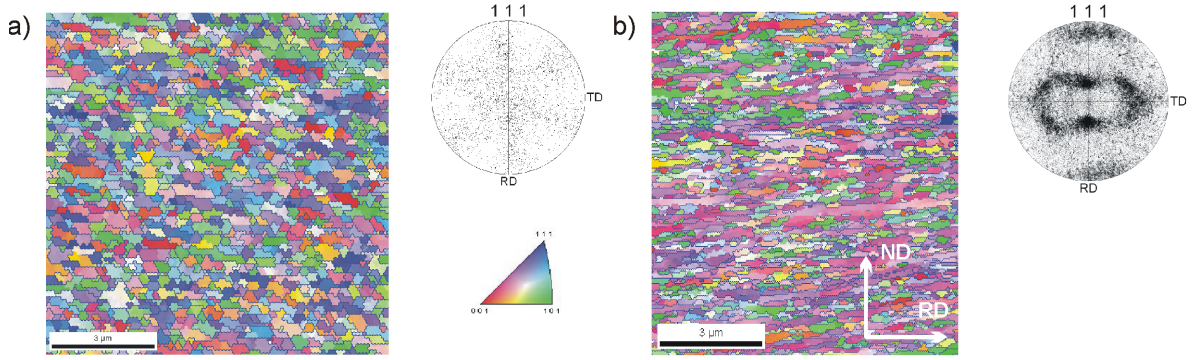

Fig.B3a) Electron back scattered diffraction (EBSD) map in the radial direction at a radius of about 6 mm (εv_{HPT} = 32) and the corresponding pole figure in the [111] direction. The standard triangle used for the EBSD maps is given in the lower right corner. b) EBSD map of HPT deformed Ni which was additionally cold rolled with 83 % reduction and the corresponding pole figure in the [111] direction. The rolling direction (RD) and normal direction (ND) during the cold rolling is depicted in the lower right corner of the micrographs.

Considering the aforementioned results the different strain path in the repeated rolling and folding process and HPT deformation can not solely be responsible for the significant finer saturation grain size in the rolling and folding process. In literature, different explanations for the occurrence of the saturation in the grain refinement during processing have been proposed. Besides grain boundary sliding or localized deformation, grain boundary migration is proposed to be the dominant process responsible for the limitation in the refinement by severe plastic deformation [B17]. If boundary migration limits the refinement during severe plastic deformation, introducing second phase or nano particles during processing should make it possible to stabilize finer microstructure.
Therefore, HPT consolidation and deformation of oxidized Ni powders were performed to introduce oxides in the latter bulk compacts. These oxides should act as barriers for boundary migration during the deformation process. To get a sufficiently thick oxide layer on the particle surface before the HPT consolidation, an annealing treatment was performed before the compaction. The annealing treatment was carried out in air at 400°C for 10 minutes. Afterwards the powder was precompacted directly in the HPT tool and subsequently deformed at room temperature.

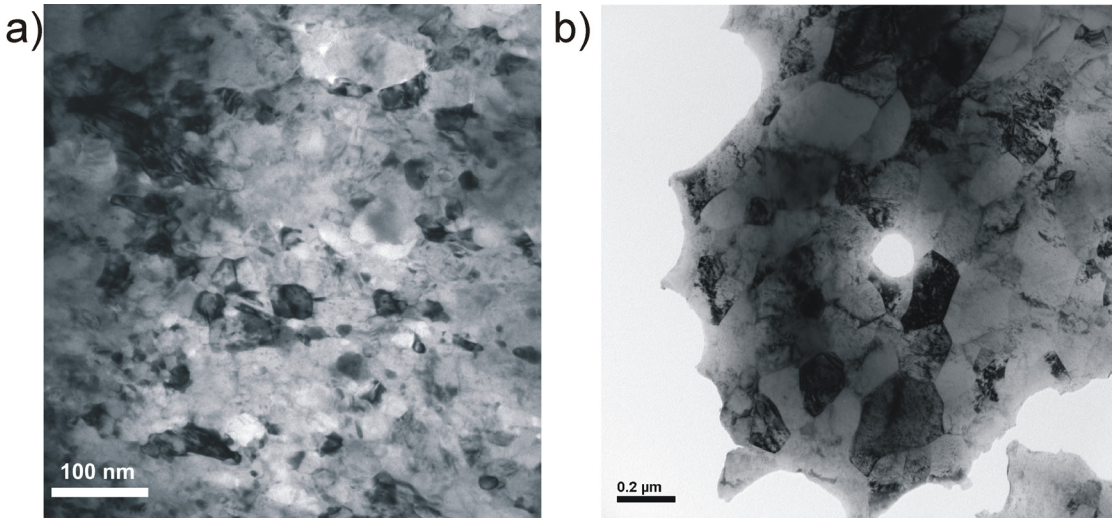

Fig.B4a) Bright-field transmission electron micrograph of the microstructure of the HPT consolidated sample of oxidized Ni powder [B18]. b) Bright-field transmission electron micrograph of the microstructure of the HPT deformed sample of bulk Ni. Please note the difference in magnification.

Fig.B4a shows a bright field TEM image of the resulting saturation microstructure of the HPT consolidated sample of oxidized Ni powder [B18]. Compared to the bright field TEM image of the saturation microstructure of the HPT bulk Ni sample shown in Fig.B4b, a significant smaller grain size can be seen. Indeed, a nanocrystalline structure is revealed. XRD measurements confirmed a two phase structure consisting of Ni and a small quantity of NiO in the HPT consolidated sample of oxidized Ni powder. Fig.B5a shows the XRD pattern of the HPT consolidated sample of oxidized Nickel powder. In Fig.B5b the size distributions of the coherently scattering domains of the Ni and NiO phase are shown. From the size distribution, the area weighted mean crystallite size $\langle x \rangle_{area}$ can be determined. The values for $\langle x \rangle_{area}$ are 31 nm and 9 nm for the Ni and NiO phase, respectively.

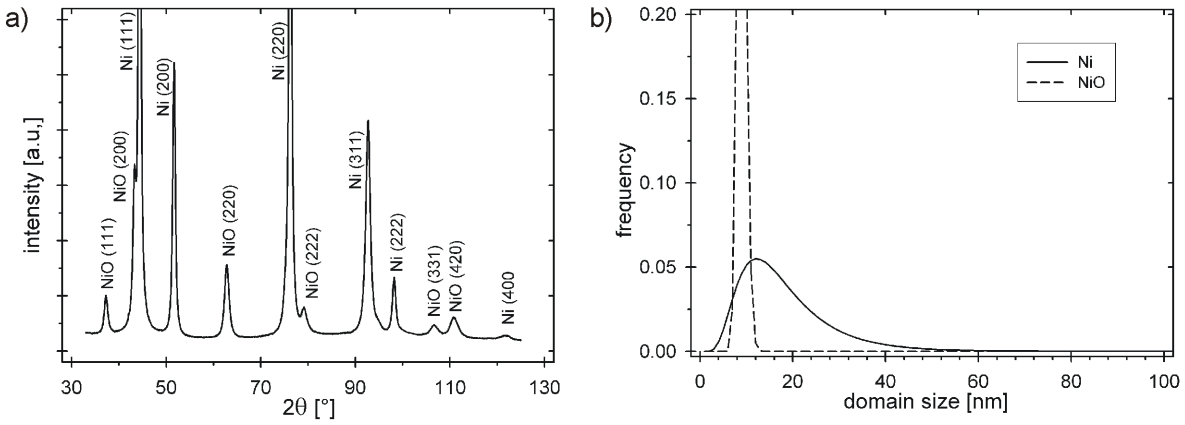

Fig.B5a) XRD pattern of HPT consolidated sample of oxidized Ni powder. b) Size distribution of the coherently scattering domains as determined by multiple X-ray Bragg profile analysis.

The differences, or comparing the initial HPT state and the cold rolled states, the similarities in the saturation microstructures are also reflected in the hardness values. Fig.B6a shows the evolution of the measured hardness values as a function of the applied equivalent shear strain in the HPT deformed bulk Ni and for the cold rolled samples. HPT deformation of bulk Ni leads to a hardness increase from 0.6 GPa in the undeformed state up to a hardness of 2.8 GPa in the saturation region. Additional cold rolling does not cause a significant further increase in the hardness. For the sample which was additionally cold rolled to an equivalent shear strain ε_{CR} of 2.1 (State 1), a hardness of 2.8 GPa was obtained. A hardness of 2.9 GPa was measured for the sample which was additionally cold rolled to an ε_{CR} of 3.7. Fig.B6b shows the evolution of the hardness as a function of the applied equivalent shear strain for the HPT consolidated samples of oxidized Ni powder. The HPT consolidated sample of oxidized Ni powder exhibits the highest hardness values (6.8 GPa) in the saturation region which is nearly 2.5 times the hardness of the HPT bulk Ni samples.

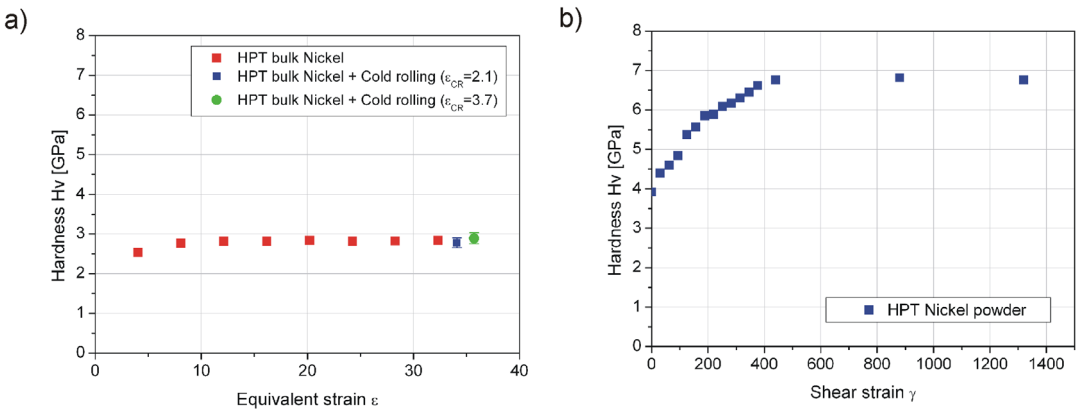

Fig.B6a) Microhardness of bulk HPT deformed Ni at room temperature as a function of the applied equivalent shear strain. The microhardness values of the Ni samples which were additionally cold rolled to two different strains are also shown. b) Microhardness of HPT consolidated oxidized Ni powder sample as a function of the applied equivalent shear strain.

These results emphasize the importance of the introduced oxides on the refinement of the microstructure. Besides the effect on the refinement and the hardness, the thermal stability of the microstructure could also be clearly improved as shown in [B18]. The same mechanism which impedes grain boundary migration during the deformation is also responsible for the improved thermal stability.

Conclusion

It could be shown that the large difference in the minimum size of the saturation microstructure after the different severe plastic deformation processes results not solely from the different applied strain paths. The dominant process which limits the grain refinement is the occurrence of grain boundary migration during severe plastic deformation. Therefore, to stabilize finer microstructures the movement of the grain boundaries must be hindered. In this work, it was possible to synthesize nanocrystalline bulk Ni using HPT deformation due to the pinning effect caused by the introduction of small oxide particles. These Ni oxide particles do not only lower the minimum achievable grain size, they also strengthen the matrix effectively and an excellent thermal structural stability is reached.

Acknowledgment

The financial support by the Austrian Fonds zur Förderung der wissenschaftlichen Forschung (Project number: S10402-N16) is gratefully acknowledged.

References for Publication B

[B1] A.P. Zhilyaev, S. Lee, G.V. Nurislamova, R.Z. Valiev, T.G. Langdon // Scripta Mater. 44 (2001) 2753-2758.

[B2] A.P. Zhilyaev, G.V. Nurislamova, B.K. Kim, M.D. Baró, J.A. Szpunar, T.G. Langdon // Acta Mater. 51 (2003) 753-765.

[B3] X. Huang, G. Winther, N. Hansen, T. Hebesberger, A. Vorhauer, R. Pippan, M. Zehetbauer // Mater. Sci. Forum 426-432 (2003) 2819-2824.

[B4] H. Zhang, X. Huang, R. Pippan, N. Hansen // in press Acta Mater.

[B5] R. Pippan, F. Wetscher, M. Hafok, A. Vorhauer, I. Sabirov // Adv. Eng. Mater. 11 (2006) 1046-1056.

[B6] T. Hebesberger, H.P. Stüwe, A. Vorhauer, F. Wetscher, R. Pippan // Acta Mater. 410-411 (2005) 281.

[B7] M. Hafok, R. Pippan // Philos. Mag. 88 (2008) 1857-1877.

[B8] M. Hafok, R. Pippan // Mater. Sci. Forum 550 (2007) 277-282.

[B9] B. Yang, H. Vehoff, H. Hohenwarter, M. Hafok, R. Pippan // Scripta Mater. 58 (2008) 790-793.

[B10] G.P. Dinda, H. Rösner, G. Wilde // Mater. Sci. Eng. A 410-411 (2005) 328-331.

[B11] G.P. Dinda, H. Rösner, G. Wilde // Scripta Mater. 52 (2005) 577-582.

[B12] A. Vorhauer, S. Kleber, R. Pippan // Mater. Sci. Eng. A 410–411 (2005) 281–284.

[B13] H.P. Stüwe // Adv. Eng. Mater. 5 (2003) 291-295.

[B14] E. Schafler, R. Pippan // Mater. Sci. Eng. A 387-389 (2004) 799-804.

[B15] R.R. Ray // Acta Metall. Mater. 43 (1995) 3863.

[B16] J. Pospiech, J. Jura, A. Mücklich, K. Pawlik, M. Betzl // Text. Microstruct. 6 (1983) 63-80.

[B17] R. Pippan, S. Scheriau, A. Taylor, M. Hafok, A. Hohenwarter, A. Bachmaier // accepted for publication in Annu. Rev. Mat. Res. (2010)

[B18] A. Bachmaier, A. Hohenwarter, R. Pippan // Scripta Mater. 61 (2009) 1016-1019.

Publication C: New procedure to generate stable nanocrystallites by severe plastic deformation

New procedure to generate stable nanocrystallites by severe plastic deformation

A. Bachmaier [a], A. Hohenwarter [a], R. Pippan [a, b]

[a] Erich Schmid Institute of Materials Science of the Austrian Academy of Sciences, Jahnstraße 12, A-8700 Leoben, Austria

[b] CD Laboratory of Local Analysis of Deformation and Fracture, Jahnstraße 12, A-8700 Leoben, Austria

Abstract

A new method to produce bulk nanocrystalline metal-matrix composites is presented. A metal powder is treated to obtain a relatively brittle layer with a defined thickness on the surface. The precompacted powder is deformed by High-Pressure Torsion until a dense bulk nanocrystalline material is formed. Due to fragmentation of the thin layer, it is possible to incorporate nanometer sized dispersions into the nanocrystalline metal-matrix. As example an oxidized nickel powder is investigated where thermal stability and microhardness are extraordinarily enhanced.

Keywords

High Pressure Torsion, Nanocomposite

Nanocrystalline materials have been a subject of extensive research over the past decades due to the effect of the nanocrystalline state on the microstructure and the mechanical, thermophysical, optical and magnetic properties of metals and alloys [C1-3]. Development of novel methods for large-scale processing of nanostructured materials is a challenging task. Methods of severe plastic deformation (SPD) are well known procedures to obtain dense ultra fine grained or even nanocrystalline bulk materials with unique properties, which cannot be obtained by nanostructured materials produced by other techniques [C4-9].

A large number of different SPD methods were developed in recent years [C10-13]. One of these SPD methods is High-Pressure Torsion (HPT), where the deformation is obtained mainly by simple shear. HPT is a simple technique to apply very large strains in a material due to the applied hydrostatic pressure during the deformation. It is ideal to investigate the limits in refinement which one can obtain in a material at a certain deformation temperature and strain rate [C14].

The evolution of the microstructure of single phase materials deformed by HPT shows a relatively uniform behaviour: With increasing strain the size of the structural elements continuously decreases until -at strains larger than a critical value - no further microstructural refinement can be observed. This general phenomenon in HPT is independent of the material and the processing parameters and has been observed in many pure metals and alloys [C7,C8,C14,C15]. Only the minimum size of the crystallites in the saturation and the necessary strain to reach this so called steady-state region are affected. The most important parameters influencing the refinement of the microstructure and the necessary strain to reach the onset point of saturation in single phase materials are the deformation temperature, alloying, the strain rate and the mode of deformation [C16]. In bulk microcrystalline (MC) nickel, a typical saturation microstructure with a mean grain size of ~200 nm after HPT deformation at room temperature can be obtained [C17,C18]. It is impossible to further decrease grain size by processing the samples to higher strains once the saturation region is reached. This limitation becomes even more clearly visible if HPT is applied to electrodeposited nanocrystalline (NC) nickel. Remarkable grain coarsening is induced during the HPT deformation and the material is transformed from the nanocrystalline microstructure into an ultrafine grained microstructure [C19]. Nevertheless the saturation size of the structural elements can be decreased distinctly with decreasing deformation temperature. HPT deformation of MC bulk nickel at -196°C leads to a saturation microstructure with a mean grain size of approximately 100 nm [C20]. Unfortunately, the microstructure of SPD pure metals in the as-deformed state is thermally unstable and annealing at low temperatures leads to recrystallization and coarsening of the microstructure, which in turn alters material properties. For this reason, one major goal for material development must be the enhancement of the thermal stability of the produced microstructure to make it suitable for technical applications.

Because the limit in the structural refinement during severe plastic deformation cannot be overcome with SPD of bulk single phase materials, we used a new processing route to circumvent these limitations. Nickel powders were consolidated via HPT to incorporate fine dispersed nickel oxide particles in the nickel matrix which were found to influence the obtainable saturation microstructure, mechanical properties and furthermore the thermal stability of the structure.

The HPT equipment used for processing the materials present in this paper is described in detail in [C8]. Two states of nickel powder were used in this study: (i) as-received nickel powder (99.8%, 70-

100 microns from Alfa Aesar®) and (ii) as-received nickel powder (99.9%, 3-7 microns from Alfa Aesar®) which was also additionally annealed before compaction. The powders were first precompacted in the HPT tool and subsequently deformed by HPT at room temperature. Both precompaction and the HPT deformation were carried out in air. The precompacted samples with a diameter of 8-14 mm and a thickness t of ~0.8 mm were deformed to different equivalent strains until the steady state, where no further refinement of the microstructure takes place. The pressure during deformation was varied between 2.5-6 GPa and the rotation speed was kept constant at 0.2 rpm.

After deformation, the deformed samples were additionally heat treated for 1 h at three different temperatures (243°C, 418°C and 591°C) corresponding to 0.3, 0.4 and 0.5 times of the melting temperature to investigate the thermal stability.

For comparison, experiments on microcrystalline bulk nickel were also performed. Microstructures were characterized in a scanning electron microscope type LEO 1525 using back scattered electrons and in a transmission electron microscope type Philips CM12. All microstructural investigations were performed at a distance of 1 mm from the HPT disc edge in all samples. Grain size distribution was measured using TEM bright-field images. Vickers microhardness measurements were performed on a BUEHLER Mircomet 5100 using a load of 1000 g. XRD measurements for phase analysis were performed with a Seifert 3000 PTS- X-ray diffraction system in a Θ/2Θ geometry using Cu-Kα radiation.

At first the behaviour during HPT deformation of nickel powders with a particle size of approximately 70-100 microns and nickel powder with a particle size of 3-7 microns in the as received condition is considered. Due to the large surface area especially in the latter case, a high amount of naturally formed oxide is introduced in the later bulk compacts. The powders were firstly precompacted directly in the HPT tool and subsequently HPT deformed. During the HPT deformation the powders are consolidated, the naturally formed oxides get fragmented and homogenously distributed and simultaneously the grain size is refined. The process of continuous subdivision of the initial grain structure in bulk metals is well documented in literature [C7,C16]. In contrast to bulk metals, larger strains must be applied for the HPT consolidation of powders to reach the saturation region. All here presented samples were HPT deformed until the saturation region was reached, in which no further refinement of the microstructure takes place. Grain sizes between 100-150 nm were estimated from the back scattered electrons (BSE) micrographs. However, also some grains with a size below 50 nm were observable. Nevertheless, no considerable influence of the different particle sizes of the nickel powders before deformation on the final microstructure was found.

These first experiments revealed that the fraction of naturally formed surface oxides in the as received powder is apparently too low to exhibit a distinct influence on the final microstructure. To increase the fraction of oxides, the initial powder was additionally annealed at 400°C for 10 minutes in air to obtain a thin oxide layer of on the surface of the particles [C21]. Figure C1 displays a schematic illustration of the nickel powder particles and the thin oxide layers on the surface of the particles after the annealing treatment. Afterwards, the oxidized nickel powder was again precompacted and subsequently HPT deformed until the saturation region was reached. BSE micrographs of the samples after HPT revealed a smaller saturation grain size compared to the non-oxidized nickel powder sample, which is clearly below 100 nm. During the deformation, the nickel powder particles are heavily deformed and

elongated whereas the grain size is refined at the same time (a schematic sketch of the process is shown in Figure C1).

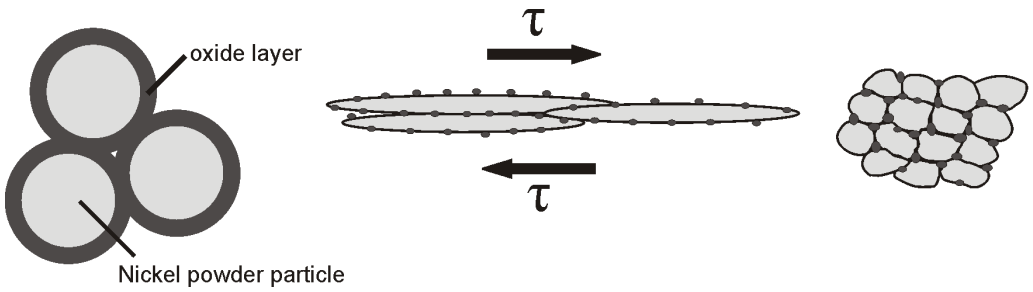

Figure C1: (a) Nickel oxide layers on nickel particles before deformation, (b) the fracture of these layers during deformation and (c) the assumed distribution of the nickel oxide particles in the nickel matrix after deformation.

The nickel oxide layers on the surface of the particles fracture during the deformation into small particles. Increase in deformation finally leads to a nanocrystalline nickel matrix with dispersed nickel oxide particles. At the moment, the distribution of the nickel oxide particles in the nickel matrix is not completely clear. Due to the nanometer size of the nickel grains we would rather expect the oxide particles to be dispersed along the grain boundaries and triple junctions of the grains. This assumption was further confirmed by transmission electron microscope (TEM) images, where no particles were visible inside the grains. The nickel oxide particles also have an influence on the structural evolution and final attainable microstructure of the samples: They should pin dislocations and grain boundaries, therefore deterring recovery and recrystallization during the deformation and therefore a finer microstructure is obtained.

Microhardness was measured from the center to the edge of the different HPT deformed samples (i.e. increasing applied strain). The results of the evolution of hardness as a function of the applied equivalent strain εv is plotted in Figure C2. All graphs show a similar trend: small hardness values at low equivalent strains, which increase with increasing applied equivalent strain and a saturation of hardness at large deformations which corresponds to the saturation in the grain size refinement. However, there exist distinct differences between the samples. The HPT induced grain size reduction in the beginning of the deformation leads to a strong hardening of the HPT deformed bulk nickel. The hardness increases from 0.6 GPa of the undeformed nickel sample up to a hardness of 2.8 GPa in the saturation region, which is reached at applied equivalent strains of about 20. Processing the sample to higher equivalent strains is not leading to a further increase in hardness as already mentioned. The same behaviour can be seen for the bulk nickel sample which was HPT deformed at -196°C. Nevertheless, the hardness in the saturation region is higher and reaches values of approximately 4.4 GPa. In this case, the increase in hardness results primarily from the reduction in grain size. The HPT bulk nickel sample deformed at room temperature exhibits a mean grain size of 200 nm, whereas the sample deformed at -196°C shows a mean grain size of approximately 100 nm. The evolution of hardness of the HPT consolidated samples of nickel powder is similar, but the necessary strain to reach saturation in hardness is much higher compared to HPT deformed bulk nickel. On the other hand, one should note that the obtainable hardness (5 GPa) of the HPT nickel powder samples is 1.7

times higher compared to that of HPT bulk nickel. The samples of the HPT consolidated oxidized nickel powder reach the highest hardness values (6.8 GPa) after an applied strain εv of about 250. The hardness is more than 10 times or 2.5 times higher compared to MC nickel or MC HPT deformed bulk nickel, respectively. The high hardness of these samples is primarily attributed to strengthening from further grain size refinement and maybe to the nickel oxide particles.

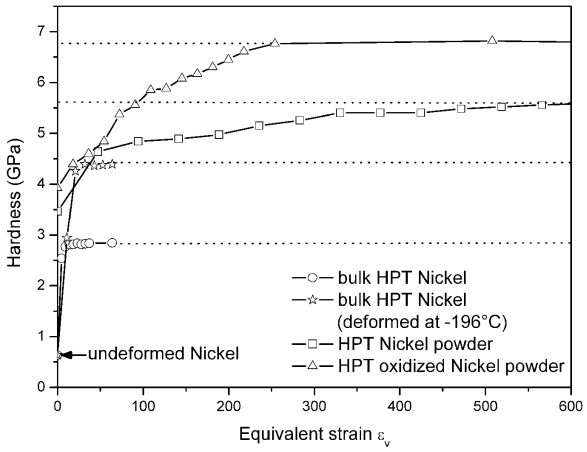

Figure C2: Microhardness of HPT bulk nickel deformed at room temperature and at -196°C and of HPT consolidated samples of nickel powder and oxidized nickel powder as a function of the applied equivalent strain. The hardness of bulk nickel without any deformation is 0.64 GPa (indicated by an arrow).

Transmission electron microscopy was used to investigate the microstructure of the HPT consolidated sample of oxidized nickel powder in more detail. The TEM sample was cut at a distance of 1 mm from the edge of the HPT disk. Figure C3 shows a bright field image of the microstructure of the sample after HPT, with insets showing the corresponding selected area electron diffraction (SAED) pattern and the grain size distribution. The bright field image reveals a nanocrystalline structure with few larger but as well very small grains, where the different grains can hardly be distinguished from each other. The grains have a rather broad grain size distribution making the estimation of the grain size difficult. The grain size distribution was measured using several TEM images. Most of the grains have a size between 10-30 nm, but there is also a considerable amount of grains with a size somewhat below 10 nm as well as few larger grains with grain sizes of ~30 to 100 nm. The mean size is 29.8 nm with a standard deviation of 20.6 nm. Furthermore, nickel oxide particles cannot be distinguished from nickel matrix grains.

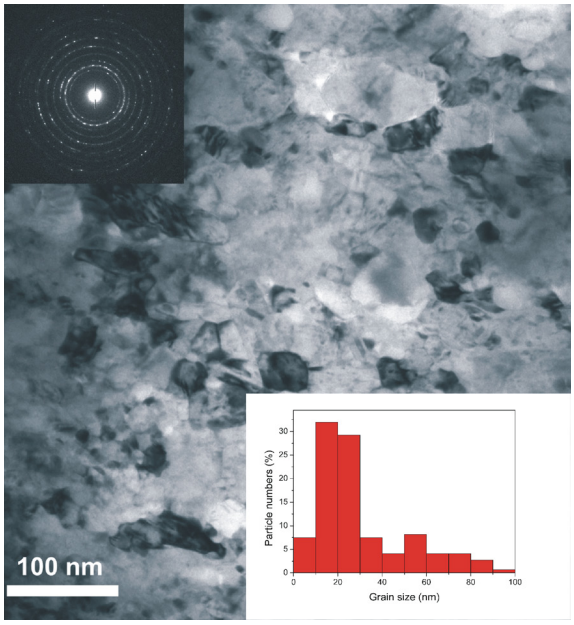

Figure C3: The bright-field transmission electron micrograph shows the microstructure of the HPT consolidated sample of oxidized nickel powder. The corresponding SAED pattern and the grain size distribution are shown as insets. The number fraction of grains vs. grain size of the HPT consolidated sample of oxidized nickel powder was measured by TEM bright field images.

In addition, the HPT consolidated samples of nickel powder and oxidized nickel powder were investigated by X-ray diffraction (XRD) in order to determine the phases present. The HPT consolidated sample of nickel powder exhibits only nickel peaks in the pattern. No other phases were detected. In contrast, the formation of an additional phase, namely nickel oxide, is clearly visible in the XRD pattern of the HPT consolidated sample of oxidized nickel.

In general, pure materials processed by SPD are thermally unstable due to the huge stored energy in form of crystalline defects like dislocations and “non-equilibrium” grain boundaries in the as-deformed state [C4]. A way to stabilize the fine, as-deformed microstructure is the presence of a high density of smallest uniformly distributed second phase particles. To study the thermal stability, the as-deformed HPT consolidated powder samples were annealed at three different temperatures for 1 h and changes in microhardness were subsequently measured (Figure C4). The HPT consolidated sample of nickel powder displays three distinguishable stages during the annealing treatment: the sample has an initial hardness of about 5 GPa, which stays nearly constant until 0.3 Tm (Tm being the melting temperature). The hardness rapidly drops at higher annealing temperatures between 0.3 – 0.4 Tm which might be due to grain growth. Further grain growth occurs at higher annealing temperatures leading to a further slight decrease in hardness reaching values of 1.7 GPa at 0.6 Tm. Microstructural observations by scanning electron microscopy confirmed these findings. The HPT consolidated sample of oxidized nickel powder shows higher initial hardness values of about 6.8 GPa which slowly decrease with higher annealing temperatures up to 0.4 Tm. In this temperature range recovery may take place, which is not affecting the grain size considerably as approved by scanning electron microscopy. At higher annealing temperatures (0.5 Tm) the hardness decreases somewhat faster reaching values still in the range of the initial hardness of the HPT consolidated sample of nickel

powder before the annealing treatment (4.8 GPa) or even larger than the hardness of the at -196°C HPT deformed bulk nickel. Marginal grain growth set in leading to an estimated grain size of approximately 100 nm. It is obvious that the fine dispersed oxides in the nickel matrix have a remarkable effect on the thermal stability: The HPT oxidized nickel powder samples exhibit an extended recovery stage, therefore the onset temperature for grain growth is increased and the structure remains nanocrystalline even at high annealing temperatures of 0.5 Tm with high hardness values of about 4.8 GPa. The fine microstructure is stabilized by the oxide particles because grain growth is impeded by uniform distributed particles due to their influence on dislocation motion and pinning of grain boundaries. The thermal stability is clearly improved compared to other results reported in literature on the thermal stability of HPT deformed MC bulk nickel considering also different purity and annealing treatment [C22,C23] and compared to the HPT bulk nickel samples deformed at -196°C where low annealing temperatures resulted in recrystallization and grain growth as well.

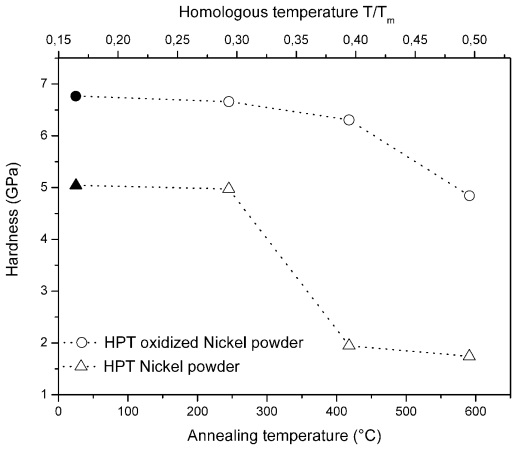

Figure C4: Evolution of the microhardness of the HPT consolidated samples of nickel powder and oxidized nickel powder as a function of the annealing temperature. The hardness of the as-deformed samples is also included (filled symbols).

To prove possible application of the process to other materials, experiments with oxidized aluminium powders were performed. The results showed that the method can be successfully applied to other powders as well. Oxidation of the initial metal powders is the easiest way to produce a metal matrix composite of type MO_x, whereby M and O stay for the metal and corresponding oxide, respectively. Another possible application might emerge from the initial carburization of metal particles to obtain metal matrix composites of type MC_x (C stays for carbon). By the use of coating processes almost arbitrary combinations of thin coatings and substrate metal might be achieved giving the opportunity to produce completely new types of metal matrix composites of type $M1M2X_y$ (X stays for the non-metallic component).

The new processing route proposed in this study offers an easy way to produce bulk nanocrystalline metal matrix composites with nanometer sized oxide dispersions without any complicated steps during the processing. Initial micrometer sized powders are oxidized via a simple annealing treatment and subsequently HPT consolidated until a fully dense bulk material is obtained. The oxidation of the initial powders has a huge impact on the final microstructure as well as on the mechanical properties and

the thermal stability of the consolidated material. A truly nanocrystalline metal matrix is produced which is stabilized with homogenously distributed nanometer sized oxide particles. The second phase particles strengthen the matrix effectively and an excellent structural stability is reached due to the pinning effect of the oxide particles. Additional advantages of the process are the use of micrometer sized powders instead of nanometer sized powders which are easier to handle and to produce as well as the avoidance of particle cluster formation during processing which are drawbacks in conventional powder consolidation techniques. The combination of a simple processing route, the possible application on arbitrary material combinations and the potential up-scaling of the process makes it an attractive candidate for further industrial application.

Acknowledgement

The financial support by the Austrian Fonds zur Förderung der wissenschaftlichen Forschung (Project number: S10402-N16) is gratefully acknowledged

References for Publication C

[C1] H. Gleiter, Prog. Mater. Sci. 33 (1989) 223-315.

[C2] H. Gleiter, Acta Mater. 48 (2000)1-29.

[C3] M.A Meyers, A. Mishra, D.J. Benson, Prog. Mater. Sci. 51(4) (2006) 427-556.

[C4] R.Z. Valiev, R.K. Islamgaliev, I.V. Alexandrov, Prog. Mater. Sci. 45 (2000) 103-189.

[C5] C.C. Koch, Rev. Adv. Mater. Sci. 5(2) (2003) 91-99.

[C6] A.P. Zhilyaev, T.G. Langdon, Prog. Mater. Sci. 53(6) (2008) 893-979.

[C7] T. Hebesberger, H.P. Stüwe, A. Vorhauer, F. Wetscher, R. Pippan, Acta Mater. 53 (2005) 393-402.

[C8] A. Vorhauer, S. Kleber, R. Pippan, Mater. Sci. Eng. A 410-411 (2005) 281-284.

[C9] J. May, H.W. Höppel, M. Göken, Mater. Sci. Forum 503-505(2006) 781-786.

[C10] R.Z. Valiev, A.V. Korznikov, R.R. Mulyukov, Mat. Sci. Eng. A 168(2) (1993) 141-148.

[C11] R.Z. Valiev, N.A. Krasilnikov, N.K. Tsenev, Mat. Sci. Eng. A 137 (C) (1991) 35-40.

[C12] A. Vorhauer, R. Pippan, Scripta Mater. 51(9) (2004) 921-925.

[C13] Y. Saito, H. Utsunomiya, N. Tsuji, T. Sakai, Acta Mater. 47(2) (1999) 579-583.

[C14] A. Vorhauer, R. Pippan, Mater. Sci. Forum 426-432(3) (2003) 2747-2752.

[C15] X. Huang et al., Mater. Sci. Forum 426-432(4) (2003) 2819-2824.

[C16] R. Pippan, F. Wetscher, M. Hafok, A. Vorhauer, I. Sabirov, Adv. Eng. Mater. 8(11) (2006) 1046-1056.

[C17] H.W. Zhang, X. Huang, N. Hansen, Acta Mater. 56(19) (2008) 5451-5465.

[C18] M. Hafok, R. Pippan, Mater. Sci. Forum 550 (2007) 277-282.

[C19] B. Yang, H. Vehoff, A. Hohenwarter, M. Hafok, R. Pippan, Scripta Mater. 58(9) (2008) 790-793.

[C20] A. Hohenwarter, thesis, University of Leoben (2006).

[C21] A.M. López-Beltrán, A. Mendoza-Galván, Thin solid films 503 (2006) 40-44.

[C22] R.K. Islamgaliev, F. Chmelik, R. Kuzel, Mater. Sci. Eng. A 237 (1997) 43-52.

[C23] E. Schafler, R. Pippan, Mater. Sci. Eng. A 387-389 (2004)799-804.

Publication D: Effect of oxide particles on the stabilization and final microstructure in aluminium

Effect of oxide particles on the stabilization and final microstructures in aluminium

Andrea Bachmaier and Reinhard Pippan

Erich Schmid Institute of Materials Science of the Austrian Academy of Sciences, Jahnstrasse 12, 8700 Leoben, Austria

Abstract

Bulk aluminium samples containing alumina particles have been produced by different severe plastic deformation methods. Aluminium foils with different initial foil thicknesses were cold rolled to different amounts of strain and aluminium powders were consolidated and deformed by High Pressure Torsion (HPT). During processing, alumina particles from the foil or particle surface are easily incorporated and dispersed in the bulk material. The influence of these alumina particles on the developing microstructures and the mechanical properties has been studied.

Keywords

High pressure torsion, aluminium, alumina particles

Introduction

The mechanical and physical properties of materials are defined by structural features. A significant role plays the grain size of a material as the strength of a material increases with decreasing grain size which led to an increasing interest in producing materials with extremely small grain sizes [1]. Synthesis techniques are divided into “top-down” and “bottom-up” techniques as severe plastic deformation for the former one and such as inert gas condensation, electrodeposition, and ball milling with subsequent consolidation for the latter. Advantages of the top-down processes are that materials with theoretical density can be prepared, larger quantities of a material can be produced and contamination during the processing can be avoided.

Severe plastic deformation techniques include methods like equal channel angular pressing, HPT, multi-axial forging, constrained groove pressing and accumulative roll-bonding [D1]. It has been shown that ultrafine grained and sometimes nanocrystalline materials can be obtained by severe plastic deformation of different metals and alloys, whereas the focus was mainly on the processing, microstructure and mechanical properties at equivalent strains of 1-10 [D2-4]. At higher strains, a so called steady state is reached and no further refinement of the microstructure is possible [D5]. The dominant process limiting the grain refinement is the occurrence of grain boundary migration during severe plastic deformation [5-8]. Therefore, all mechanisms reducing the mobility of grain boundaries are efficient to further decrease the grain size. This was shown for example in [D6], where nanocrystalline nickel stabilized with homogeneously distributed nanometer-sized oxide particles was produced by HPT.

In a recent published study, the role of oxide particles on the development of deformation structures in pure aluminium containing a fine dispersion of oxides and of aluminium foil processed by rolling were investigated [D9,D10]. Consistently with our results for nickel, it was found that a finer scaled microstructure developed if the material contained oxides. The question arises how long these oxide particles are able to act as a barrier for grain boundary migration during processing. The present paper is devoted to this subject. Aluminium powders containing two different amounts of oxide particles are HPT deformed and the developing microstructure is compared to HPT deformed bulk aluminium. To prove the insignificance of the way how the strain is applied, layers of aluminium foil with different initial foil thicknesses were cold rolled to different amounts of strain and the role of the oxides on hindering grain boundary motion is studied. Furthermore, the thermal stability of the HPT deformed aluminium powder samples is investigated.

Experimental

In this study, aluminium of different initial conditions (powder, foil and bulk material) was processed by different severe plastic deformation methods.

Two different aluminium powders were used as starting material for HPT consolidation and subsequent deformation: aluminium powder (-325 mesh, 99.5% purity) was obtained from AlfaAesar®.

The as-received aluminium powder has a mean particle size of 90 µm as measured from a series of scanning electron microscopy (SEM) images. A second aluminium powder was obtained from eckagranules® which has a mean particle size of 1.3 µm. Both aluminium powders were directly precompacted in our HPT tool without any special powder treatment or handling before the compaction. The powders were compacted to small disks with a diameter of ~ 8 mm and a thickness t of ~ 0.8 mm with a pressure of ~ 0.5 GPa. Afterwards, the precompacted samples were HPT deformed at room temperature for 25 rotations applying 4 GPa pressure. The rotation speed was kept constant at 0.2 rpm for all deformed samples. Further details of the HPT facility itself and the HPT deformation process are given in [D4,D5].

From a bulk aluminium (99.99% purity) rod, samples with a diameter of 8 mm and a thickness of 0.8 mm were cut. HPT deformation was conducted at room temperature for 3 turns with a pressure of 2 GPa.

Commercially available aluminium foil coils with an initial individual foil thickness ti of ~ 10-11 µm resulting in ~ 1500 layers of aluminium foil in one single coil were deformed by rolling in a single standard cold rolling mill without lubrication. The coils were cold rolled in one single pass to 50% thickness reduction to achieve adequate bonding. The gap was adjusted prior to rolling to give the designated reduction in thickness. Further cold rolling in several passes resulted in final thickness reductions of 78%, 90%, and 99%.

Aluminium foil (99.0% purity) with an initial thickness ti of ~ 750 nm and a variation in thickness of ± 30% was obtained from Advent Research Materials. Stacks of ~ 600 layers (dimension of the sheets ~ 2 x 2 cm) of this submicron foil were cold rolled to estimated 75% and 85% thickness reductions in one single pass. Stacks of ~1220 layers (dimensions of the sheets ~ 2 x 2 cm) of this foil were cold rolled in one single pass to estimated 90% thickness reduction and in one additional pass to an even higher thickness reduction (~95%). All stacks of the submicron aluminium foil were additionally enclosed in 2-4 layers of aluminium foil with a thickness of 10-11 µm to increase the complete starting thickness of the stacks. Due to the variation in thickness of ± 30% and the additional outer thicker aluminium foils, the effective applied true strain can only be estimated.

All deformed samples were examined by SEM in a SEM type LEO 1525. In the case of the HPT deformed aluminium samples, the disks were cut in the middle and the micrographs were taken at radii of approximately 3 mm on the shear plane of the sample. All micrographs of the cold rolled aluminium foils were taken on the normal direction (ND) -rolling direction (RD) planes. Additionally, rectangles (dimensions ~ 10 x 10 µm) were milled on the ND-RD planes of the aluminium foil samples with an initial thickness of 750 nm cold rolled to the two highest thickness reductions (~90 and 95%) using a Focused ion beam (FIB) workstation (LEO XB 1540) by the impact of Ga+ ions. To keep the FIB damage small the sample was cut perpendicular to the RD direction. The microstructure on these rectangles was examined by SEM right after FIB milling.

Grain sizes were measured from the SEM micrographs. About six or more representative BSE micrographs were chosen for the different aluminium powder samples and the aluminium foil samples with an initial foil thickness of 11 µm for all rolling conditions. The grains in each of the micrographs were traced by hand and the equivalent circle diameter (ECD) was defined from each material and condition. In the case of the aluminium foil samples with an initial foil thickness of 750 nm, the

boundary spacing of the foils after the different degrees of rolling except for the aluminium foil with the highest reduction in thickness (~95%) were measured with the line intersection method from representative SEM micrographs.

Vickers microhardness measurements along the radii on the shear plane of the HPT deformed aluminium samples were performed on a BUEHLER Mircomet 5100 using a load of 200 g. Vickers microhardness tests using the same load as for the HPT deformed aluminium samples were performed on the RD-ND planes for the cold rolled aluminium foil samples with an initial thickness of 11 µm. For the aluminium foil samples with an initial thickness of 750 nm, Vickers microhardness tests using the minimum load of 10 g were performed on the RD-ND planes to avoid delamination of the aluminium foils. The mean values of 50 separated Vickers hardness measurements across the RD-ND planes for all aluminium foil samples are reported. However, it was not possible to evaluate the microhardness of the aluminium foil with higher thickness reductions with the Vickers microhardness test due to delamination of the individual foils. Therefore, indentations on the aluminium foil with approximately 90% thickness reductions were performed with a Hysitron TriboScope fitted with a Berkovich Indenter. 50 indentations measurements across the RD-ND planes were produced with a load of 2500 µN. For the purpose of comparison, indentations with the same alignments as mentioned before were additionally performed on the HPT deformed aluminium powder samples. On the sample with the highest amount of thickness reduction (~95%), 19 indentations with a load of 2500 µN were performed on the previously FIB milled rectangles.

The HPT deformed aluminium powder samples were additionally annealed in air for 1 h at 115 - 470 C to investigate the thermal stability of the deformed material.

Results

3.1 Microstructure and microhardness of HPT deformed aluminium

HPT deformation of bulk aluminium and the HPT consolidation and deformation of the aluminium powders with the different initial particle sizes were performed until the saturation region was reached, meaning that no further grain refinement takes place [D5]. Representative microstructures of the HPT deformed bulk aluminium sample and the HPT deformed aluminium powder sample with an initial particle size of about 90 µm can be seen Fig.D1. Comparing both saturation microstructures, a huge difference in the final grain size is revealed. The average grain size of the HPT deformed bulk aluminium sample is ~1 µm (Fig.D1a). Compared to the bulk aluminium sample, the saturation microstructure of the HPT deformed powder aluminium sample has a significantly smaller grain size (Fig.D1b). The grain sizes were evaluated using several BSE micrographs: The mean grain size (ECD) was determined to be 145 nm for the Aluminium powder with the initial particle size of ~90 µm and 104 nm for the Aluminium powder with the initial particle size of ~1.3 µm. This means, the final microstructure of the aluminium powder samples consists of grains only about one tenth of the size of the HPT deformed bulk aluminium sample.

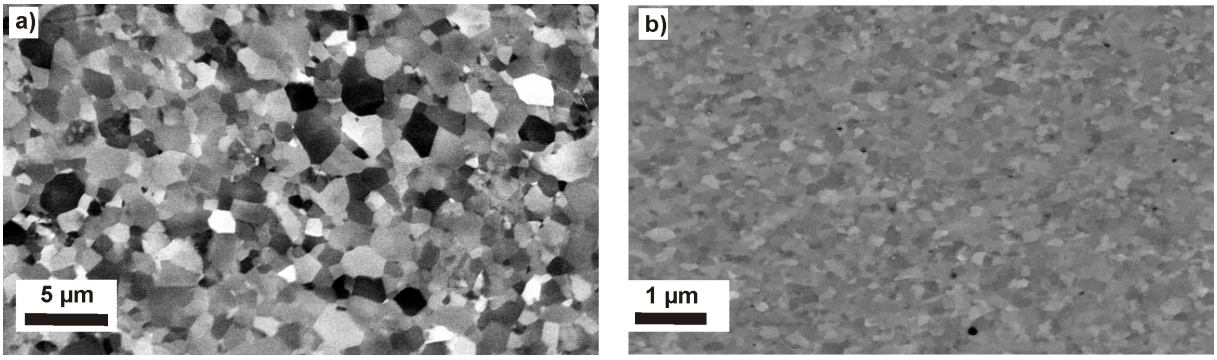

Fig.D1: a) BSE micrograph of the saturation microstructure of a HPT bulk alumnium sample deformed at room temperature. b) BSE micrograph of the saturation microstructure of a HPT consolidated and deformed alumnium powder sample with an initial aluminium particle size of about 90 µm.

The large difference in the final microstructure of the different HPT deformed samples is also clearly visible in the measured microhardness values: The HPT bulk aluminium sample shows a nearly constant hardness along the radius with an average hardness of ~0.25 GPa (see Fig.D2). In the case of the aluminium powder samples the hardness values along the radius are considerably higher. The aluminium powder sample with the initial coarser particle size (90 µm) shows an average hardness of ~0.88 GPa which is more than 3 times the hardness of the HPT aluminium bulk sample. An even higher hardness is reached in the sample consolidated from the powder with the finer initial particle size (1.3 µm). With an average value of ~1.30 GPa, the hardness is more than 5 times higher than that of the HPT bulk aluminium.

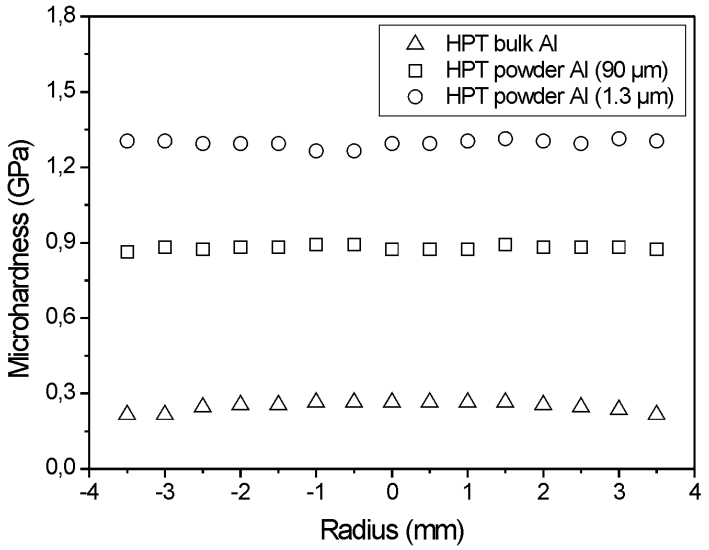

Fig.D2 Microhardness of HPT consolidated samples of aluminum powder with an initial particle size of 1.3 µm and 90 µm and HPT bulk alumnium sample deformed at room temperature.

Microhardness was measured from the center to the edge of the different HPT-deformed samples which implies that the applied strain increases from the center to the edge of the sample. Therefore, also the hardness should increase with increasing applied strain as well as the grain size constantly decreases. Nevertheless, there is a reasonable homogeneity in the hardness values across the center

to the edge of the samples. If a high enough amount of strain is applied, a saturation region is reached where no further increase in hardness or decrease in grain size is observed. Due to the high amount of applied strain (25 revolutions), even at regions in approximate vicinity of the center this saturation region was easily reached.

3.2. Thermal stability of the HPT deformed samples

The HPT consolidated and deformed aluminium powder samples were additionally annealed for 1h in air at temperatures up to about 0.8 Tm (Tm being the melting temperature) to evaluate the influence of subsequent annealing on the microhardness and microstructure. The annealing behaviour was investigated using microhardness testing after the annealing treatment. In Fig.D3, the measured microhardness as a function of the annealing temperature is plotted. For the HPT aluminium powder sample with the initial particle size of 90 µm, the hardness remains unchanged up to annealing temperatures of 0.60 Tm (290°C). At annealing temperatures of 0.77 Tm (450°C), a pronounced drop in the hardness is observable and a value of 0.73 GPa is measured. This drop in the hardness is connected to the beginning of grain growth which is confirmed by microstructural observations with the SEM. Until annealing temperatures of ~0.50 Tm (200°C), the hardness of the HPT aluminium sample with an initial particle size of 1.3 µm stays constant at a value of 1.3 GPa. At higher annealing temperatures the microhardness decreases constantly reaching values of 0.67 GPa at the highest annealing temperature of 0.8 Tm (470°C). In the beginning, the hardness decrease is due to recovery not affecting the grain size whereas at higher annealing temperatures grain growth occurs as well as approved by SEM.

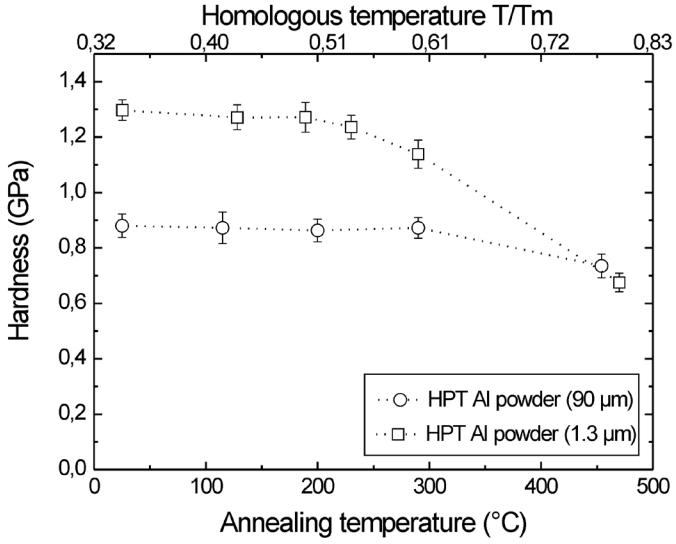

Fig.D3 Microhardness as a function of the annealing temperature for the HPT consolidated sample of alumnium powder with an initial particle size of 1.3 µm and 90 µm.

3.3. Microstructure and microhardness of the cold rolled aluminium foils

Stacks of aluminium foil with an initial foil thickness of ~11 µm were cold rolled in one single pass to 50% thickness reduction. This high amount of thickness reduction in the beginning was necessary to

achieve sufficient bonding between the individual layers of the aluminium foil to enable further rolling. Several further passes resulted in overall thickness reductions of 78%, 90% and 99%.

Thickness reduction	ECD (µm)	Boundary spacing (µm)	Microhardness (GPa)
50%	1.08	~5.1	0.35
78%	0.75	~2.4	0.41
90%	0.65	~1.1	0.43
99%	0.47	-	0.47

Table D1: Applied thickness reduction, equivalent circle diameter (ECD), boundary spacing and microhardness for the aluminium foil with an initial thickness of 11 µm.

The data in Table 1 summarizes the ECD values, the original foil boundary spacing and microhardness values measured for the aluminium foils with the different thickness reductions. With increasing amount of strain, the distance between the original boundaries is reduced. As well as the thickness of the foils is decreasing, the grain size is reduced from 1.08 µm at 50% thickness reduction to 0.47 µm at 99% thickness reduction. The distance between the original boundaries decreases from about 5.1 µm at 50% thickness reduction to about 1.1 µm at 90% thickness reduction. At thickness reductions of 99%, the original foil boundaries are no longer visible. Microhardness increased from 0.35 GPa for the sample cold rolled to 50% thickness reduction to 0.47 GPa for the sample cold rolled to 99% thickness reduction. In Fig.D4, the resulting microstructures of the aluminium foil cold rolled to 90% and 99% thickness reduction can be seen. The wavy structures sometimes visible in Fig.D4 are artefacts from the electro-polishing treatment. Fig.D4a shows a BSE micrograph of the aluminium foil with 90% thickness reduction. The original boundaries between the individual aluminium foils are still visible and most of the grains are located between these boundaries. The grains seem to be a bit aligned in rolling direction. Due to the natural alumina layer which forms on the surface of the individual aluminium foils, alumina particles are incorporated in the aluminium matrix. The position of the original foil boundaries and the alumina particles can be more clearly seen in Fig.D4b, which shows a micrograph taken with the Inlens detector from almost the same area as in Fig.D4a. The alumina particles are aligned in the rolling direction emphasizing the original positions of the foil boundaries. The alumina particles influence the position of the boundaries. It seems that nearly no alumina particles are located between the original foil boundaries. The boundary spacing is also somewhat variable as the original foils are not perfectly straightened.

In Fig.D4c and Fig.D4d, BSE and In-lens micrographs of the aluminium foil cold rolled to 99% thickness reduction recorded at the same area can be seen. In contrast to the former microstructure, the original foil boundaries are no longer visible. Besides, the grains seem to be more equiaxed and hardly any alumina particles can be seen compared to the microstructure in Fig.D4a and D4b. Furthermore, the few still visible alumina particles seem to be located more inside the grains than on the grain boundary. One possible reason for the diminished number of visible alumina particles might be due to different etching times during sample preparation in the case of the aluminium foil samples cold rolled to 90 and 99% thickness reduction. Depending on the etching time and location of the alumina particles, there are apparently more or less alumina particles visible.

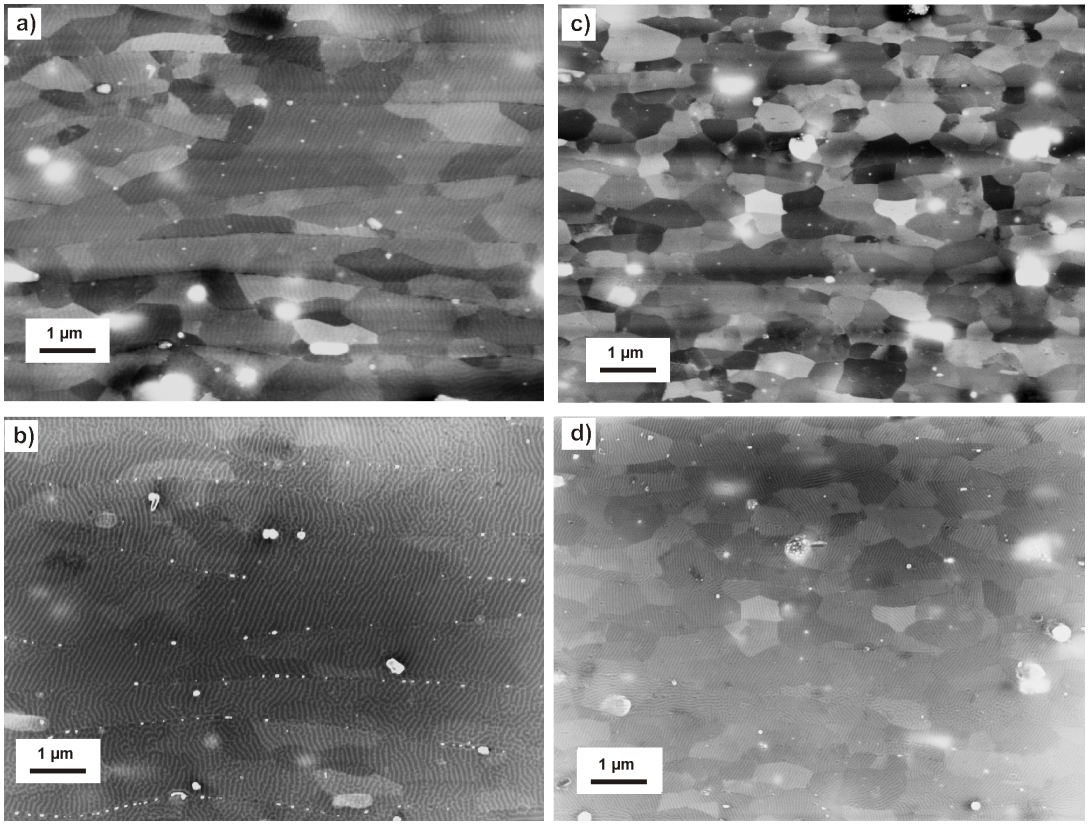

Fig.D4 BSE micrographs of the final microstructure of the cold rolled alumnium foils with an initial thickness of about 11 µm: a) alumnium foil cold rolled to 90% thickness reduction and c) alumnium foil cold rolled to 99% thickness reduction. SEM micrographs recorded with the Inlens detector: b) alumnium foil cold rolled to 90% thickness reduction and d) alumnium foil cold rolled to 99% thickness reduction.

Stacks of aluminium foil with an initial thickness of approximately 750 nm were cold rolled in one single pass to 4 different thickness reductions (approximately 75% to 95%). Table 2 summarizes the rolling conditions, resulting final foil spacing and microhardness of the cold rolled foils. Unfortunately it was not possible to prepare the samples metallographically adequate to record good SEM micrographs were the individual grains are visible. Nevertheless, it was possible to resolve the individual foils. The resulting foil spacing of each rolled condition was measured from several SEM micrographs using the line intersection method. The foil spacing decreases from 170 nm for the aluminium foil rolled to 75% thickness reduction to 107 nm in the case of the foil rolled to 90% thickness reduction.

Thickness reduction	Foil spacing (µm)	Microhardness (GPa)
~75%	0.174	0.62
~85%	0.130	0.71
~90%	0.107	1.44*
~95%	<0.1, ~0.05	3.57*

* measured with nanoindentation

Table D2: Measured foil spacing and microhardness for the aluminium foil with an initial foil thickness of 750 nm.

The SEM micrograph recorded at the previously FIB milled rectangle of the aluminium foil sample cold rolled to ~90% thickness reduction can be seen in Fig.D5a. Even though only the final thickness of the foils can be seen from the SEM micrographs, one can assume that the maximum possible grain size in the foils is limited by the foil thickness. Therefore, the maximum possible grain size in the foil with 90% thickness reduction is about 107 nm. In Fig.D5b, the microstructure of the aluminium foil sample cold rolled to the highest thickness reduction can be seen. From the micrograph, final foil thicknesses definitely below 100 nm can be observed and the mean foil spacing is estimated to be around 50 nm. It can be assumed that the maximum possible grain size in this foil is limited by the foil thickness as well.

The hardness of the aluminium foils with an initial thickness of 750 nm increased from 0.62 GPa for the aluminium foil with the smallest amount of thickness reduction to about 3.57 GPa for the aluminium foil with the highest amount of thickness reduction.

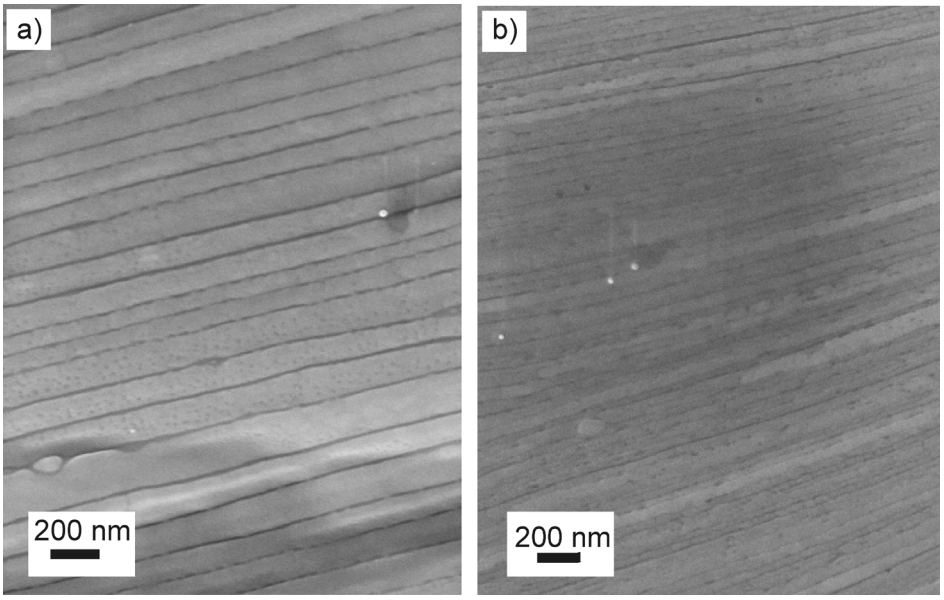

Fig.D5: a) SEM micrographs of the final microstructure of the aluminium foil with an initial thickness of ~ 750 nm cold rolled to approximately 90% thickness reduction. b) SEM micrograph of the final microstructure of the aluminium foil with an initial thickness of~ 750 nm cold rolled to approximately 95% thickness reduction.

Discussion

4.1 Effect of alumina particles on microstructure and thermal stability

On the surface of the aluminium powders, initially an amorphous oxide film is formed which has a thickness somewhat below 4 nm at room temperature without any oxidation treatment [D11,D12]. Since no additional heat treatment was performed on our aluminium powders, we assume that on the surface of the powders an amorphous alumina film with a thickness of about 4 nm is formed. Based on the fact of different amount of surface area for different initial particle sizes, the fraction of alumina is distinctly higher for the aluminium powder with the smaller initial particle size.

During HPT consolidation and deformation, the powder particles undergo severe plastic deformation, they become elongated and the alumina layer fractures into small particles. These particles are distributed through the aluminium matrix as simultaneously the grain size is refined. The alumina particles have an influence on the structural evolution and final attainable grain size of the aluminium samples. Whereas in the HPT deformed bulk aluminium sample a saturation grain size of ~1 µm is obtained, the saturation grain size in the HPT deformed aluminium powder samples is ~ 100-150 nm depending on the initial particle size. We assume that a process similar to dynamic recrystallization limits the refinement during SPD [D5,D7]. Due to the pinning effect of the alumina particles on grain boundaries, therefore deterring recovery and recrystallization during the deformation, a significantly finer microstructure is obtained compared to bulk HPT deformed aluminium.

The thermal stability of a material is of great importance. Both samples exhibit inherent grain size stability up to reasonably high temperatures for pure aluminium or even aluminium alloys [D13]. The hardness of both materials is stable up to an annealing temperature of ~200°C. Recrystallization or grain growth is delayed because the finely dispersed alumina particles pin grain boundaries. Therefore, the thermal stability of the material can be considerably enhanced by these particles.

On the surface of aluminium foils an amorphous alumina film forms immediately as well [D14]. Taking stacks of aluminium foils and rolling these stacks to produce an aluminium bulk sample gives the possibility to examine the effects of the alumina particles on the latter bulk sample. During the rolling process, the brittle alumina film fractures and is fragmented, whereas the aluminium is able to deform plastically. Assuming that the alumina particles formed are distributed through the aluminium by this rolling process, their influence on the microstructure and mechanical properties are easily analyzed. Taking aluminium foils with an initial foil thickness of approximately 10 µm, the original grains can not exceed a size of 10 µm. Rolling these foils to 90% thickness reduction should lead to foil thicknesses of approximately 1 µm with grains not exceeding 1 µm. Even smaller grain sizes should be possible, if the same foils are rolled to even higher thickness reductions.

The alumina particles were observed to be located on the original boundaries of the aluminium foils cold rolled to 50%, 78% and 90% thickness reduction. Only at the highest strain in this study (99% thickness reduction), nearly no aligned alumina particles can be seen any more. It seems that with increasing strain, the pinning effect of the alumina particles reaches saturation. With increasing strain, the length of boundaries in the material increases by elongation of the grains or by the formation of new boundaries. On the contrary, the number of the alumina particles remains constant. At a certain amount of strain, the number of alumina particles gets insufficient to pin the boundaries effectively and the boundaries are able to disassociate themselves from the alumina particles more effectively

Compared to pure aluminium processed by accumulative roll bonding to similar strains equivalent microstructures could be reached in our cold rolled foils [D15,D16]. It is hardly surprising because the roll bonding process of the aluminium foils is similar to the accumulative roll bonding process.

The pinning and stabilization effect by the oxide particles at the grain boundary to the reduced foil thickness remains until a thickness reduction of ~90-95% for both aluminium foils independent from their initial foil thickness of 11 µm or 750 nm. The same effect is also observed for the HPT consolidated and deformed aluminium powder samples, where the grain size compared to HPT bulk deformed aluminium could be reduced and stabilized by a factor of ten.

4.2 Effect of alumina particles on strength

In Fig.D6, the hardness as a function of the structural size of the different aluminium samples is plotted. Structural size stands for the measured mean equivalent circle diameter in the case of the HPT deformed aluminium powder samples and the aluminium foil samples with an initial foil thickness of about 11 µm. For the aluminium foil samples with an initial foil thickness of 750 nm, structural size denotes the spacing between the individual foils measured with the line intersection method. In case of the aluminium foil sample with an initial foil thickness of 750 nm cold rolled to the highest thickness reduction (~95%), the spacing between the individual foils could not be measured due to the small spacing distance and the mean foil thickness is estimated to be about 50 nm (compare SEM image of the microstructure in Fig.D5b).

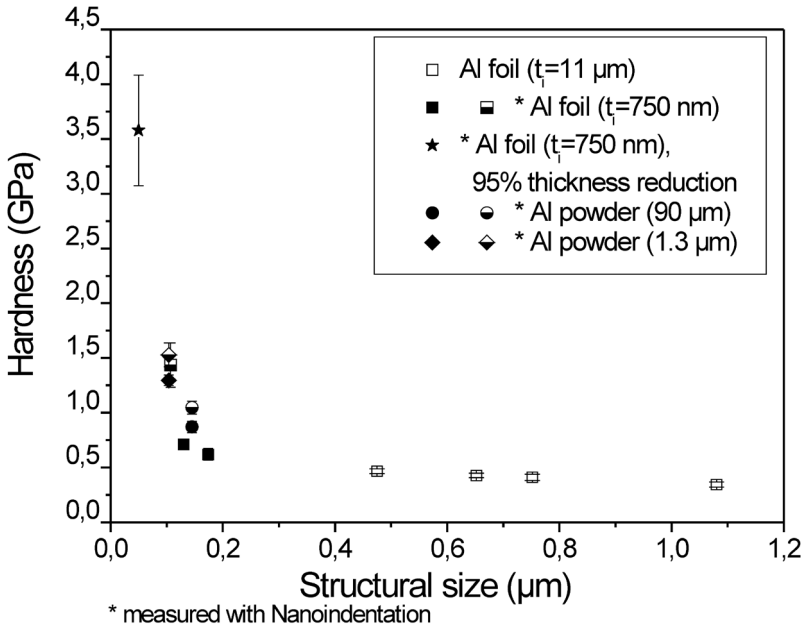

Fig.D6 Microhardness as a function of structural size plotted for the alumnium foils with an initial thickness ti of 11 µm cold rolled to 50%, 78%, 90% and 99% thickness reduction, the alumnium foil with an ti of 750 nm cold rolled to approximately 75%, 85%, 90% and 95% thickness reduction and for the HPT consolidated samples of aluminium powder with an initial particle size of 1.3 µm and 90 µm, respectively.

In the beginning, the hardness of the samples continuously increases with decreasing structural size. As the structural size gets smaller, a deviation from the continuous hardness increase is observed and the hardness distinctly increases faster. Due to the fact that the hardness of the aluminium foil samples with an initial foil thickness of 750 nm cold rolled to ~90% and 95% thickness reduction could only be evaluated with nanoindentation, the hardness of both HPT deformed aluminium powder samples were measured with the Vickers microhardness test as well as with nanoindentation for the purpose of comparison. The measured hardness values with the nanoindentation method are slightly higher for both HPT deformed aluminium powder samples compared to the values measured with the Vickers microhardness test (see Fig.D6). Although the hardness measured with nanoindentation

cannot be absolutely compared with the Vickers microhardness test results, the general trend towards a deviation of the linear hardness increase with decreasing structural size is definitely determinable.
The well known Hall-Petch relationship

$$\sigma_y = \sigma_0 + k_y d^{-1/2}, \quad (1)$$

where σ_0 and ky are material specific parameters, correlates the yield strength of a material with the size of the grains [D17,D18]. To estimate the fraction of strength enhancement due to grain size, the obtained data is analysed in terms of this relation. In Fig.D7a, the calculated yield stress σy is plotted as a function of the inverse square root of the structural size and as a function of the inverse structural size of the different aluminium samples in Fig.D7b. The yield stress is calculated from the measured hardness values by the Tabor relation given in Equation 2 [D19]:

$$H_v = 3 \cdot \sigma_y \quad (2).$$

For structural sizes above ~150 nm, classical Hall-Petch behaviour is observed (Fig.D7a). Experimental values of 62 MPa and 0.06 for σ_0 and ky were found, respectively. Compared to data from literature for σ_0 and ky, the determined values for the aluminium samples in this study are slightly higher [D20]. The values from the literature were determined for coarse grained recrystallized aluminium. Therefore, increased σ_0 and ky values result from deformation induced structures. Not only the structural size contributes to the increased hardness but high dislocation densities and high internal stresses contribute to the hardness as well. A small contribution of oxide dispersion strengthening due the presence of alumina particles is also expected but the amount of Al_2O_3 is rather low [D9,D21-23]. A deviation from the classical Hall-Petch behaviour is observed for smaller structural sizes: at structural sizes below ~ 150 nm, the Hall-Petch relationship breaks down. For these samples, calculated yield stress values are significantly higher than predicted by the Hall-Petch relation. The reason for the enhanced strength in this case can not solely be attributed to the ultrafine structural size, the deformation induced structures and dispersion strengthening. The flow stress at large structural sizes is governed by dislocation motion. We assume that for small structural sizes, the activation or availability of dislocation sources is the determining factor controlling plasticity. Such a size controlled model is proposed to explain the enhanced yield stresses in thin films compared to their bulk counterparts as well [D24,D25]. This source controlled model predicts a yield stress that scales with the reciprocal of the film thickness. In our case the calculated yield stress should therefore scale with the inverse structural size at small sizes which matches with our aluminium sample results quite well as can be seen in Fig.D7b.

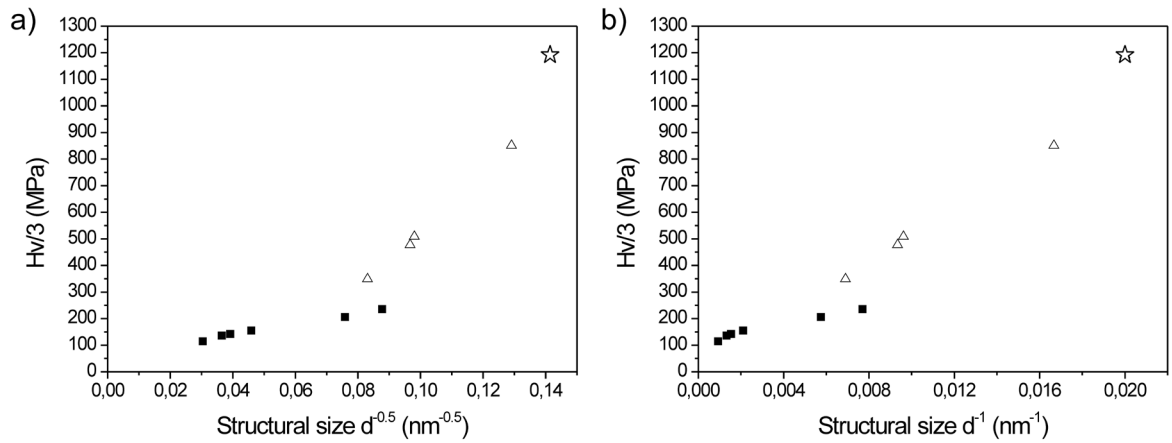

Fig.D7: a) Yield stress plotted as a function of inverse square root of the structural size and b) yield stress plotted as the inverse structural size of all aluminium samples (filled symbols: aluminum foil samples with an initial thickness ti of 11 µm cold rolled to 50%, 78%, 90% and 99% thickness reduction and the aluminium foil samples with a ti of 750 nm cold rolled to approximately 75% and 85% thickness reduction; open symbols: HPT consolidated samples of aluminium powder with a particle size of 1.3 µm and 90 µm and the aluminium foil samples with a ti of 750 nm cold rolled to 90% and 95% thickness reduction). The yield stress is calculated by the Tabor relation in both cases.

Conclusions

Aluminium samples containing dispersed alumina particles were prepared using two different SPD techniques. HPT consolidation and deformation of aluminium powders with two different amounts of alumina particles and cold rolling of layers of aluminium foil with different initial thicknesses were performed. Independent on the starting material and SPD technique, a significantly finer microstructure is obtained if the aluminium contains dispersed alumina particles. The fine grained microstructure is mainly induced by the pinning effect of the introduced alumina particles. Furthermore, it was found that independent of the initial grain size, which corresponds to the initial foil thickness or particle diameter, a reduction in size of the grains by a factor over ten can be achieved by the incorporation of the alumina particles. Accompanied with the reduction in the structural size, the hardness of the materials increased. The reported hardness data shows two different regions: (1) a region to a grain size of about 200 nm where classical Hall–Petch behaviour is found and (2) a region for grain sizes below 200 nm where the Hall–Petch relation roughly holds, but deviates from the classical −0.5 exponent. Furthermore, the HPT deformed aluminium samples exhibit reasonable grain size stability up to remarkable high temperatures for pure aluminium.

Acknowledgements

The financial support by the Austrian Fonds zur Förderung der wissenschaftlichen Forschung (Project number: S10402-N16) is gratefully acknowledged. The author thanks Harald Lehofer for experimental assistance.

References for Publication D

[D1] R.Z. Valiev, T.G. Langdon, Prog. Mater. Sci. 51 (2006) pp. 881–981.

[D2] R.Z. Valiev, R.K. Islamgaliev, I.V. Alexandrov, Prog. Mater. Sci. 45 (2000) 89-103.

[D3] A.P. Zhilyaev, T.G. Langdon, Prog. Mater. Sci. 53 (2008), 893-979.

[D4] R. Pippan, F. Wetscher, M. Hafok, A. Vorhauer, I. Sabirov, Adv. Eng. Mater. 8 (2006), 46-56.

[D5] R. Pippan, S. Scheriau, A. Taylor, M. Hafok, A. Hohenwarter, A. Bachmaier, Annu. Rev. Mater. Res. 42 (2010) 319-344.

[D6] A. Bachmaier, A. Hohenwarter, R. Pippan, Scr. Mater. 61 (2009) 1016–1019.

[D7] A. Bachmaier, M. Hafok, R. Pippan, Mater. Trans. 51 (2010) 8-13.

[D8] A. Bachmaier, R. Schuster, R. Pippan, Rev. Adv. Mater. Sci. 25 (2010) 1-8.

[D9] C.Y. Barlow, P. Nielsen, N. Hansen, Acta Mater. 52 (2004) 3967-3972.

[D10] C.Y. Barlow, N. Hansen, Y.L. Liu, Acta Mater. 50 (2002) 171-182.

[D11] B. Rufino, F. Boulc`h, M.-V. Coulet, G. Lacroix, R. Denoyel, Acta Mater. 55 (2007) 2815-2827

[D12] M.A. Trunoc, M. Schoenitz, X. Zhu, E.L Dreizin, Combust. Flame 140 (2005) 310-318.

[D13] M. Lewandowska. K.J. Kurzydłowski, Mater. Charact. 55 (2005) 395-401.

[D14] L.P.H. Jeurgens, W.G. Sloof, F.D. Tichelaar, E.J. Mittemeijer, Thin Solid Films 418 (2002) 89-101.

[D15] C. Kwan, Z. Wangand, S.-B. Kang,. Mater. Sci. Eng. A 480 (2008) 148-159.

[D16] M. Eizadjou, H. D. Manesh, K. Janghorban, J. Alloys Compd. 474 (2009) 406-415.

[D17] E.O.Hall, Proc.Phys.Soc.London B 64 (1951) 747.

[D18] N.J. Petch, J.Iron Steel Inst. 174 (1653) 25.

[D19] G. Tabor, The Hardness of Metals, Clarendon Press, Oxford, 1951.

[D20] N. Hansen, Acta Metall. 25 (1977) 863-869.

[D21] N. Hansen, Scr. Mater. 51 (2004) 801-806.

[D22] N.C. Kothari, J. Nucl. Mater. 41 (1971) 303-312.

[D23] N. Hansen, Acta Metall. 52 (1970) 137.

[D24] B. von Blanckenhagen, P. Gumbsch, E. Arzt, Phil. Mag. Let. 83 (2003) 1-8.

[D25] R. Venkatraman, J.C. Bravman, J. Mater. Res. 7 (1992) 2040-2048.

Publication E: Microstructure and properties of a Fe-Cu composite processed by HPT powder consolidation

Microstructure and properties of a Fe-Cu composite processed by HPT powder consolidation

A. Bachmaier and R. Pippan

Erich Schmid Institute of Materials Science of the Austrian Academy of Sciences,Jahnstrasse 12, A-8700 Leoben, Austria

Abstract

A method to produce nanocrystalline Fe-Cu composites by means of high-pressure torsion (HPT) deformation is presented. Mixtures of micrometer sized powders of Fe and Cu with different ratios of the two components were precompacted and subsequently deformed by HPT at room temperature to a certain amount of strain. Afterwards, new samples were cut out of these previously deformed samples and further HPT deformation was conducted. The evolution of the microstructure during the different steps of the HPT process and the resulting microstructure of the composites were investigated by scanning electron microscopy. In summary it could be shown that the final attainable grain sizes in the composite materials in the two step process are much smaller than in the simply HPT deformed composites. The reduction of the grain size is also reflected in an enhancement of the hardness.

Keywords

High Pressure Torsion, Fe-Cu composite

Introduction

Severe plastic deformation promises to be a suitable method to produce nanocrystalline or ultra fine grained materials which cannot be obtained by standard methods. In literature, numerous data is reported about the microstructure and mechanical properties of pure metals and alloys processed by severe plastic deformation. In contrast, multiphase materials have rarely been investigated until now.
In this work, the microstructural evolution of a Fe-Cu composite deformed by HPT was investigated. A powder mixture of Cu and Fe powder was chosen as a starting material. Even though the mutual solubility of Fe and Cu is very small, “mechanical” intermixing of the constituents might be possible due to the severe plastic deformation. This fact might allow the formation of new types of materials. Similar phenomena have been observed before in a Cu-Fe composite [E1,E2]. It was shown that for the Cu-Fe composite the production of a non-equilibrium Cu supersaturated solid solution by HPT was feasible. A nanocrystalline Cu-Fe composite with an inhomogeneous layered microstructure was produced, where nanoscaled Fe clusters dissolved into the Cu matrix. Similar results were obtained in powder mixtures of Fe and Cu processed by ball milling which induces alloying of the otherwise immiscible elements [E3-5].
If nanocrystalline Fe-Cu composites with homogeneous microstructures can be produced by HPT deformation of the appropriate powder mixtures, it is not solely an easy way to produce such composites but it would also be interesting for magnetic applications: nanocrystalline Fe-Cu composites with small amounts of Cu should exhibit large magnetostrictive effects [E6].

Experimental

Micrometer sized powders of Fe and Cu were mixed with different ratios (Fe powder with ~5 wt% Cu powder and Fe powder with ~10 wt% Cu powder). Subsequently, the powder mixtures were precompacted directly in our large HPT tool. A detailed description of the HPT equipments is given in [E7,E8]. The precompacted samples had a diameter of 30 mm and a thickness of 10 mm. Afterwards the samples were HPT deformed at room temperature at a pressure of 2.4 GPa for 10 rotations, which corresponds to an equivalent strain of ~30 at a radius of 8 mm. After the deformation, the samples were cut at a radius of 2 mm and 8 mm. From the cut part, a rod with a diameter of 6 mm was turned. Afterwards, the rod was cut into disks with a diameter of 6 mm and a thickness of 0.8 mm. The most central disks were then further HPT deformed in our small HPT tool at room temperature at a pressure of 5 GPa for 50 rotations, which corresponds to an equivalent strain εv of 560 at a radius of 2 mm. Fig.E1 illustrates the production and deformation steps.
Microstructures were characterized in a scanning electron microscope (SEM) type LEO 1525 using back scattered electrons. The directions of the microstructural observations are given in Fig.E1. The micrographs were taken at a radius of 2 mm in tangential and axial direction, respectively. Vickers microhardness measurements were performed on a BUEHLER Mircomet 5100 using a load of 1000 g for all deformation conditions.

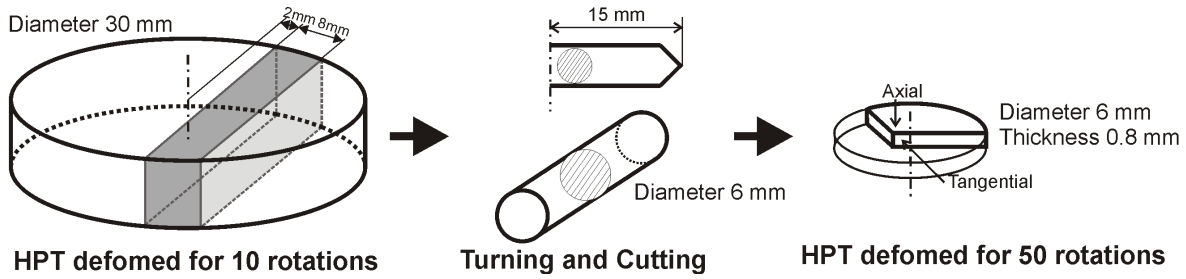

Fig.E1 Sketch illustrating the steps of the sample production: HPT sample with an initial diameter of 30 mm and the following steps for the production of a HPT sample with a diameter of 6 mm for further HPT deformation.

Results

After powder mixing and precompaction, samples with a diameter of 30 mm of the two different compositions were HPT deformed for 10 rotations. Smaller HPT samples were prepared accordingly out of the previously deformed samples (see Fig.E1). These “new” HPT samples were further deformed for 50 rotations: compared to the initial HPT samples, the torsion axis has now changed.

In Fig.E2, the microstructure of the FeCu10% composite after 10 rotations in the axial direction and after 50 rotations in the tangential direction is shown. Due to the lower scattering factor of the Fe phase, the Fe rich regions appear darker in the micrograph in the back scatter electron mode.

In Fig.E2a, the Fe and Cu regions can be easily distinguished. Continuous bands of Cu rich regions are embedded in the Fe matrix and the Cu and Fe phases are not homogeneously distributed. The thickness of the Cu bands is about 1 – 2 µm, which is about ten times smaller than the particle size of the Cu powder in the initial state. The distance between the Cu bands is approximately 10 µm. The accurate position in the initial 30 mm diameter HPT sample cannot be retraced after the cutting and turning process. From the micrograph with the higher magnification an average grain size of 200 and 400 nm for the Fe and Cu phases can be estimated, respectively (Fig.E2b).

In Fig.E2c, the final microstructure after 50 rotations is shown. Compared to the microstructure of the sample where 10 rotations were applied, the grains sizes are clearly reduced. The grains are somewhat elongated in the shear direction but an apparent homogenous microstructure is now obtained. It is not possible to distinguish between the Fe and Cu phases in this case due to the small grain size and lack in contrast. From the micrograph, a grain size of ~ 20-100 nm is estimated whereat a few larger grains are also visible.

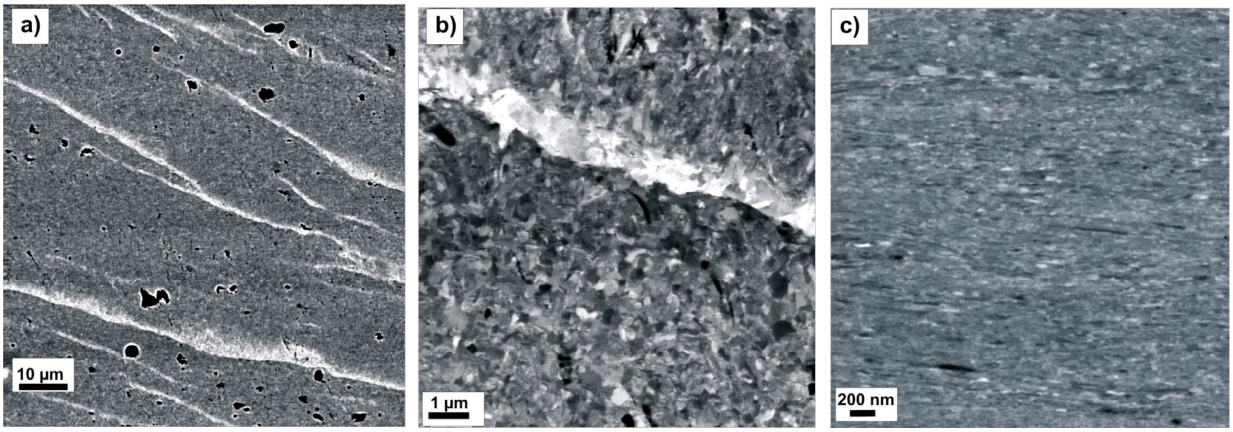

Fig.E2 SEM images of the microstructure of the FeCu10% composite: a) after HPT deformation for 10 rotations in the axial direction, b) after HPT deformation for 10 rotations in the axial direction with a higher magnification and c) HPT deformed for 50 rotations in tangential direction at a radius of 2 mm. Please note the large differences in the magnification.

The microstructure of the FeCu5% composite in the final state after 50 rotations is shown for comparison in Fig.E3. The production steps of these samples are the same as for the FeCu10% composite sample. Comparing both composites, the grain size is further reduced in the case of the FeCu5% composite. From the micrograph, grain sizes of about ~ 20-50 nm are estimated and the grains seem to be more equiaxed in this case.

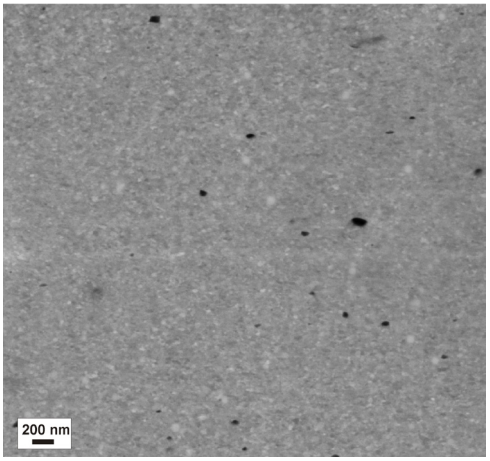

Fig.E3 SEM image of the microstructure of the FeCu5% composite after HPT deformation for 50 rotations in tangential direction at a radius of 2 mm.

Microhardness was measured from the center to the edge (i.e. increasing applied strain) of the different HPT deformed samples. In Fig.E4a the microhardness for the FeCu10% composite samples after 10 and 50 rotations is plotted. After 10 rotations, the microhardness of the FeCu10% composite sample is almost homogeneous along the radius of the disk with values ranging from 250 to 300 HV. After an additional 50 rotations, the hardness increases significantly to about 440 HV in the center of the sample and 600 HV at the outer radius. These findings fit well with the observed microstructure of the deformed samples after 10 and 50 rotations. After 10 rotations, the microstructure is inhomogeneous and bands of Cu are embedded in the Fe matrix. The enhancement of the hardness

after the additional 50 rotations is primarily attributed to the reduction in grain size: in the final state, a nanocrystalline microstructure is reached.

In Fig.E4b, the microhardness of the FeCu5% composite sample compared to the FeCu10% composite sample after 50 rotations is plotted. In the center, the hardness of the FeCu5% composite sample starts with ~ 700 HV and increases continuously to a hardness of ~ 950 HV. The higher hardness of the FeCu5% composite is attributed to strengthening from further grain size refinement if compared to the microstructure of the FeCu10% composite.

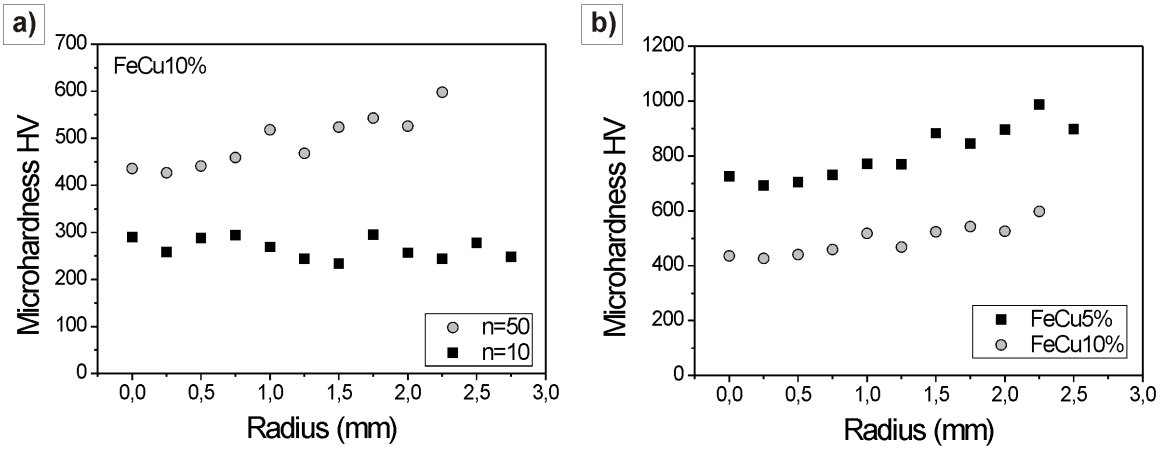

Fig.E4 Microhardness plot along the radius of the HPT disk: a) the FeCu10% composite after 10 (n=10) and after 50 rotations (n=50), b) the FeCu5% and FeCu10% composites after 50 rotations.

The continuous increase in hardness measured from the center to the edge of the disk can be explained by the different microstructures along the radius of the samples in both composites. In spite of the high degree of deformation, saturation in the refinement could not be reached even after 50 rotations. In Fig.E5, the different microstructures occurring along the radius of the disk in tangential direction for the FeCu10% composite are shown as an example: at small strains (radius of ~ 0.2 mm), Cu rich bands in the Fe matrix are visible, which are somewhat elongated in the direction of the shearing (the shear direction is parallel to the longitudinal side of the image). At higher strains (radius of 1 mm), the Cu rich bands are still visible, but their thickness is reduced. Therefore, the grain size of the Cu and Fe phases are further reduced. Finally, at a radius of 2 mm, an apparent homogeneous microstructure is observed. Due to the nanocrystalline microstructure, Cu and Fe phase cannot be longer distinguished from each other. Saturation in hardness or saturation in the refinement process cannot be obtained as long as both phases occur in the composite and as long as both phases are still deformed.

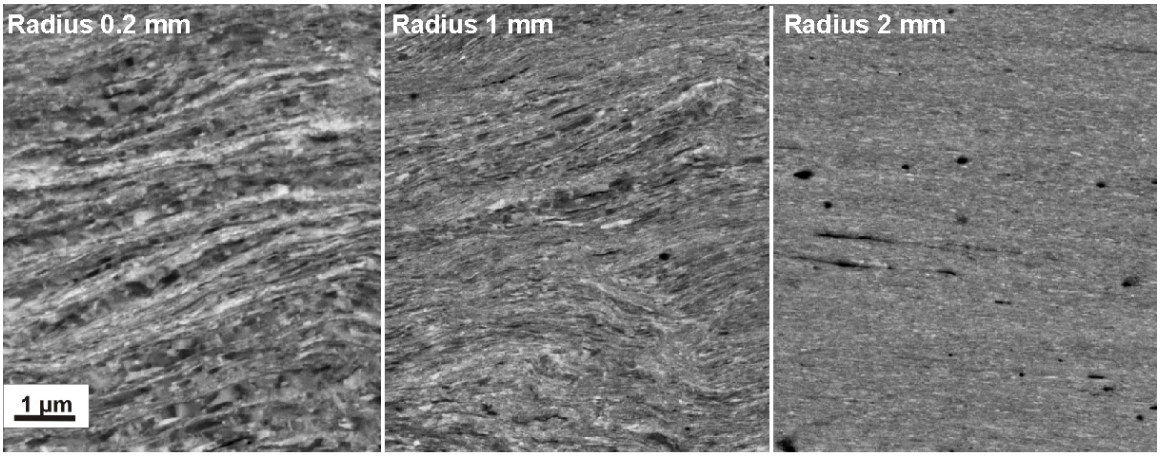

Fig.E5 SEM images of the microstructure of the FeCu10% composite recorded at a radius of ~ 0.2 mm, 1 mm and 2 mm in tangential direction. The magnification is the same in all micrographs.

Summary

Nanocrystalline Fe-Cu composites with a Cu content of 5 and 10 wt% were processed by HPT powder compaction and subsequent deformation. Due to the two-step process with a change in the direction of deformation, a quite homogeneous microstructure at high strains was obtained. Nevertheless, a saturation region, where no further refinement of the microstructure occurs, could not be reached even at a high degree of deformation. In the final state, both composites exhibit a microstructure with a significant smaller grain size compared to pure bulk Fe and Cu samples deformed by HPT [E9-11].
This work focused on the structural evolution during the deformation of the composites. Further investigations will include analysis of possible dissolution mechanism (or possible interdiffusion mechanism) and the magnetic properties of the composites will be examined.

Acknowledgements

The financial support by the Austrian Fonds zur Förderung der wissenschaftlichen Forschung (Project number: S10402-N16) is gratefully acknowledged.

References for Publication E

[E1] X. Sauvage and R. Pippan: Mater. Sci. Eng. A 410-411 (2005), p. 345-347

[E2] X. Sauvage, F. Wetscher and P. Pareige: Acta Mater. 53 (2005), p.2127-2135

[E3] A.R. Yavari, P.J. Desré and T. Benameur: Phys. Rev. Lett. 68 (1992), p. 2235

[E4] J. Eckert, J.C. Holzer and W.L. Johnson: J. Appl. Phys. 73 (1993), p. 131

[E5] J.Y. Huang, Y.D. Yu, Y.K. Wu, D.X. Li and H.Q. Ye: Acta Mater. 45 (1997) p. 113-124

[E6] P. Gorria, D. Martinez-Blanco, R. Iglesias, S.L. Palacios, M.J. Perez, J.A. Blanco, L. Fernandez Barquin, A. Hernando and M.A. Gonzales: J. Magn. Magn. Mater. 300 (2006) p.229-233

[E7] R. Pippan, S. Scheriau, A. Taylor, M. Hafok, A. Hohenwarter and A. Bachmaier: Annu. Rev. Mater. Res. Vol. 40 (2010), p.319-343

[E8] R. Pippan, S. Scheriau, A. Hohenwarter and M. Hafok: Mater. Sci. Forum Vol. 584–586 (2008), p. 16–21

[E9] G. Khatibi, J. Horky, B. Weiss and M.J. Zehetbauer: Int. J. Fatigue Vol. 32 (2010), p. 269-278

[E10] T. Hebesberger, H.P. Stüwe, A. Vorhauer, F. Wetscher and R. Pippan: Acta Mater. Vol. 53 (2005), p. 393-402

[E11] R.Z. Valiev, Y.V. Ivanisenko, E.F. Rauch and B. Baudelet: Acta Mater. 44 (1996), p. 4705

Publication F: The formation of supersaturated solid solutions in Fe-Cu alloys deformed by High-pressure torsion

The formation of supersaturated solid solutions in Fe-Cu alloys deformed by High-pressure torsion

A. Bachmaier[a], M. Kerber[b], D.Setman[b] and R. Pippan[a]

[a]Erich Schmid Institute of Materials Science – Austrian Academy of Sciences, Jahnstr.12, A-8700 Leoben, Austria

[b]Research Group Physics of Nanostructured Materials, University of Vienna, Boltzmanngasse 5, A-1090 Vienna, Austria

Abstract

Fully dense bulk nanocomposites have been obtained by a novel two step severe plastic deformation process in the immiscible Fe-Cu system. Elemental micrometer sized Cu and Fe powders were first mixed in different compositions and subsequently High-Pressure torsion consolidated and deformed in a two step deformation process. Scanning electron microscopy, X-ray diffraction and atom probe investigations were performed to study the evolving far from equilibrium nanostructures which were observed at all compositions. For lower and higher Cu contents a complete solid solution of Cu in Fe and Fe in Cu is obtained, respectively. In the near 50% regime a solid solution face-centred cubic and solid solution body-centred cubic nano grained composite has been formed. After an annealing treatment, these solid solutions decompose and form two phase nanostructured Fe-Cu composites with a high hardness and an enhanced thermal stability. The grain size of the composites retained nanocrystalline up to high annealing temperatures.

Keywords

High-pressure torsion, Solid solubility extension, Fe-Cu alloy

1. Introduction

Due to novel properties of materials fabricated out of typically immiscible alloys like high thermal and electrical conductivity and excellent magnetic properties (i.e. high magnetoresistance and coercivity), a long standing interest in preparation of such alloys exists [F1-3]. The formation of metastable phases in alloy systems with a negative heat of mixing as well as positive heat of mixing has been intensively investigated in recent years [F3-6]. Since the 1990s, the formation of metastable single phase solid solutions with nanocrystalline grain sizes for mechanically alloyed Fe-Cu powders has been studied extensively by several research groups [F7-13]. The Fe-Cu system, a spinodal type system, is nearly immiscible in equilibrium at room temperature and up to 600°C and has a positive heat of mixing [F14]. Due to mechanical alloying, the potential to extend the mutual solubility of Fe and Cu has been widely reported due to friction and strong impacts of the steel balls on the powder grains. The formation of face-centred cubic (f.c.c.) single phase solid solutions is observed for Fe_xCu_{1-x} alloys with a Fe content x<60at%, two phase alloys consisting of a f.c.c and a body-centred cubic (b.c.c) phase are formed for a Fe content of 60<x<80at% and b.c.c single phase solid solutions are obtained for a Fe content x>80at% [F8-10]. The mixing occurs on the atomic level in the milled alloys which was confirmed by Mössbauer spectroscopy [F8,F11]. The crystallite size in the milled powders is reported to be about 20 nm or even smaller. Decomposition of the unstable FeCu solid solutions occurred due to annealing treatments as reported in several studies [F10-12].

In this study, a new approach to obtain fully dense homogeneous bulk Fe-Cu composites by High-Pressure torsion (HPT) deformation is presented. Sauvage et al. showed that by HPT deformation the production of a non-equilibrium Cu supersaturated solid solution in a Cu-Fe composite was possible [F15, F16]. Many structural defects are incorporated in a material during severe plastic deformation (SPD) processes which is accompanied with a higher dislocation density, a higher vacancy concentration and the continuous formation of new grain boundaries [F15-18]. A Cu-Fe composite with an inhomogeneous layered nanostructured microstructure was produced, where nanoscaled Fe clusters dissolved into the Cu matrix.

Instead of a filamentary composite starting material micrometer sized Fe and Cu powders are used which is similar as in the mechanical alloying process. Nevertheless, the product after mechanical alloying is a powder and further processes like compaction and sintering are necessary to obtain bulk specimens. One emerging disadvantage is that the nanocrystalline structure can be lost during these treatments and decomposition of the supersaturated solid solutions occurs during annealing. Furthermore, an increase of the impurity content is unavoidable. The advantage of the HPT process is that the end product is directly available as a massive bulk material. Up to now it was impossible to generate homogeneous nanocrystalline supersaturated FeCu composites by HPT or Equal Angular Channel Pressing micrometer sized powder consolidation. One of the goals in this study was to find a way to overcome these problems. If nanocrystalline supersaturated Fe-Cu composites with homogeneous microstructures can be produced by HPT deformation, it would be an easy way to produce such composites which are also very interesting materials for magnetic applications. F.c.c

supersaturated solid solutions are ferromagnetic for a Fe content x>15. Furthermore, nanocrystalline Fe-Cu composites with small amounts of Cu should exhibit large magnetostrictive effects [F19-21].

2. Experimental

Commercial copper powders (99.9% purity, -170+400 mesh,) and iron powders (99.9% purity, -100+200 mesh) were used as starting material. These micrometer sized powers were mixed in different ratios to obtain powder mixtures with final alloy compositions of $Fe_{100-x}Cu_x$ (x= 15, 30, 50, 85). The powder mixtures were precompacted and deformed in our large HPT tool which can be used to deform samples up to a diameter of 50 mm and a thickness of about 10 mm. Afterwards, new smaller HPT samples were cut out of the previously deformed sample. Therefore, the sample was cut at a radius of 5 and 15 mm, a cylindrical rod was turned from the cut part and slices of ~ 0.8 mm thickness were cut from this rod. These “new” HPT samples were deformed a second time. The reason for this special procedure will be discussed later. The single steps of the sample production are illustrated in the schematic sketch in Fig.F1.

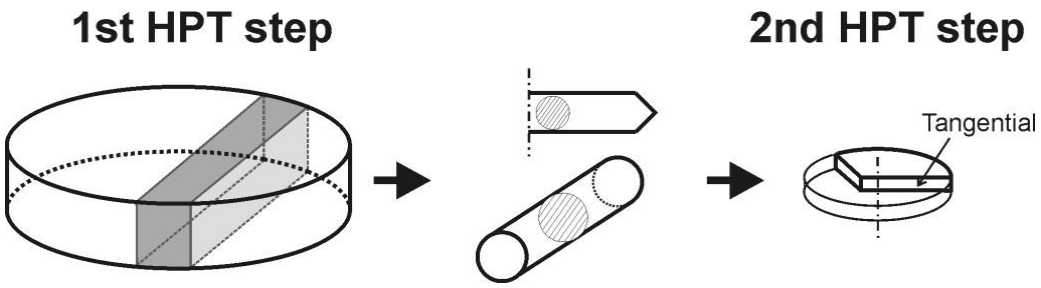

Fig.F1 Schematic sketch of the individual sample production and deformation steps: From the sample (diameter of 50 mm) deformed in the first HPT deformation step, new samples (diameter of 8 mm) are cut and further HPT deformation is conducted. The direction in which all microstructural observations are conducted is also shown.

Further information about HPT deformation and a detailed description of the HPT equipments is given in [F22-24]. A list of the deformation parameters of both processing steps for all samples deformed in this study is given in Table 1.

All microstructural investigations were performed at a radius of 10 mm of the HPT sample after the first deformation step and at a radius of 3 mm after the second deformation step in tangential direction with a scanning electron microscope (SEM) type LEO 1525 using back scattered electrons. The direction of the SEM observations is also shown in Fig.F1. Vickers microhardness measurements were performed on a BUEHLER Mircomet 5100 using a load of 500 g. Indents were made across the radii of the samples with a distance of 0.25 mm between the indents on the 8 mm diameter disks after the cutting procedure described above. After the first processing step, nearly constant hardness values are measured across the radii of the samples and the mean values of 32 indents over the radii of the samples are given. In contrast, mean values of 16 indents starting from a radius of 2 mm to the outer edge of the sample are reported after the second processing step in this study which corresponds to the saturation region. X-ray diffraction measurements were taken with an AXS BRUKER D8 system in

Bragg-Brentano θ-2θ geometry using Co (K_α) radiation. Furthermore an atom probe analysis has been carried out on the $Fe_{50}Cu_{50}$ sample. Bars with dimension of 0.3x0.3x3 mm of the HPT deformed sample were cut out and tips at a radius of 3 mm referred to the HPT sample have been produced by a standard two step electrochemical polishing procedure. The atom probe analysis was conducted on a LEAP 3000X HR from Cameca® which was former Imago Scientific Instruments. The sample was measured with a pulsed laser with a frequency of 250 kHz, a temperature of 40 K and a laser pulse energy 0.5 nJ. The software package IVAS 3.4.3 from Cameca® was used for reconstruction of the probed volume and the data analysis.
Differential scanning calorimetry (DSC) with a PERKIN ELMER DSC-7 was performed to evaluate the decomposition temperature of the FeCu alloys with 10°C/min of heating rate up to a temperature of 590°C on ring samples (inner diameter 2 mm, outer diameter 3 mm) cut out of the samples after both deformation steps.

	1. Deformation Step			**2. Deformation Step**		
	# rotations	thickness (mm)	Ø (mm)	# rotations	thickness (mm)	Ø (mm)
$Fe_{85}Cu_{15}$	10	9,5	50	50	0,5	8
$Fe_{70}Cu_{30}$	10	9,5	50	100	0,6	8
$Fe_{50}Cu_{50}$	20	9,6	50	200	0,5	8
$Fe_{15}Cu_{85}$	20	11,5	50	100	0,5	8

Table F1: Deformation parameters of the first and second deformation step for all deformed samples in this study.

3. Results

3.1. Formation of supersaturated solid solutions

After powder mixing to obtain the different compositions ($Fe_{85}Cu_{15}$, $Fe_{70}Cu_{30}$, $Fe_{50}Cu_{50}$ and $Fe_{15}Cu_{85}$) and precompaction of the powder mixtures directly in the HPT tool, the precompacted samples with a diameter of 50 mm were HPT deformed for 10-20 rotations. Fig.F2 shows the microstructure of the $Fe_{70}Cu_{30}$ and $Fe_{85}Cu_{15}$ samples after the deformation at a lower and at a higher magnification. Due to the lower scattering factor of the Fe phase, the Cu rich regions appear brighter in the back scatter electron mode and the Fe and Cu regions can be easily distinguished. Continuous bands of Cu rich regions (thickness 1-2 µm) are embedded in the Fe matrix and the Cu and Fe phases are not homogeneously distributed in the case of the $Fe_{85}Cu_{15}$ alloy. The thickness of the Cu bands is about ten times smaller than the particle size of the Cu powder in the initial state but the distance between the Cu bands differ a lot. From the micrograph with the higher magnification an average grain size of 300 and 200 nm for the Fe and Cu phases in $Fe_{85}Cu_{15}$ composite can be estimated using the back scattered electron mode. In the $Fe_{15}Cu_{85}$ composite, similar grain sizes are observed (300 nm for Cu, 300 nm for Fe).

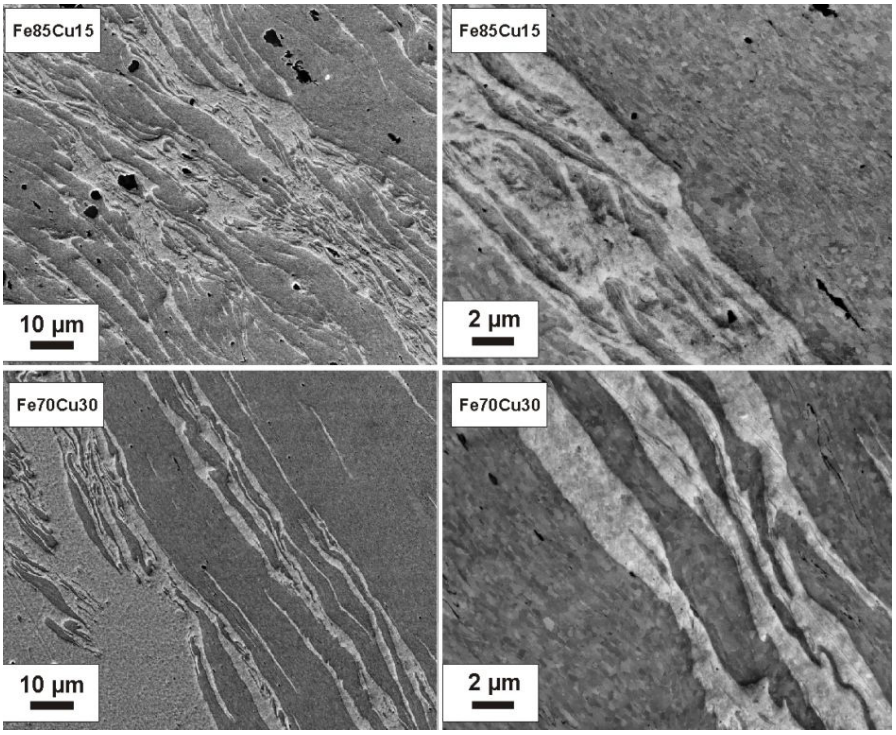

Fig.F2 SEM micrographs (back scattered electron mode) showing the microstructure of the $Fe_{85}Cu_{15}$ and the $Fe_{70}Cu_{30}$ after the first deformation step with a low and high magnification recorded at a radius of 10 mm in tangential direction. Fe rich regions appear darker in the image, Cu regions brighter.

In the $Fe_{70}Cu_{30}$ composite, the Cu and Fe phase can also be differentiated very easily. From the micrograph with the higher magnification, Fe and Cu grains with a similar grain size of about 300 nm and 200 nm can be seen. In the $Fe_{50}Cu_{50}$ composite, the grain size in the Cu and Fe phase are again similar (about 300 nm for Cu and 400 nm for Fe).

In Fig.F3, the final microstructures of the $Fe_{85}Cu_{15}$, $Fe_{70}Cu_{30}$, $Fe_{50}Cu_{50}$ and $Fe_{15}Cu_{85}$ samples after the second processing step are shown. Compared to the obtained microstructures after the first processing step, the grain size is significantly reduced in all four samples. In the $Fe_{85}Cu_{15}$, $Fe_{50}Cu_{50}$ and $Fe_{15}Cu_{85}$ samples an apparent homogeneous microstructure is obtained. The $Fe_{15}Cu_{85}$ sample shows a somewhat larger grain size compared to the other microstructures but still a nanocrystalline microstructure is obtained. In the $Fe_{70}Cu_{30}$ sample, an inhomogeneous layered microstructure can be seen. The darker regions are Fe rich regions whereas the brighter regions are Cu rich regions. Very thin Fe layers with a thickness significantly below 50 nm are drawn trough the Cu matrix and vice versa. The grain size is nanocrystalline as well.

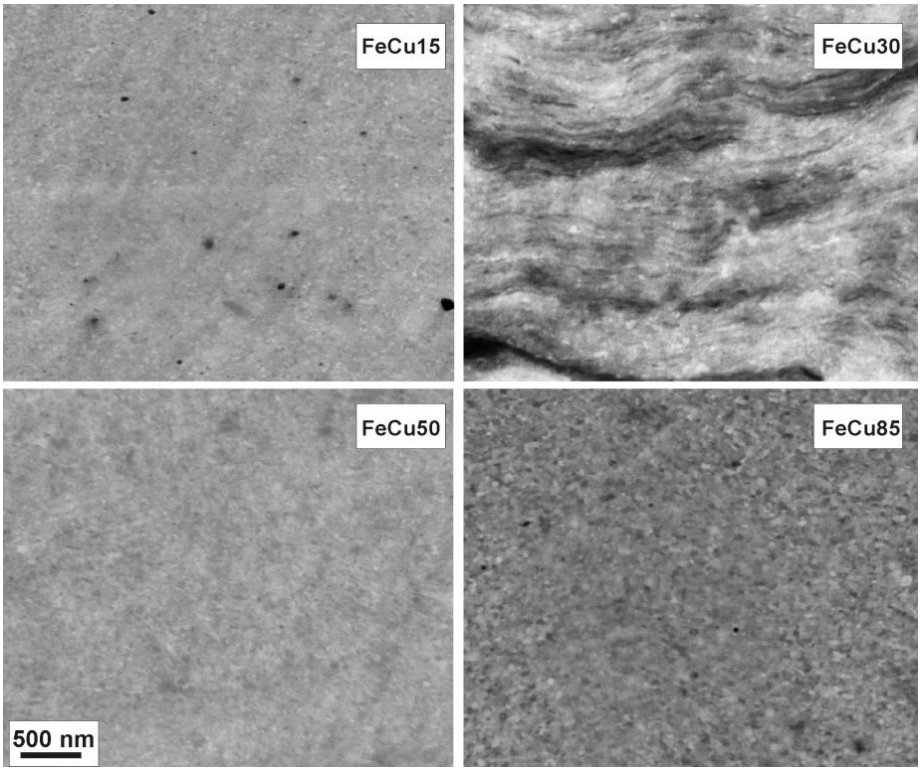

Fig.F3 SEM micrographs (back scattered electron mode) showing the final microstructure after both processing steps in all alloys ($Fe_{85}Cu_{15}$, $Fe_{70}Cu_{30}$, $Fe_{50}Cu_{50}$, $Fe_{15}Cu_{85}$) recorded at a radius of 3 mm in the tangential direction. The magnification is the same in all images.

The mean microhardness values of the samples after the first and second processing step can be seen in Fig.F4. The first step of the HPT deformation leads to a hardness of 187 HV for the composite with the highest Cu content. Decreasing the Cu content increases the hardness after the first processing step up to a value of 341 HV for the $Fe_{85}Cu_{15}$ composite. After the second processing step, microhardness values increased nearly twice in all samples. Between the $Fe_{50}Cu_{50}$ and $Fe_{70}Cu_{30}$ samples, nearly no hardness difference exists. From the micrographs, it is not possible to distinguish between Fe and Cu phases in the case of the $Fe_{85}Cu_{15}$, $Fe_{50}Cu_{50}$ and $Fe_{15}Cu_{85}$ samples. Therefore, X-ray diffraction investigations were performed to study the occurring phases after the first and second deformation step.

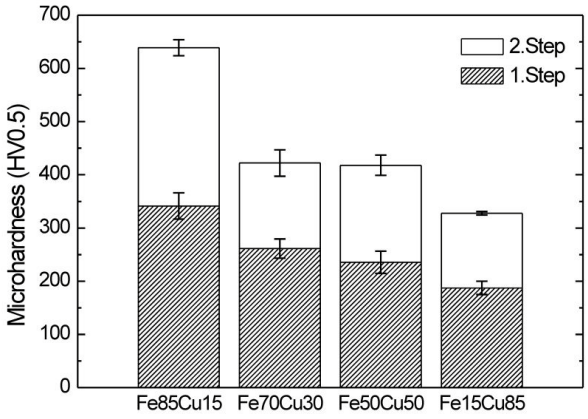

Fig.F4 Microhardness of the FeCu samples after the first and second deformation step. Mean values of 32 indents over the radii of the samples after the first processing step and mean values of 16 indents starting from a radius of 2 mm to the outer edge of the samples after the second processing step are given.

In Fig.F5, X-ray diffraction patterns for all four alloy compositions after the first and second deformation step are shown. In the X-ray diffraction pattern of the $Fe_{85}Cu_{15}$ alloy, peaks of the f.c.c. Cu phase and the b.c.c. Fe phase are visible after the first deformation step (Fig.F5a). This result is consistent with the microstructure of this alloy which shows a composite structure in the micrograph consisting obviously of Fe and Cu (Fig.F2). In general, no peaks from oxides or other contaminants are observed in all diffraction patterns. After the second deformation step, the X-ray diffraction pattern of the $Fe_{85}Cu_{15}$ alloy contains only peaks of the b.c.c Fe phase. Therefore, we assume that supersaturated solid solution of Cu in Fe is formed after this processing step. Furthermore, both b.c.c. Fe peaks have significantly broadened due to the reduction of the mean grain size as confirmed from the micrographs of the microstructure after the first and second deformation step. Moreover, the intensity of the Fe (110) peak increased. The Fe peaks are also shifted to lower angles compared to those recorded after the first deformation step, which might be due to the formation of a Cu solid solution in Fe. Fig.F5d shows the X-ray diffraction pattern of the $Fe_{15}Cu_{85}$ alloy. After the first deformation step, f.c.c. Cu peaks and a weak Fe (110) peak are visible. After the second deformation step, the intensity of the Cu (111) peak increased significantly. The Fe peaks completely disappeared and only Cu peaks remain vice versa as in the case of the $Fe_{85}Cu_{15}$ alloy. In the $Fe_{15}Cu_{85}$ alloy, the Cu (111) peak is now shifted to lower diffraction angles which might now be due to the formation of supersaturated Fe solid solution in the Cu phase. Furthermore, some peak broadening is also observed which is again due to the reduction of the mean grain size.

In the X-ray diffraction patterns of the $Fe_{70}Cu_{30}$ alloy (Fig.F5b), diffraction peaks related to the f.c.c. Cu and the b.c.c Fe phase are observed after the first as well as after the second deformation step. The intensity of the Cu peaks increased somewhat after the second deformation step and the intensity of the Fe peaks is diminished at the same time. Furthermore, both sets of peaks show a broadening after the second deformation step. The Cu peaks are also slightly shifted to lower diffraction angles after the

second deformation step. Similar results are obtained in the $Fe_{50}Cu_{50}$ alloy (Fig.F5c). In turn, a two phase structure consisting of f.c.c. Cu and b.c.c. Fe is obtained at both deformation steps. The intensity of the Fe peaks after the second deformation step is again reduced whereas the intensity of the Cu peak is slightly increased. Moreover, broadening of the peaks after the second deformation step is observed as well. The position of the Cu peaks after the second deformation step is shifted to lower diffraction angles.

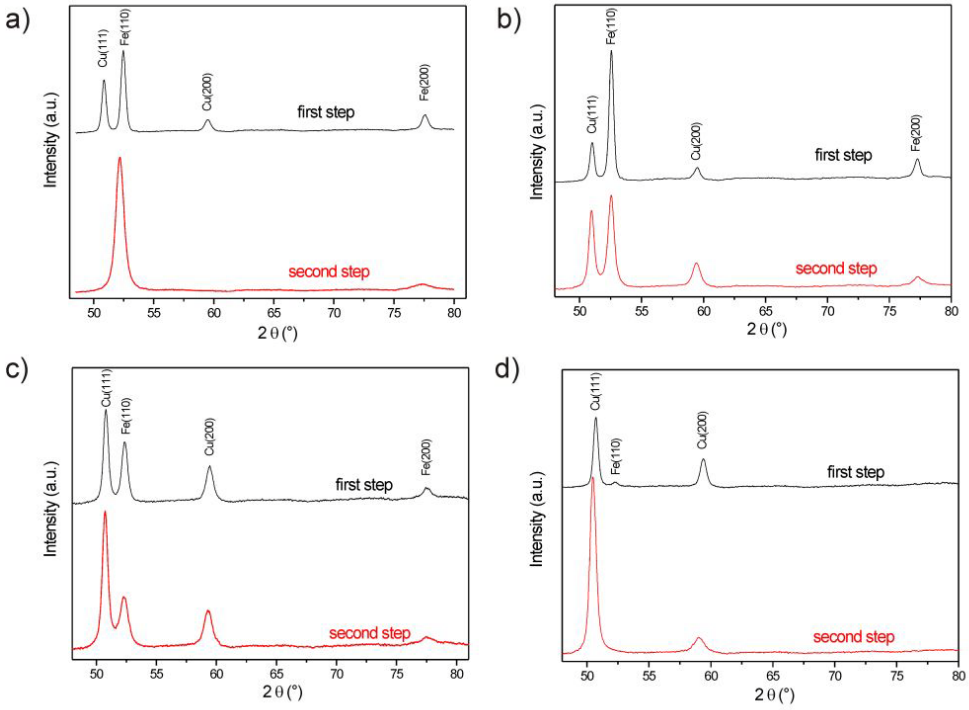

Fig.F5 X-ray diffraction patterns after the first deformation step and second deformation step of the $Fe_{85}Cu_{15}$ alloy (a), the $Fe_{70}Cu_{30}$ alloy (b), the $Fe_{50}Cu_{50}$ alloy (c) and the $Fe_{15}Cu_{85}$ alloy (d), respectively.

Generally, the Cu peaks in the X-ray diffraction pattern of the $Fe_{70}Cu_{30}$, $Fe_{50}Cu_{50}$ and $Fe_{15}Cu_{85}$ samples after the second deformation step are all shifted to lower diffraction angles. In case of the $Fe_{85}Cu_{15}$ sample, the Fe peaks are shifted to lower diffraction angles. A two phase structure is maintained in the $Fe_{70}Cu_{30}$ and $Fe_{50}Cu_{50}$ sample even after both processing steps are conducted. Based on the results from the X-ray diffraction experiments it might be assumed that for Cu contents >30wt%, Cu supersaturated solid solutions are formed even if not a complete single phase structure is obtained. For Fe contents >85%, Fe supersaturated solid solutions are achieved.

Atom probe analysis on the $Fe_{50}Cu_{50}$ sample was conducted to evaluate the possible formation of supersaturated solid solutions in the two phase structures and to map the distribution of Fe and Cu atoms in a volume of 65x66x285 nm³ (Fig.F6a). Cu atoms are displayed in green and Fe atoms in blue, respectively. The Cu as well as the Fe concentration profile across a smaller analyzed volume is shown in Fig.F6b. Grain sizes of both phases around 10 nm can be estimated from this plot. The Cu as well as the Fe concentration profile exhibits gradients which might indicate Fe-Cu interdiffusion. The Cu concentration in the Fe phase is up to ~25 at% and the Fe concentration in the Cu phase is up to ~20 at%. Under equilibrium conditions, the mutual solubility of Fe and Cu is normally less than 0.1

at% at room temperature. Therefore, these data confirms that the formation of Fe supersaturated solid solutions as well as of Cu supersaturated solid solutions is simultaneously possible in the two phase structure.

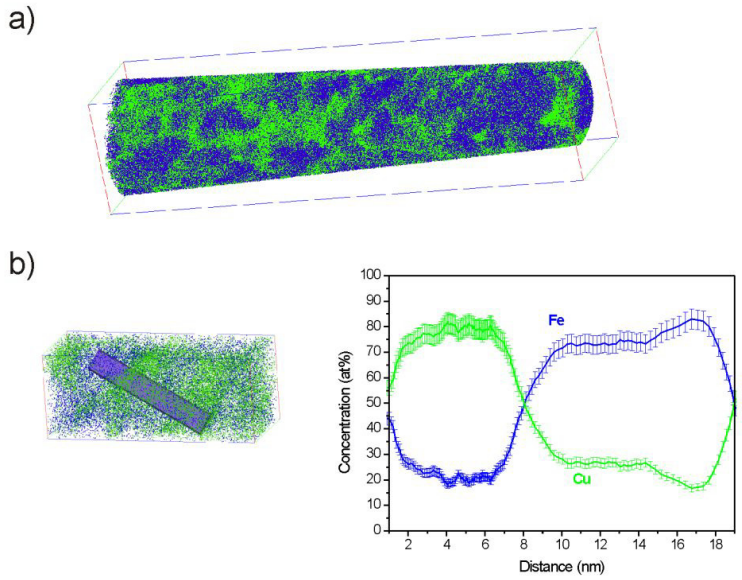

Fig.F6 Atom probe data of the $Fe_{50}Cu_{50}$ alloy after both deformation steps: (a) 3D reconstructed volume (65x 66x 285 nm³) where Cu atoms are displayed in green and Fe atoms in blue, respectively. (b) Cu concentration profile (green) and Fe concentration profile (blue) across the Cu/Fe interfaces.

3.2. Thermal stability

In the following section, the thermal stability of the single phase supersaturated solid solutions of the $Fe_{85}Cu_{15}$ and $Fe_{15}Cu_{85}$ samples are investigated. The samples are annealed at three different annealing temperatures for 1h at air. To monitor a possible thermal decomposition process, the samples are investigated by X-ray diffraction after each annealing step. Furthermore, DSC measurements are conducted to determine the temperature of the decomposition process. Fig.F7 shows the X-ray diffraction patterns of the $Fe_{85}Cu_{15}$ and $Fe_{15}Cu_{85}$ alloy after annealing for 1 h at 290°C, 440°C and 620°C and after the second deformation step without an annealing treatment as a reference (indicated as RT in the plot). After annealing for 1h at 290°C, the diffraction pattern of the $Fe_{15}Cu_{85}$ alloy sample consists of just Cu peaks. No peaks belonging to the b.c.c. Fe phase are visible. Moreover, the width of the Cu peaks decrease which might be due to thermal relaxation of the structure. With annealing at 440°C, the b.c.c. Fe phase peaks appear which is a clear sign of the decomposition of the initial single f.c.c. $Fe_{15}Cu_{85}$ phase into an f.c.c. Cu and b.c.c. Fe phase. After annealing at 620°C, the X-ray diffraction pattern does not change very much. F.c.c. Cu as well as b.c.c. Fe peaks are now visible indicating that decomposition into a two phase structure has occurred at annealing temperatures higher than 440°C. With increasing annealing temperature, the Cu peaks are continuously shifted to higher diffraction angles which are a further indication for the decomposition of the structure. The single phase supersaturated solid solution is remained in the $Fe_{85}Cu_{15}$ alloy sample until annealing temperatures below 440°C. After annealing at 440°C for 1h, Cu

peaks appear in the X-ray diffraction pattern. Therefore, decomposition of the initial single b.c.c. $Fe_{85}Cu_{15}$ phase into f.c.c. Cu and b.c.c. Fe occurs. At an annealing temperature of 620°C, b.c.c Fe and f.c.c. Cu peaks are visible. Moreover, the slight shift of the Fe peaks to lower diffraction angles is reversed with increasing annealing temperature which is again a further indication for the decomposition of the single phase structure. Small thermal relaxation of the structure might also occur in this alloy at low annealing temperatures.

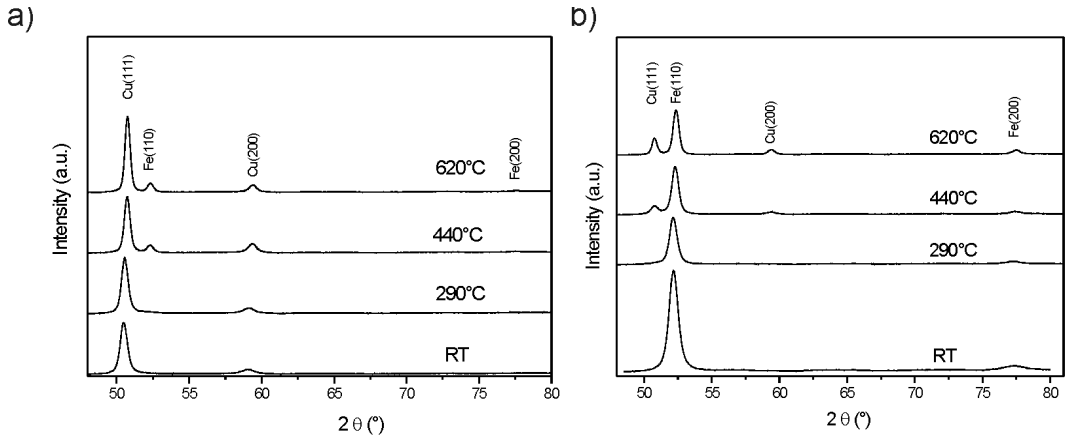

Fig.F7 X-ray diffraction patterns of the $Fe_{15}Cu_{85}$ alloy (a) and the $Fe_{85}Cu_{15}$ alloy (b) sample recorded in the as deformed condition (both deformation steps) and after annealing for 1h at 290°C, 420°C and 620°C.

As an example, the microstructural evolution of the $Fe_{15}Cu_{85}$ sample with increasing annealing temperature is shown in Fig.F8. Compared to the as deformed condition, no significant difference is visible between the microstructures in the sample annealed at 290°C and 440°C. From the micrographs, no distinction between Fe and Cu grains can be made although a two phase structure has already formed at 440°C as confirmed by X-ray diffraction. At annealing temperatures of 620°C, grain growth has occurred and grains with a size above 100 nm are visible. The microstructural evolution of the $Fe_{85}Cu_{15}$ sample is similar. Until annealing at the highest annealing temperature, no difference between the as deformed and annealed microstructures is visible. No change in the grain size is observed after annealing for 1h at 290°C and 440°C and from the micrographs it is not possible to distinguish between Fe and Cu grains. Only at the highest annealing temperature, marginal grain growth occurs as well.

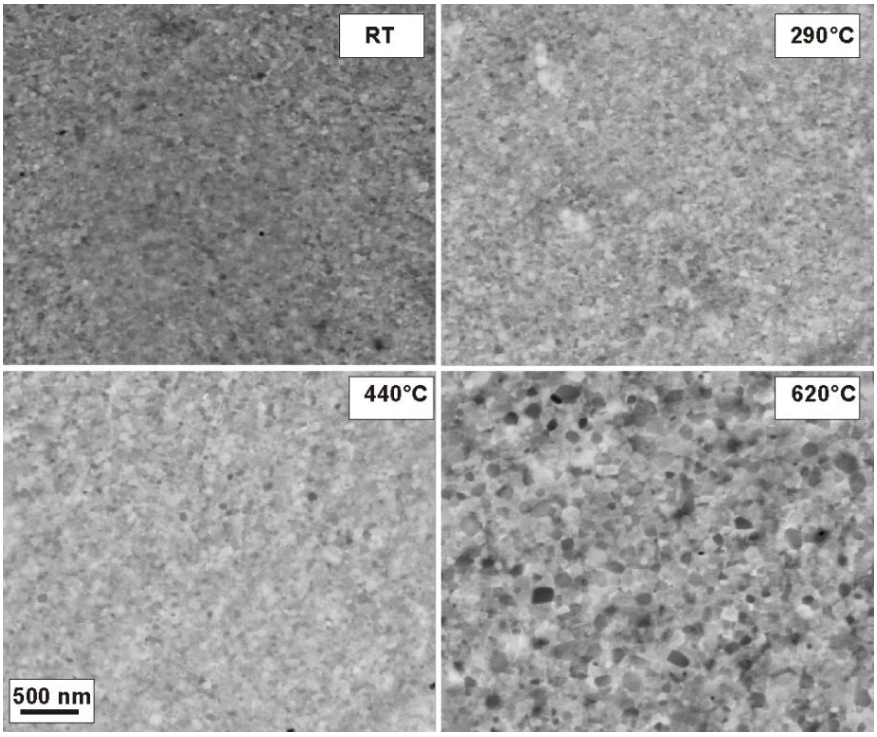

Fig.F8 SEM micrographs (back scattered electron mode) showing the microstructure of the $Fe_{15}Cu_{85}$ alloy in the initial condition (RT) and after annealing for 1h at 290°C, 420°C and 620°C recorded at a radius of 3 mm in tangential direction.

In Fig.F9, the microhardness as a function of annealing temperature of the $Fe_{85}Cu_{15}$ and $Fe_{15}Cu_{85}$ samples is plotted. In the $Fe_{85}Cu_{15}$ sample, the hardness increases with increasing annealing temperatures in the beginning. The hardness of the as deformed sample is 639 HV whereas the hardness after annealing at 290°C and 440°C is 642 and 675 HV, respectively. At the highest annealing temperature, the hardness decreases and has a somewhat lower value compared to the as deformed condition (576HV). First of all there is a slight increase in the hardness in the $Fe_{15}Cu_{85}$ sample during annealing. The hardness of the as deformed sample is 327HV and the hardness after annealing at 290°C is 330HV. At 440°C a higher hardness value of 337HV compared to the initial condition is measured but at the highest annealing temperature the hardness decreases to 277HV. In both samples, the measured hardness values are higher compared to the as deformed condition if decomposition of the supersaturated solid solution has occurred. At the highest annealing temperature, the hardness of both samples decreased which is due to the occurrence of marginal grain growth during the annealing treatment as shown for example for the annealed $Fe_{15}Cu_{85}$ sample in Fig.F9.

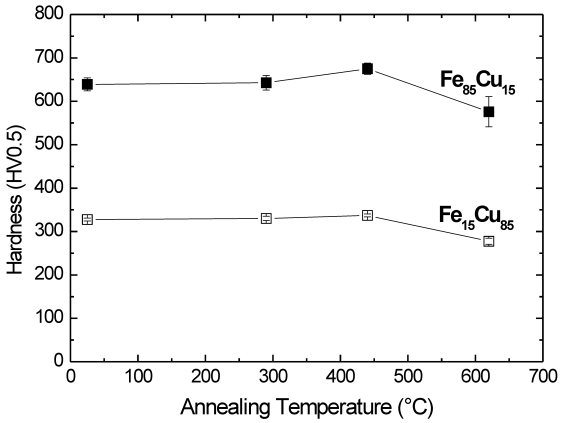

Fig.F9 Microhardness of the $Fe_{15}Cu_{85}$ alloy and the $Fe_{85}Cu_{15}$ alloy sample after annealing for 1h at 290°C, 420°C and 620°C. Mean values of 16 indents starting from a radius of 2 mm to the outer edge of the sample are reported.

DSC of the $Fe_{15}Cu_{85}$ sample shows a broad exothermic signal extending from 302°C to 585°C during heating from room temperature to higher temperatures. Integration of the area under the DSC curve yields to a total stored energy of 43.9 J/g with a peak temperature of 434°C. Such an exothermic event might be attributed to the transition from the metastable supersaturated phases to the stable two phase structure which fits well with the results obtained from the X-ray diffraction experiments. It indicates that the phase separation process is completed when reaching a temperature above 585°C. In the case of the $Fe_{85}Cu_{15}$ sample, a smaller exothermic peak extending from 300°C to 483°C is observed with a total stored energy of 13.1 J/g and a peak temperature of 385°C. This is again attributed to the decomposition of the supersaturated phase to the stable elemental Fe and Cu phases which starts at approximately the same temperature and is completed at a somewhat lower temperature of 480°C than in the $Fe_{15}Cu_{85}$ sample.

4. Discussion

From the experiments it is concluded that three composition regions can be distinguished in the as deformed state after the two-step HPT process: a nanocrystalline f.c.c supersaturated Cu phase at high Cu contents, a mixture of nanocrystalline supersaturated f.c.c Cu and b.c.c. Fe phase for medium Cu contents and a nanocrystalline supersaturated b.c.c. Fe phase for low Cu contents. Therefore, the formation of supersaturated solid solutions over the whole composition range occurs as a result of HPT deformation. After the first processing step, however, a two phase ultrafine grained material is formed. Depending on composition, the grain size of Cu is between 200 nm and 300 nm and around 300nm and 400 nm for Fe. After the second processing step, a much smaller grain size is reached. The nanocrystalline grain size obtained in the composites is significantly smaller compared to pure Fe and Cu deformed by SPD [F25,F26].

4.1. Why is a two step process necessary?

If continuous shearing of the individual Fe and Cu powder components in the composite during HPT deformation and volume conservation is assumed, their thickness decreases with increasing applied deformation. If d_o denotes the initial particle size and γ is the applied shear strain, their thickness d_1 after HPT deformation can be estimated for larger γ to be

$$d_1 = d_0/\gamma . \quad (1)$$

If powders with a mean initial particle size d_o of about 50 µm (like the Cu powders in this study) are deformed to a shear strain of γ 100, their thickness or their size after the deformation is about 500 nm. This result fits very well to the observed microstructures in the deformed composite materials where a two phase structured material is clearly observed in all compositions (Fig.F2). In the individual components of the composite, an ultrafine grained microstructure is formed. With monotonic shear deformation like in the HPT process and Equal Channel Angular Pressing very high amounts of deformation are necessary to reach about 2 nm distance between two phases which are reported to be a basic requirement in the case of Fe for alloying of Fe and Cu and to initiate the formation of supersaturated solid solutions in the Fe-Cu system [F14]. Using equation 1 and assuming d_0=50 µm to obtain a 2 nm spacing would require a γ of 20000. This is in principle possible by HPT but it is extraordinary time and energy consuming. The large necessary strain becomes evident if one considers a lamellar structure and applies a simple shear in the direction parallel to the aligned lamellae. Such a shear dies not change the lamellar spacing.

On account of this and to further increase the effectiveness of the deformation process, a novel two-step HPT process was developed (Fig.F10a). After the shear deformation is applied in one direction, new samples are fabricated out of these already deformed samples which are further deformed by HPT. Due to the cutting process, a rotation of the shearing direction by 90° is also introduced. The shear direction and lamellar alignment are now perpendicular to each other. The thickness d_2 of the lamella of the individual components after both HPT deformation steps can now assumed to be

$$d_2 = d_1/\gamma_2 = d_0/\gamma_1 \cdot \gamma_2 \quad (2)$$

where γ_1 denotes the applied shear strain in the first deformation step and γ_2 is the applied shear strain in the second deformation step. If now a shear strain of γ_1 100 is applied in the first HPT deformation step and a shear strain of γ_2 100 is applied in the second HPT deformation step, the final thickness of the individual components should become 5 nm or lower.

As an example for the effectiveness of the two step HPT process, the microhardness of the $Fe_{85}Cu_{15}$ alloy sample is plotted in Fig.F10b. After the first processing step, nearly constant hardness values are measured across the radii of the disk. The Cu and Fe phases have reached their specific saturation microstructure nearly in the whole sample. Only in the immediate vicinity of the center the applied γ is not sufficient to reach the saturation. However, this part could not be localized by the hardness measurements. The spacing between the two phases in the whole sample is larger than the saturation grain size of the individual phases. Therefore, the hardness is nearly constant. After the second

processing step, a continuous increase of the hardness with increasing radii (i.e. increasing strain) is again observed.

Due to the fast decrease of the lamella spacing of the Fe and Cu phases the size of the grains in Cu and Fe become restricted by the fast decreasing lamella spacing. As a consequence the hardness increases with increasing γ_2 i.e. increasing radius.

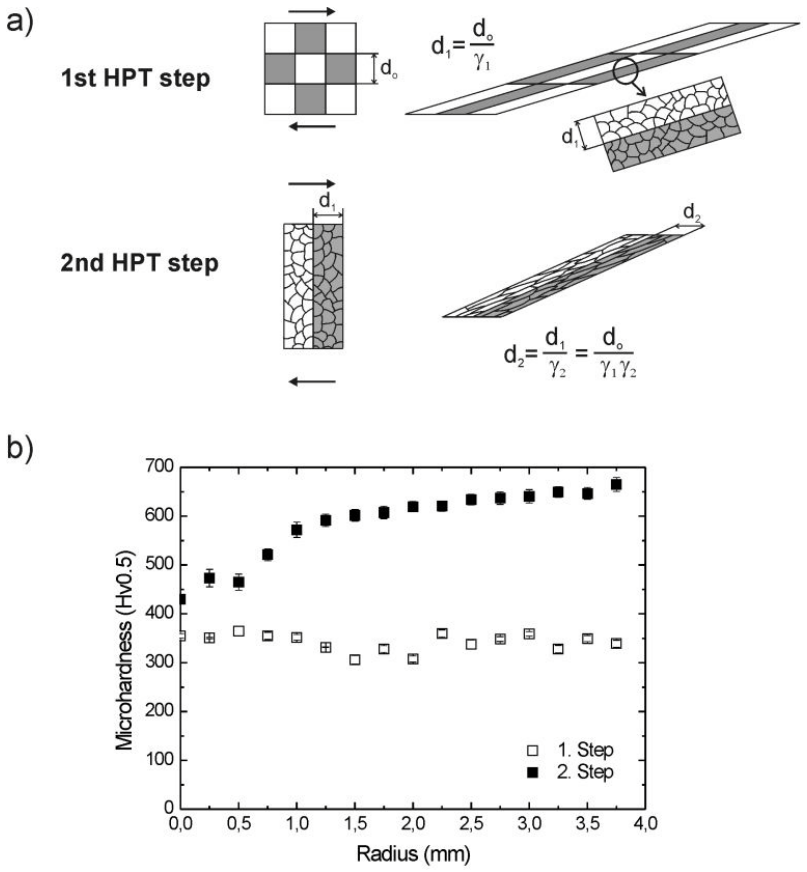

Fig.F10 a) Schematic sketch showing the continuous shearing of the different components of the composite in the first and second deformation step. Between the different deformation steps, a rotation of the sample of 90° is included. b) Microhardness of the $Fe_{85}Cu_{15}$ alloy sample after the first and second processing step. Indents are made across the radii of the sample with a distance of 0.25 mm between the indents.

4.2. The formation of supersaturated solid solutions

From free energy curves calculated by the CALPHAD method [F13], it was shown that for a Fe content x>80, the free energy of the b.c.c. structure is smaller whereas at Fe contents x<40, the f.c.c. structure is more stable. In between, the difference of the free energy between both structures is small and the formation of both phases is favourable. This theoretical result fits quite well with our obtained structures in the FeCu system.

Different mechanisms were proposed in recent years of how the formation of a solid solution in immiscible systems with a positive heat of mixing can be explained during SPD. An explanation was given by Veltl et al. [F27]: the driving force to form solid solutions comes from the energy stored in the

grain boundaries in which a considerable amount of enthalpy can be stored in nanocrystalline metals. Jiang et al. [F13], however, showed that the maximum decrease in grain boundary enthalpy is not sufficiently high as compared to the free energy of mixing to explain the formation of solid solutions in the Fe-Cu system. Another explanation is a diffusion driven process. Raabe et al. [F28], however, suggested that such a process can be excluded due to the lack of thermodynamic forces. The high number of introduced point defects during SPD like the high dislocation density is proposed as another mechanism for the solid solution formation which can be summarized as defect-enhanced diffusion processes [F29-31]. The formation of a high number of non equilibrium vacancies during SPD has been reported by a lot of researchers. Sauvage et al. [F16] reported a very high vacancy production rate of 10^{-5} s^{-1} during HPT which would increase the diffusion coefficient and furthermore enable the mechanical alloying of Fe and Cu. Nevertheless, the strain energy induced by mechanical deformation alone is not sufficient as calculated in [F10]. The defect-enhanced diffusion processes are proposed to be possible in [F28], but the net flux depends on different defect densities and mobilities in the different phases.

Yavari et al. [F14,F32,F33] proposed a different explanation for the occurrence of the formation of solid solution in Fe and Cu for f.c.c solid solutions. The free energy curve of a Fe component can be raised by the interfacial energy term [F14]

$$\Delta G_{\text{int}} = 3\gamma_{FeCu} V_m / r \qquad (3)$$

where V_m is the molar volume and r is the radius of the particle. γ_{FeCu} is the interfacial energy between FeCu interfaces. Therefore, if small Fe particles are formed the free energy curve of Fe is raised to higher values. This is accompanied with a change of the comment tangent with the free energy curve of the Cu phase to higher Fe contents and therefore to an enhancement of supersaturation. If elemental fragments with small tip radii below 2 nm are formed, capillary pressures forces the atoms which are on the tip of the fragments to dissolve. This process continues as long as such small fragments are continuously created. In mechanical alloying, the grains size of initial pure Cu f.c.c. phase is reduced in the beginning to a value of about 20 nm and remains constant at higher milling times. The same happens with the initial pure Fe b.c.c. phase which gets refined until a grain size of 10 nm before it disappears. Even if the overall grain size of the solid solution phase is around 10 nm, it is possible that small fragments below 2 nm are formed again and again if the deformation continues. From the calculated energy stored in the Fe/Cu interface for an elemental size of 1 nm, formation of f.c.c. solid solutions is energetically possible. The same processes might occur during HPT deformation. Sauvage et al. [F16] showed that Fe clusters with a nanometer size are dissolved during HPT. The smaller the size of the Fe clusters the higher the amount of dissolved Fe in Cu. Nonetheless, complete single phase supersaturated solutions were not obtained in this work. The second processing step offers a new possibility to quickly obtain grain size regions were the formation of complete supersaturated solid solutions in the FeCu system are feasible.

Therefore, the enthalpy contribution of the Fe/Cu interfaces can act as driving force for the solid solution formation at least for f.c.c. solid solutions [F14,F32,F33]. It might be also an explanation for the b.c.c. solid solution formation during SPD. Additional enthalpy which comes from the SPD is not included in this calculation. Therefore, the enthalpy contribution from the interface together with a

contribution from the deformation might be large enough to overcome the positive heat of mixing of this alloy in the b.c.c region.
Another explanation is given in [F28]: Dislocation shear driven alloying which includes a dislocation assisted carrier mechanism with multislip shear transfer one more than one slip system across heterophase interfaces is proposed to explain the mechanically induced mixing in normally immiscible systems. This mechanism is also known as dislocation shuffle mechanism [F34].

4.3. The hardness evolution after annealing

Decomposition occurs during annealing above temperatures of 300°C which leads to the formation of a nanocrystalline FeCu composite material with an enhanced hardness and an extraordinary thermal stability. Even at high annealing temperatures, the nanocrystalline structure of the composite is retained and hardness values remains nearly constant. After decomposition separated f.c.c. and b.c.c phases exist in the composite. Due to this structural configuration where grains of the one phase may be isolated from the other phase grain growth through boundary migration is reduced [F35]. Another reason for the observed high thermal stability may be impurities which are introduced in the latter bulk compacts from the as-received powders or from contamination during processing. Such impurities would furthermore retard grain boundary movement. However, due to the relative large initial powder size the content of impurities should be relatively small.
In general, the hardness of the FeCu composites in the as deformed state increases with increasing Fe content after both processing steps. With a simple rule of mixture,

$$H_{composite} = H_{cu} * F_{cu} + H_{Fe} * F_{Fe}, \qquad (4)$$

the upper bound of the hardness of the composite ($H_{composite}$) materials can also be calculated. For H_{cu} and H_{Fe}, which denote the hardness of pure Cu and Fe with a similar grain size (~ 15 nm), values of 153 and 693 HV are used [F36,F37]. F_{Cu} and F_{Fe} is the fraction of Cu and Fe in the composite. The predicted hardness values of the composites calculated with this rule of mixture are lower compared to the experimental ones in the case of the $Fe_{85}Cu_{15}$ and $Fe_{15}Cu_{85}$ samples. Therefore, solid solution hardening seems to take place although it is only reported to occur for Cu(Fe) alloys [F38]. The experimental hardness of the $Fe_{50}Cu_{50}$ fits well to estimated ones but the experimental hardness of the $Fe_{70}Cu_{30}$ sample is too low. After decomposition of the single phase FeCu composite structure ($Fe_{85}Cu_{15}$ and $Fe_{15}Cu_{85}$) and before grain growth during annealing sets in, an enhanced hardness compared to the as deformed material is observed. The same behaviour is observed in supersaturated CuCr composites [F18]. In this case, solid solution softening in the as deformed state was given as an explanation for the enhanced hardness in the annealed state. In our case, no solid solution softening occurred in the as deformed samples. One explanation for the enhanced hardness after annealing in our study might be the additional strengthening from the interphase boundaries between the dissimilar b.c.c. and f.c.c phases as shown in [F39] which are formed right after decomposition. Nevertheless, further investigations regarding the hardness phenomena have to be conducted to explain the details of the observed phenomena in future.

5. Conclusion

Bulk nanostructured FeCu alloys are prepared by a two step HPT deformation process. In all alloys f.c.c and b.c.c solid solutions which are far from equilibrium are formed with this new two step SPD technique similar as after ball milling. After the first processing step, an ultrafine grained two phase composite material is formed. After the second deformation step, nanostructured supersaturated solid solutions were achieved. It was shown that mechanical intermixing of Fe and Cu is possible with SPD. The decomposition of the supersaturated solid solutions upon annealing is used to produce in situ two phase nanocrystalline homogeneous FeCu composites. The FeCu composites after annealing show an enhanced hardness as well as a high thermal stability.
The advantages of the newly developed process are an uncomplicated control of the composition of the alloy, the possible combination of arbitrary material combinations, the easy production process and a high quality final product which is already in bulk form.

Acknowledgments

The financial support by the Austrian Fonds zur Förderung der wissenschaftlichen Forschung (Project number: S10402-N16, S10403, T 512-N20) is gratefully acknowledged.

References for publication F

[F1] Di Maggio R, Ischia G, Rossi F, Molinari A, Bortolotti M. J Mater Sci 2007;42:9284.

[F2] Kakisawa H. Mater Sci Eng A 2003;340:175.

[F3] Ma E. Prog Mater Sci 2005;50:413.

[F4] Johnson WL. Prog Mater Sci 1986;30:81.

[F5] Koch CC. Materials Science and Technology. Weinheim:VCH;1991.

[F6] Oehring MY, Klassen T, Bormann R. Phys status solidi 1992;131:671.

[F7] Holzer JC, Johnson WL, Eckert J, Krill CE. J Appl Phys 1993;73:2794.

[F8] Eckert J, Spooner S, Johnson WL, Ahn CC, Fultz B, Hong LB. Metall Mater Trans A 1996;27:2934.

[F9] Ishihara KN, Uenishi K, Nasu S, Kobayashi KF, Hatano H, Shingu PH. Z Metallkunde 1992;83:132.

[F10] Ma E, Pinkerton FE, Atzmon M. J Appl Phys 1993;74:955.

[F11] Jiang JZ, Gente C, Bormann R, Gonser U. App Phys Lett 1993;63:2768.

[F12] Dong ZF, Wu YK, Huang JY, Ye HQ, Yu YD. J Mater Res 1996;11:2717.

[F13] Jiang JZ, Gente C, Bormann R. Mater Sci Eng A 1998;242:268.

[F14] Yavari AR, Desre PJ, Benameur T. Phys Rev Lett 1992;68:2235.

[F15] Quelennec X, Menand A, Le Breton JM, Pippan R, Sauvage X. Philos Mag 2010;90:1179.

[F16] Sauvage X, Wetscher F, Pareige P. Acta Mater 2005;53:2127.

[F17] Valiev RZ, Islamgaliev RK, Alexandrov IV. Prog Mater Sci 2000;45:103.

[F18] Sauvage X, Jessner P, Vurpillot F, Pippan R. Scr Mater 2008;58:1125.

[F19] Barquín LF, Gorria P, Smith RI, Blanco JA, Pérez MJ, Martínez-Blanco D. Phy Rev B 2005:72.

[F20] Martínez-Blanco D, González MA, Gorria P, Iglesias R, Palacios SL, Hernando A, Blanco JA, Pérez MJ, Fernández Barquín L. J Magn Magn Mater 2005;300:229.

[F21] Campo J, Martínez-Blanco D, González MA, Gorria P, Pérez MJ, Blanco JA. Physica B 2006;384:336.

[F22] Pippan R, Bachmaier A, Gludovatz B, Scheriau S, Hohenwarter A. Int J Mater Res 2009;100:1653.

[F23] Pippan R, Sabirov I, Wetscher F, Vorhauer A, Hafok M. Adv Eng Mater 2006;8:1046.

[F24] Pippan R, Scheriau S, Taylor A, Hafok M, Hohenwarter A, Bachmaier A. Annu Rev Mater Res 2010;40:319.

[F25] Park K-T, Shin DH. Mater Sci Eng A 2002;334:79.

[F26] Islamgaliev RK, Buchgraber W, Kolobov YR, Amirkhanov NM, Sergueeva AV, Ivanov KV, Grabovetskaya GP. Mater Sci Eng A 2001;319-321:872.

[F27] Veltl G, Scholz B, Kunze HD. Mater Sci Eng A 1991;134:1410.

[F28] Raabe D, Choi PP, Li YJ, Kostka A, Sauvage X, Lecoturier F, Hono K, Kircheim R, Pippan R, Empury O. MRS Bull 2010;35:982.

[F29] Mazzone G, Antisari MV. Phys Rev B 1996;54:441.

[F30] Mazzone G, Montone A, VittoriAntisari M, Angiolini M. Mater Sci Forum 1997;235:175.

[F31] Mazzone G, VittoriAntisari M, Montone A, Cardellini F, Krasnowski M, Angiolini M. Microsc Microcanal 1995;6:601.

[F32] Yavari AR. Mater Trans 1995;36:228.

[F33] Yavari AR. Mater Sci Eng A 1994;179-180:20.

[F34] Ohsaki S, Raabe D, Hono K. Acta Mater 2009;57:5254.

[F35] Schaffer G. Scripta Metall Mater 1992;27:1.

[F36] Nieman GW, Weertman JR, Siegel RW. J Mater Res 1991;6:1012.

[F37] Jang JSC, Koch CC. Scripta Metall Mater 1990;24:1599.

[F38] Shen TD, Koch CC. Acta Mater 1996;44:753.

[F39] He L, Ma E. Nanostruct Mater 1996;7:327.